J. Reiser et al.

Ductilisation of tungsten (W): Tungsten laminated composites

Ductilisation of tungsten (W): Tungsten laminated composites

Jens Reiser[a,*], Lauren Garrison[b], Henri Greuner[c], Jan Hoffmann[a], Tobias Weingärtner[a], Ute Jäntsch[a], Michael Klimenkov[a], Peter Franke[a], Simon Bonk[a], Carsten Bonnekoh[a], Sven Sickinger[a], Siegfried Baumgärtner[a], Daniel Bolich[a], Mirjam Hoffmann[a], Rainer Ziegler[a], Joachim Konrad[a], Jörg Hohe[d], Andreas Hoffmann[e], Tobias Mrotzek[e], Martin Seiss[e], Michael Rieth[a], Anton Möslang[a]

a: Karlsruhe Institute of Technology, Institute for Applied Materials, 76344 Eggenstein-Leopoldshafen, Germany
b: Oak Ridge National Laboratory, Oak Ridge, TN 37831, USA
c: Max Planck Institute for Plasma Physics, Department of Plasma Edge and Wall, 85748 Garching, Germany
d: Fraunhofer Institute for Mechanics of Materials, 79108 Freiburg, Germany
e: PLANSEE SE, 6600 Reutte, Austria

Corresponding author:
*:   Dr. Jens Reiser, Karlsruhe Institute of Technology (KIT), Institute for Applied Materials (IAM-AWP), Hermann-von-Helmholtz-Platz 1, 76344 Eggenstein-Leopoldshafen, Germany, Phone: +49 721 608 23894, e-mail: jens.reiser@kit.edu

Highlights:
- Mechanisms of plastic deformation and fracture of W laminates have been elucidated
- Diffusion mechanisms in W-Cu, W-V, and W-Pd laminated composites have been identified
- Properties after annealing for 10, 100 and 1000 h at 1000°C (1273 K) have been determined
- Three-point bending, Charpy impact, and tensile tests have been performed
- Divertor components made of W laminates have been built and HHF tested in GLADIS

Keywords:

- Multilayer material
- Ductility
- Brittle-to-ductile transition
- Nuclear fusion
- Divertor
- Diffusion in tungsten

Abstract

Here we elucidate the mechanisms of plastic deformation and fracture of tungsten laminated composites. Our results suggest that the mechanical response of the laminates is governed

by the plastic deformation of the tungsten plies. In most cases, the impact of the interlayer is of secondary importance.

Severely cold-rolled ultrafine-grained tungsten foils possess exceptional properties in terms of brittle-to-ductile transition (BDT), toughness, and tensile ductility. The motivation for investigating laminated composites is to determine whether a bulk material can be made that retains the ductility of the thin tungsten foils.

In this paper we analyse W-AgCu, W-Cu, W-V, and W-Pd laminates in their as-produced and annealed conditions (e.g. 10, 100 and 1000 h at 1000°C (1273 K) in vacuum). The analyses comprise (i) the mechanical characterisation by means of three-point bending (damage tolerance), Charpy impact (BDT), and tensile tests (total elongation to fracture) as well as (ii) the in-depth analyses of the microstructure by means of scanning electron microscopy (SEM), transmission electron microscopy (TEM), and Auger electron spectroscopy (AES).

W-Cu laminates (60 vol % W) show 15.5 % total elongation to fracture in a tensile test at room temperature. Furthermore, the BDT of tungsten laminated composites occurs at a temperature that is several hundreds of Kelvin lower than the BDT temperature of the pure tungsten bulk counterparts.

Finally, we present the successful fabrication of a 1000 mm long W-Cu laminated pipe and show its high heat flux performance. Fabrication studies of high heat flux components made of tungsten laminates, in which the laminates are used either as heat spreaders or structural pipes, are presented.

1. Introduction

Nuclear fusion is an ideal sustainable energy source. A major hurdle to its commercial development is the availability of sufficiently resilient materials [1, 2]. Tungsten and tungsten-based materials are candidates for plasma-facing components. For these components, there is a need for both armour tungsten (which shields the underneath structural material from the high heat flux and particle flux from the plasma), as well as structural tungsten (performing the function such as a pipe for a cooling medium) [3]. For tungsten, its tendency to fail at low temperatures by brittle fracture is a major disadvantage [4]. Therefore, the main challenge that needs to be overcome to make a successful plasma-facing component is to make tungsten ductile, which means achieving improvement of

- the tensile ductility (e.g. the total elongation to fracture, A_t),
- the toughness, K_{IC}, or the crack growth resistance, and
- the brittle-to-ductile transition temperature (BDTT).

A method to improve these properties is the modification of the microstructure through cold-rolling. Wei and Kecskes assessed the effect of low-temperature rolling (rolling at 800°C (1073 K), 600°C (873 K), and 400°C (673 K)) on the room-temperature tensile behaviour of pure tungsten. Their results show that the ductility (i.e. total elongation to fracture) increases with decreasing rolling temperature [5]. The impact of cold-rolling on the toughness and the crack growth resistance has been investigated by Reiser et al. [6]. Their results show that severely cold-rolled tungsten plates have a much lower stable crack growth onset temperature compared to their cold-rolled counterparts. Furthermore, Reiser et al. showed that a cold-rolled tungsten plate possesses a lower brittle-to-ductile-transition temperature compared to its hot-rolled or recrystallised counterparts [7]. Finally Németh et al. elucidated the nature of the brittle-to-ductile transition of severely cold-rolled and recrystallised tungsten foils [8]. Their results obtained from the severely cold-rolled foils indicate a brittle-to-ductile transition at -196°C (77 K).

Severely cold-rolled tungsten plates exhibit extraordinary mechanical properties and will be used for the synthesis of the laminated composites within this study.

A tungsten sheet that experienced a high degree of cold-rolling is in most cases rolled down to a thin foil with a thickness of e.g. 100 μm (Fig. 1A). The motivation for investigating laminated composites is to determine whether a bulk material can be made that retains the ductility of the thin severely cold-rolled ultrafine-grained tungsten foils. Therefore, tungsten laminates were produced that consist of repeated layers of tungsten and an interlayer, joined together into a multilayer material (Fig. 1B).

The tungsten foil laminates allow the assembling and production of three-dimensional geometries and components such as deep-drawn caps (Fig. 1C) or pipes (Fig. 1D, E), which are used as structural tungsten in high heat flux test components (Fig. 1F).

The following sections will provide answers to the following questions:

- What are the main energy dissipation mechanisms in tungsten laminated composites (plastic deformation of the tungsten foils, plastic deformation of the interlayer sheets, creation of new surfaces)?
- What is the role of the copper (Cu) interlayer on the improved mechanical and thermo-physical properties (residual stresses, crack arresting and deflection)?
- How do the Charpy impact properties of W-Cu, W-V, and W-Pd laminates change through annealing (10, 100 and 1000 h at 1000°C (1273 K))?
- What is the performance of W-Cu laminated pipes in a high heat flux test?

Fig. 1. Overview of the material system "tungsten laminated composites". The starting point is severely cold-rolled tungsten foils (A) that are joined together into a multilayer material (B, Charpy impact test sample, 3 mm x 4 mm x 27 mm, 1 mm notch, KLST type). Three-dimensional shapes such as a cap (C) or a pipe (D, E) can be produced. The pipes are used as structural tungsten in high heat flux test components (F).

This paper is organised as follows: previous studies on laminated composites based on refractory metals are presented in the following section. Afterwards, the materials and methods are briefly described. This is followed by a results and discussion section, which is divided into four parts: first, we present the proof of principle using W-AgCu laminates. In the second part, the potential of W-Cu laminates is discussed. Third, the properties of W-V and W-Pd laminates are analysed, and finally, the potential of W-W laminated composites are displayed. The paper is finalised with a brief conclusion and outlook.

2. Background: Laminated composites based on refractory metals

In this section, we present selected studies on laminated composites based on refractory metals (Table 1). The results obtained and the mechanisms identified by these studies are useful in developing successful plasma-facing components and give an impression on the complexity of this type of materials.

Laminated composites or multilayer composites, as they are also called, are widespread in material science and technology. The idea is to tailor properties such as (i) thermal conductivity, (ii) thermal expansion, (iii) strength, or (iv) tensile ductility, toughness and brittle-to-ductile transition, by an appropriate adjustment of a layered structure.

2.1. Thermal conductivity and the coefficient of thermal expansion

Laminated composites made of repeated layers of molybdenum (Mo) and copper (Cu) have become increasingly important in the field of thermal management. The development of power electronics, light emitting diodes and radio-frequency devices demands innovative heat sink and heat spreader materials. In particular, the thermal management of gallium nitride (GaN) chips demand heat spreader materials with a high thermal conductivity (> 300 W/(m*K)), combined with an adjusted coefficient of thermal expansion (6–12 ppm/K) [9]. These requirements can be tailored by molybdenum copper multilayer composites, as these composites combine the high thermal conductivity of copper (397 W/(m*K) at room temperature) with the low coefficient of thermal expansion of molybdenum (4.8 ppm/K, 20–100°C (293–373 K)) [9, 10]. In particular the thermal conductivity of a multilayer material can easily be estimated by using the rules of mixture (ROM).

The linear and reciprocal rules of mixture provide simple analytical formulae to estimate the homogenised material properties. The linear rule of mixture is given by

$$p^{lin} = V_1 * p_1 + V_2 * p_2 \qquad (1)$$

and the reciprocal rule can be written as

$$\frac{1}{p^{rec}} = \frac{V_1}{p_1} + \frac{V_2}{p_2} \qquad (2)$$

where p_1 and p_2 are the material properties of layers 1 and 2, and V_1 and V_2 are the corresponding volume fractions.

It has been shown by Hill [11] that for entirely linear homogenisation problems, the rules of mixture provide rigorous mathematical bounds. This is why the rules of mixture have proven useful to estimate the homogenised thermal conductivity in the in plane (linear rule of mixture, Eq. (1)) and in the through plane (reciprocal rule of mixture, Eq. (2)) directions (in Eq. (1) and (2) the thermal interface resistance due to electron scattering is not considered). However the rules of mixture can fail to estimate the coefficients of thermal expansion. Seiss et al. reported the peculiar behaviour of the coefficient of thermal expansion in Mo-Cu multilayer composites, which can be summarised as follows: (i) the homogenised coefficients of thermal expansion are found outside the region bounded by the rules of mixture, (ii) with increasing temperature, the coefficient of thermal expansion first decreases then gently increases, and (iii) the coefficient of thermal expansion changes during thermal cyclic loading [9, 12]. The reason for these effects is not yet understood, and is the topic of current studies. However it is likely that the plastic deformation of the Cu-phase plays an important role.

4

In this paper, we will report high heat flux tests of components made of heat spreader materials.

2.2. Strength

Multilayer composites exhibit significant increases in strength as the layer thickness is decreased from the micrometre scale to the nanometre scale. Furthermore, multilayer materials are well suited for fundamental studies on the effect of length scale on the strengthening mechanisms. A study on the length-scale-dependent deformation mechanisms in niobium copper (Nb-Cu) multilayer composites has been performed by Misa et al. [13].

In the sub-microns length scale, the Hall-Petch model is found applicable. According to this model, the yield strength, σ_{ys}, scales with the inverse square root of the relevant microstructural length scale (grain size or layer thickness, h)

$$\sigma_{ys} \sim h^{-1/2}. \tag{3}$$

A breakdown of the Hall-Petch model is observed in metallic multilayers when the layer thickness is in the order of a few tens of nanometres. In that case, plastic flow is confined to one layer and occurs by the motion of single dislocation loops. Therefore, confined layer slip of a single dislocation is treated as the operative mechanism.
In detail, dislocations that are nucleated at the interface are pinned on the opposite interface and spread as Orowan loops. It is this Orowan bowing motion of the glide dislocation that leads to hardening with decreasing layer thickness.
For further details on the strengthening mechanisms of multilayer materials such as the lattice parameter mismatch and dislocation-interface interaction (i.e. blocking, absorbing, transmission) the reader is referred to Refs. [13-15].

The mechanical and thermo-physical properties of W-Cu laminates may be significantly affected by the plastic deformation of the Cu-phase. By reducing the layer thickness, the yield stress in the Cu-phase increases according to the models presented above. This offers the possibility of designing multilayer materials that operate solely in the elastic regime.

Strength has been the main thrust for multilayer investigations. Tensile ductility, toughness, and brittle-to-ductile transition have been given less attention.

2.3. Tensile ductility, toughness, and brittle-to-ductile transition

Vill et al. [16] studied tungsten molybdenum microlaminates. Molybdenum layers were attached in between thin tungsten layers in order to provide an enhanced toughness of the material. In a recent publication, we demonstrated that the brittle-to-ductile transition temperature can be decreased by several 100s K by the synthesis of a tungsten laminated composite (W-AgCu) [17]. Our results were confirmed by Basuki et al. [18], who reported the potential of tungsten vanadium (V) multilayer materials. Furthermore, the damage tolerance of a layered microstructure, demonstrated by means of three-point bending tests, has been reported by Shao et al. (W-TiNiNb) [19] and Zhang et al. (W-Ta) [20].

The tensile behaviour of refractory metal based laminated composites has been assessed by Beals and Nardone (Nb-Al$_2$O$_3$) [21] and Hoffmann and Weeton [22]. The latter reported a study of laminar composites composed of mutually insoluble sheets of tungsten and copper. By selecting this model system, the reactivity between tungsten and copper has been eliminated as a variable.

Hoffmann and Weeton anticipated several high-temperature uses for the laminated material: e.g, turbine blades, chambers for advanced rocket engines, or thrust reverses. The tensile behaviour of the W-Cu laminates was discussed against the results from tungsten fibre / copper matrix model system composites [23].

Hoffmann and Weeton gave consideration to the laminate failure modes and the experimentally determined stress-strain relations to obtain an indication of the deformation behaviour during tensile testing. Four stages of deformation were observed:

- Stage 1: Elastic deformation of W, elastic deformation of Cu
- Stage 2: Elastic deformation of W, plastic deformation of Cu
- Stage 3: Plastic deformation of W, plastic deformation of Cu
- Stage 4: Fracturing of W and Cu

In particular, fracturing of the tungsten sheets was indicated by a serrated load-strain curve.

With regard to the tensile behaviour of W-Cu composites that we will report within this paper, the investigation of Hoffmann and Weeton yielded the following major result: For W-Cu laminates with more than 20 vol % W, and tested at room temperature, no elongation was measurable for the fractured specimens. In contrast, we will present and discuss a W-Cu laminate with 60 vol % W that shows 15.5 % total elongation to fracture at room temperature.

Table 1
Selected laminated composites based on refractory metals.

Properties of interest (technical application)	Components	Referred to as	Fabrication route	Methods	Reference
Thermal conductivity, coefficient of thermal expansion (thermal management)	Mo-Cu	Multilayer composite	-	Transient flash, dilatometer	[9]
	W-CuCrZr	Laminates		Numerical homogenisation analysis, representative volume elements (RVE)	[24]
Strength	Nb-Cu	Multilayer composite	Magneton sputtering	Nano-indentation hardness	[13]
	Nb-Cu	Multilayer	Accumulative roll bonding		[25]
	Nb-Cu	Multilayer composite	Physical vapour deposition		[26]
Ductility, toughness, brittle-to-ductile transition	W-Mo	Microlaminates	Sputtering		[16]
	W-AgCu	Laminates	Brazing (800°C (1073 K), 1 min.)	Charpy impact tests	[17]
	W-Ti	Laminates	Diffusion bonding (900°C (1173 K), 35 MPa, 1 h)	Charpy impact tests	[27]
	W-V	Hybrid material	Diffusion bonding	Charpy impact tests	[18]

		(700°C (973 K), 97 MPa, 4 h)		
W-TiNiNb	Laminated composite	Vacuum hot pressing (1220°C (1493 K), 20 MPa, 0.5 h)	Three-point bending tests	[19]
W-TiNi	Micro-laminated composite	Vacuum hot pressing (1300°C (1573 K), 20 MPa, 0.5 h), forging at 880°C (1153 K)	Three-point bending tests, compression tests	[28]
W-Ta	Multilayers	Spark plasma sintering (1700°C (1973 K), 95 MPa, 5 min.)	Three-point bending tests	[20]
Nb-Al$_2$O$_3$	Composite laminate	Vacuum hot pressing (1500°C (1773 K), 104 MPa, 1 h)	Tensile tests	[21]
W-Cu	Laminar composites	Vacuum hot pressing (982°C (1255 K), 14 MPa, 4 h)	Tensile tests	[22]
W-CuCrZr	Laminates		Tensile properties obtained by a numerical homogenisation analysis, RVE	[24]

Detailed information on the synthesis of the laminates as well as an overview of the materials and methods used in our investigations will be given in the next section.

3. Materials and methods

This section is divided into three parts. In the first part we provide details on the synthesis of the tungsten foil laminates. This includes a description of the microstructure and the chemical composition of the tungsten foils and the interlayer sheets. Furthermore, details of the thermal ageing conditions of the tungsten foil laminates are given. The first part closes with a description of the processing history and microstructure of the tungsten plate materials used for benchmark experiments. In the second part, details of the mechanical tests such as the three-point bending, tensile, and Charpy impact tests are presented. Finally, in the third part,

we provide detailed information about the election microscopy analyses performed within this paper.

In this paper, the notation for the reference directions and the notation for the crack systems are according to ASTM E399 [29]. There, "L" is the direction of principal deformation (i.e. length, longitudinal, rolling direction, 0°), "T" is the direction of least deformation (i.e. width, long transverse, 90°) and "S" is the third orthogonal direction (i.e. thickness, short transverse). The notation of the crack system uses the two-letter code. The first letter designates the direction normal to the crack plane, and the second letter the expected direction of crack propagation. For example, the L-S specimen fracture plane normal is in the longitudinal direction of the laminate/plate and the expected direction of crack propagation is coincident with the third orthogonal direction (or short transverse) of the laminate/plate. Fig. 2 visualises the description of the notation for the crack systems.

For specimens tilted with respect to two of the reference axes, the crack plane orientation is identified by a three-letter code. The designation LT-S, for example, indicates a crack plane normal to be intermediate between the L (0°) and T (90°) (thus at an angle of 45°), and the expected fracture direction to be in the S-direction.
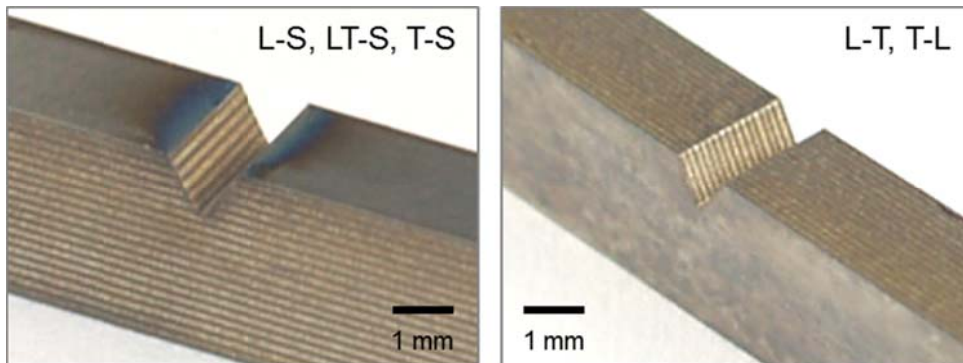

Fig. 2. We use the notation for the crack systems according to ASTM E399 [29]. An example for a laminate with an L-S, LT-S or T-S orientation is shown in the left-hand image; a laminate representing an L-T or T-L crack system is shown in the right-hand image.

3.1. Materials: tungsten foil laminates and tungsten plate material

Tungsten laminates consist of repeated layers of tungsten and interlayer, joined together into a multilayer material. In this section we will (i) give details of the tungsten foils and interlayer sheets, (ii) present the synthesis of the laminate materials, (iii) describe the thermal ageing conditions, and finally (iv) give comments on the fabrication history and microstructure of tungsten plate materials that have been used for benchmark experiments.

3.1.1. Tungsten foil

The tungsten materials used for the synthesis of the laminates are technically pure tungsten foils (> 99.97 wt % W) manufactured by PLANSEE SE in a powder metallurgical route consisting of sintering and rolling. The impurity concentrations, which PLANSEE SE guarantees not to exceed, as well as the typical impurity concentrations, are shown in Table 2 [30].

Table 2
Impurity concentration of the tungsten foils. The first row shows the maximum concentration of selected elements, which PLANSEE SE guarantees not to exceed, while the second row gives the typical impurity concentrations.

Element	Al	Cr	Cu	Fe	K	Mo	Ni	Si	C	H	N	O

Guaranteed analyses (max.), $\mu g/g$	15	20	10	30	10	100	20	20	30	5	5	20
Typical analyses (max.), $\mu g/g$	1	3	1	8	1	12	2	1	6	0	1	2

The tungsten foils had a thickness of 100 μm and are considered as severely cold-rolled, ultrafine-grained. The foils were used in their as-received condition. This means that the foils experience a stress-relieving heat treatment after rolling. The grain size of the foils in the S-direction is about 0.5 μm, and the grain shape can be described best as pancake-like. The hardness measurements with indentation in the T-direction gave a value of approximately 600 HV0.1. The severely cold-rolled tungsten foils show a characteristic crystallographic texture, as the α-fibre (<110> || RD) and the γ-fibre (<111> || ND) orientations are well pronounced with maximum intensities for the rotated cube component, {100}<011>. For further details on the microstructure of the foils, the reader is referred to Refs. [31, 32].

To help clarify the discussion of the microstructural origin of the Charpy impact properties of the tungsten foil laminates, selected microstructural features of the tungsten foils are visualised and plotted next to Charpy impact test samples and their crack system in Fig. 3. Fig. 3 also displays the well-known fact that tungsten, like other body-centred cubic metals, primarily cleaves on the {100} cleavage plane. The second cleavage plane for tungsten is the {110} plane. Furthermore, Fig. 3 shows the <111> slip direction of body-centred cubic metals.
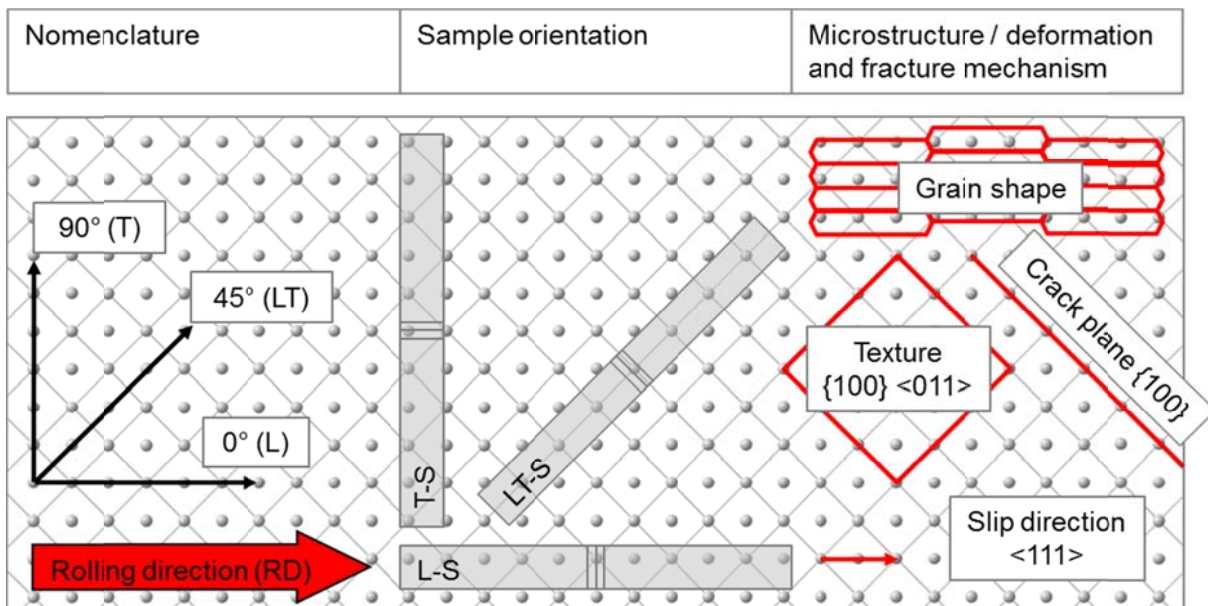

Fig. 3. The anisotropy of the Charpy impact properties revealed from samples representing the L-S, T-S and LT-S crack systems will be discussed against microstructural features of the severely cold-rolled, 100 μm-thick tungsten foils. These features are the grain shape, the crystallographic texture, the primary cleavage plane, and the slip direction. This figure provides a representation on the top surface on the tungsten foil.

In the majority of cases, the laminates were made of tungsten foils in their as-received condition. In only one particular case, the tungsten laminate was made of recrystallised tungsten foils. The foils were annealed for 1 h at 1800°C (2073 K) in vacuum. The median grain size of the recrystallised foils is approximately 20 μm x 20 μm x 20 μm. The hardness measurements with indentation in the T-direction gave a value of about 400 HV0.1. After annealing, the crystallographic texture is even more pronounced with maximum intensities of

the rotated cube component, {100}<011>. For further details of the microstructure of the recrystallised foils, the reader is referred to Ref. [31].

The tungsten foil laminates were tested both in the as-produced and in the conditions after thermal ageing, so the recovery and recrystallisation behaviour of tungsten foils is of importance. Bonnekoh et al. describe the recrystallisation behaviour of ultrafine-grained tungsten foils as follows. The grains do not produce recrystallization nuclei, so primary recrystallisation is suppressed and the deformation texture is inherited. Such a situation can be referred to as "recrystallisation in situ" [33].

Studies of the tensile behaviour of the tungsten foils in the as-received and recrystallised condition (1 h / 2000°C (2273 K) and 1 h / 2700°C (3073 K) in hydrogen) can be found in Ref. [34]. The most important results can be summarised as follows:

- As-received condition (ultrafine-grained): at a test temperature of 600°C (837 K) the engineering stress-strain curves of foils tested in the rolling direction (0°) and perpendicular to the rolling direction (90°) are congruent. This result can easily be understood by considering the 90° rotation symmetry of the {100}<011> rotated cube component. When the foils are tested at room temperature the situation appears rather different. Now the samples tested in the rolling direction (0°) show plastic deformation, whereas the samples tested perpendicular to the rolling direction (90°) are brittle. This material response is attributed to the anisotropic grain shape of the foils and the change of the dislocation-grain-boundary interaction.
- Recrystallised condition (coarse-grained): at a test temperature of 600°C (837 K) the engineering stress-strain curves of the foils show up to 40 % plastic strain. The plastic deformation is accompanied by serrated flow. The microstructural origin of the serrated flow is associated with strain localisation and propagation (strain bursts) followed up by dislocation-surface-interactions (dislocation annihilation). At a test temperature of 20°C (293 K) the foils behave brittle.

In the next section, details of the interlayer sheets will be provided.

3.1.2. Interlayer

The interlayer materials used for the synthesis of the laminated composites are (i) an eutectic silver (Ag) copper (Cu) alloy (according to DIN EN 1044, AG 401, and ISO 3677, B-Ag72Cu-780, 72 wt % Ag, 28 wt % Cu, melting temperature, T_m = 780°C (1053 K)), (ii) pure copper (> 99.99 wt % Cu, T_m = 1084°C (1357 K)), (iii) vanadium (V) (> 99.8 wt % V, T_m = 1910°C (2183 K)), and (iv) palladium (Pd) (> 99.9 wt % Pd, T_m = 1555°C (1828 K)).

3.1.3. Laminate synthesis

In Section 4.1. "W-AgCu laminates", three-point bending tests were performed on W-AgCu laminates. The material consisted of eight layers of tungsten foil (100 μm, as-received condition) brazed together to a laminate using seven layers of AgCu foil (100 μm). The laminate had a total thickness of 1.5 mm. From this laminate, specimens with dimensions of 1.5 mm x 10 mm x 20 mm were cut by spark erosion. The specimens represent the L-S crack system, without notch.

Section 4.1. "W-AgCu laminates", also describes Charpy impact properties. The material used for these tests consisted of repeated layers of 100 μm tungsten (20 sheets, as-received condition) and 100 μm AgCu (19 sheets) brazed together into a laminate with a total thickness of 3.9 mm. From this laminate, specimens with dimensions of 3 mm x 3.9 mm x 27

mm, 1 mm notch (approx. KLST-type) were cut by spark erosion. The specimens represent the L-S, T-S and LT-S crack systems.

Furthermore, in Section 4.1. "W-AgCu laminates", the results of laminates made from recrystallised tungsten foils (annealed for 1 h at 1800°C (2073 K) in vacuum) are presented. The laminate consisted of 20 layers of tungsten foil (100 μm, in the recrystallised condition) brazed together using 19 layers of AgCu foil (100 μm). The laminate had a total thickness of 3.9 mm. From this laminate, specimens with dimensions of 3 mm x 3.9 mm x 27 mm, 1 mm notch (approx. KLST-type) were cut by spark erosion. The specimens represent the L-S crack system.

Finally, in Section 4.1. "W-AgCu laminates", tensile properties are displayed. The material tested consisted of three layers of 100 μm tungsten (as-received condition) and two layers of 100 μm AgCu, brazed together into a laminate with a total thickness of 0.5 mm. From these laminates, tensile test specimens were cut by spark erosion. The samples had a width of 2 mm and a gauge length of 13 mm. The samples were aligned in such a way that the tensile loading direction was congruent with the rolling direction of the tungsten foils (0°).

Further tensile properties are described in Section 4.2. "W-Cu laminates". Again, the material tested consisted of three layers of 100 μm tungsten (as-received condition) and two layers of 100 μm copper, brazed together into a laminate with a total thickness of 0.5 mm. From this laminate, tensile test specimens were cut by spark erosion. The samples had a width of 2 mm and a gauge length of 13 mm. The samples were aligned in such a way that the tensile loading direction was congruent with the rolling direction of the tungsten foils (0°).

In Sections 4.2. "W-Cu laminates" and 4.3. "W-V and W-Pd laminates", the Charpy impact properties of different kinds of tungsten laminates are displayed. The laminates were produced as follows: n layers of tungsten foil (100 μm, as-received condition) and $n-1$ sheets of an interlayer were placed on each other alternately. This stack of $2*n-1$ foils was then placed in an electro-mechanical universal test device (ZWICK 100). This test device was modified and combined with a vacuum chamber and a furnace (MAYTEC). The stack of foils was heated up to 900°C in a high vacuum (1 x 10^{-5} – 5 x 10^{-5} mbar) and was diffusion bonded for 1 h at 35 MPa. The furnace cooled down to room temperature at a cooling rate of 450 K / h. The material condition directly after cooling is referred to as "as-produced" in this paper. From these laminates, specimens with dimensions of 3 mm x 3.9 mm x 27 mm, 1 mm notch (approx. KLST-type) were cut by spark erosion. The specimens represent the L-S crack system.

The potential of tungsten laminates without interlayers is investigated in Section 4.4. "W-W laminates". Charpy impact test samples with dimensions of 1 mm x 3 mm x 27 mm, without notch, were produced by diffusion bonding of 10 layers of 100 μm-thick tungsten foil. The surfaces of the foils were activated by depositing a thin layer of tungsten by physical vapour deposition before bonding. The diffusion bonding was realised in the electro-mechanical universal test device, as described above. The process parameters were 1 h, 35 MPa, and vacuum. The bonding temperatures were 900°C (1173 K), 1000°C (1273 K), 1100°C (1373 K) and 1200°C (1473 K). The specimens represent the L-S crack system.

During brazing or diffusion bonding the top layers of the stacks of foils were in contact with alumina. We strongly recommend to prevent the top layers to get in contact with graphite, as there is the severe risk of contaminate tungsten with carbon, which leads to the formation of brittle tungsten carbides.

A summary of the aforementioned laminates can be found in Table 3.

Table 3
Overview of the produced tungsten laminates. After layer bonding, the laminates are referred to as "as-produced" in this paper.

Section	Test method	Tungsten foil: thickness / number of sheets	Interlayer: element / thickness / number of sheets	Joining technology	Dimension, orientation
4.1. "W-AgCu laminates"	Three-point bending tests	100 μm / 8	AgCu, 100 μm, 7	Brazing	1.5 mm x 10 mm x 20 mm, L-S, without notch
	Charpy impact tests	100 μm / 20	AgCu, 100 μm, 19		KLST, L-S
					KLST, T-S
					KLST, LT-S
		100 μm / 20 (foils annealed for 1 h / 1800°C (2073 K) in vacuum)	AgCu, 100 μm, 19		KLST, L-S
	Tensile tests	100 μm / 3	AgCu, 100 μm, 2	Brazing	0.5 mm x 2 mm x 13 mm (gauge length), 0°, tensile direction = rolling direction
4.2. "W-Cu laminates"	Tensile tests	100 μm / 3	Cu, 100 μm, 2	Brazing	0.5 mm x 2 mm x 13 mm (gauge length), 0°, tensile direction = rolling direction
	Charpy impact tests	100 μm / 20	Cu, 100 μm, 19	Diffusion bonding	KLST, L-S
4.3. "W-V and W-Pd laminates"	Charpy impact tests	100 μm / 20	V, 100 μm, 19	Diffusion bonding	KLST, L-S
		100 μm / 27	Pd, 50 μm, 26		
4.4. "W-W laminates"	Charpy impact tests	100 μm / 10	-	Diffusion bonding	1 mm x 3 mm x 27 mm, L-S, without notch

3.1.4. Thermal ageing conditions

In Sections 4.2. "W-Cu laminates" and 4.3. "W-V and W-Pd laminates", the evolution of the Charpy impact properties after thermal ageing are displayed. The thermal ageing conditions were as follows: laminates in their as-produced condition were encapsulated in glass ampoules. The procedure consisted of flushing the ampoules with argon, creating vacuum conditions inside the ampoules ($1 \times 10^{-5} – 5 \times 10^{-5}$ mbar), and finally sealing the ampoules with a blowtorch. The laminates were annealed for 10, 100 and 1000 h at 1000°C (1273 K), and cooled to room temperature at a cooling rate of 100 K / h. From these plates, specimens with dimensions of 3 mm x 3.9 mm x 27 mm, 1 mm notch (approx. KLST-type) were cut by spark erosion. The specimens represent the L-S crack system (Table 4).

Table 4
Details of the thermal ageing conditions of the tungsten foil laminates.

Section	Time / temperature	Atmosphere	Cooling rate	Dimension, orientation
4.2. "W-Cu laminates"	10 h / 1000°C (1273 K)	Vacuum, $1 \times 10^{-5} – 5 \times 10^{-5}$ mbar	100 K / h	KLST, L-S
	100 h / 1000°C (1273 K)			
	1000 h / 1000°C (1273 K)			
4.3. "W-V and W-Pd laminates"	10 h / 1000°C (1273 K)	Vacuum, $1 \times 10^{-5} – 5 \times 10^{-5}$ mbar	100 K / h	KLST, L-S
	100 h / 1000°C (1273 K)			
	1000 h / 1000°C (1273 K)			

3.1.5. Tungsten plates for benchmark experiments

The tungsten materials used for benchmark experiments are technically pure tungsten plates (> 99.97 wt % W) manufactured by PLANSEE SE in a powder metallurgical route consisting of sintering and rolling. The impurity concentrations, which PLANSEE SE guarantees not to exceed, as well as the typical impurity concentrations, are shown in Table 2 [30].

In Section 4.1. "W-AgCu laminates", the results of a comparison of the three-point bending behaviour of W-AgCu laminates and pure tungsten plate materials are discussed. The material used for the benchmark experiment was a hot- and cold-rolled tungsten plate. The plate was in its stress-relieved condition. The microstructure reveals a median grain size of 1 μm x 1 μm x 3 μm (S- x T- x L-directions). From this plate, specimens with dimensions of 1 mm x 10 mm x 20 mm were cut by spark erosion. The specimens represent the L-S crack system, without notch.

In Sections 4.1. "W-AgCu laminates", and 4.2. "W-Cu laminates", the tensile properties of tungsten laminated composites are compared with the tensile behaviour of pure tungsten foils. The material used for the benchmark experiments was a severely cold-rolled tungsten foil. The foil was in its as-received condition and possesses a median grain size in the S-direction of 0.5 μm. The foil is the exact same type of foil that makes up the tungsten layers in the laminates. From this foil, specimens were cut by spark erosion. The samples were aligned in such a way that the tensile loading direction was congruent with the rolling direction of the tungsten foils (0°).

In Sections 4.1. "W-AgCu laminates", 4.2. "W-Cu laminates", and 4.3. "W-V and W-Pd laminates", the Charpy impact properties of tungsten foil laminates are discussed against the background of the Charpy impact results of pure tungsten plate material.
The material used for the benchmark experiments was a hot-rolled tungsten plate. The plate was in its stress-relieved, as-received condition with a median grain size of 4 μm x 6 μm x 9 μm, and in its recrystallised condition (annealed for 1 h at 2000°C (2273 K) in hydrogen) with a median grain size of 12 μm x 18 μm x 22 μm. In addition, the plate was in four different conditions of annealing: 10, 100 and 1000 h at 1000°C (1273 K). From these plates, specimens with dimensions of 3 mm x 4 mm x 27 mm, 1 mm notch (KLST) were cut by spark erosion. The specimens represent the L-S crack system.

Finally, in Section 4.4. "W-W laminates", the Charpy impact properties of W-W laminated composites are compared with the properties of pure tungsten plate material. The plate material used for the benchmark experiments was a hot-rolled plate, as described above. The plate was in its as-received an in its recrystallised condition (annealed for 1 h at 2000°C (2273 K) in hydrogen). Specimens with dimensions of 1 mm x 3 mm x 27 mm, without notch, were cut by spark erosion. The specimens represent the L-S crack system.

An overview of the materials used for the benchmark experiments can be found in Table 5.

Table 5
Overview of non-composite materials used for benchmark experiments.

Section	Test method	Tungsten product	Grain size (S- x T- x L-direction)	Dimensions, orientation
4.1. "W-AgCu laminates"	Three-point bending tests	Hot- and cold-rolled plate	1 μm x 1 μm x 3 μm	1 mm x 10 mm x 20 mm, L-S, without notch
4.1. "W-AgCu laminates", 4.2. "W-Cu laminates"	Tensile tests	Severely cold-tolled foil	0.5 μm in the S-direction	0.1 mm x 2 mm x 13 mm (gauge length), 0°, tensile direction = rolling direction
4.1. "W-AgCu laminates", 4.2. "W-Cu laminates", and 4.3. "W-V and W-Pd laminates"	Charpy impact tests	Hot-rolled plate, as received	4 μm x 6 μm x 9 μm	KLST, L-S
		Hot-rolled plate, 10 h / 1000°C (1273 K)	Not measured, IPF see Fig. 47	
		Hot-rolled plate, 100 h / 1000°C (1273 K)	Not measured, IPF see Fig. 47	
		Hot-rolled plate, 1000 h / 1000°C (1273 K)	Not measured, IPF see Fig. 47	
		Hot-rolled plate, (1 h / 2000°C (2273 K), in hydrogen)	12 μm x 18 μm x 22 μm	
4.4. "W-W laminates"	Charpy impact tests	Hot-rolled plate, as received	4 μm x 6 μm x 9 μm	1 mm x 3 mm x 27 mm, L-S, without notch
		Hot-rolled plate, (1 h / 2000°C (2273 K), in hydrogen)	12 μm x 18 μm x 22 μm	

3.2. Mechanical tests

The mechanical properties of the tungsten laminated composites are identified by three types of tests. These are tensile, three-point bending, and Charpy impact tests.

3.2.1. Tensile tests

Tensile testing was conducted on a Zwick100 electro-mechanical test device. This step-motor screw-driven test machine has a 50 kN capacity load cell and was modified and combined with a furnace (RT - 1300°C (1573 K)) and a vacuum chamber (operation pressure: 10^{-6} mbar, viz. 10^{-4} Pa).
The tests were performed in displacement controlled mode at an extension rate of 0.1 mm/min. The extension rate was set by the speed of the cross-head of the load frame.
Longitudinal strain of specimens was measured using high-temperature strain gages (MAYTEC). The ceramic tips of the extensometer were positioned directly on the sample.
Engineering stress strain curves were obtained for each tensile test.

3.2.2. Three-point bending tests

Three-point bending tests were performed in the same test device as used for the tensile tests described above. Tests were conducted at room temperature, using a cross head speed of 10 mm/min. The support had a span of 10 mm. No extensometer was used. Load displacement curves were obtained from these tests.

3.2.3. Charpy impact tests

Instrumented Charpy impact tests were performed according to the standards DIN EN ISO 148-1 (2011) and DIN EN ISO 14556 (2006). These standards describe small-size specimens with dimensions of 3 mm × 4 mm × 27 mm, 1 mm notch depth, 0.1 mm notch root radius, and a support span of 22 mm (KLST type sample).
The Charpy impact test device is designed in a drop-weight style. To avoid oxidation, the whole Charpy testing machine is placed inside a vacuum vessel, which operates at typical pressures of about $1×10^{-3}$ mbar. The specimens are heated up together with the support, which allows a precise test temperature control. For more technical details of the Charpy impact test device, the reader is referred to Ref. [35].
The Charpy impact test results display the dissipated energy plotted against the test temperature. In this study, only one sample for each material condition and test temperature was tested.

At selected deformed Charpy impact test samples electron backscatter diffraction (EBSD) measurements and transmission electron microscope (TEM) analyses were conducted.

3.3. Electron microscopy

3.3.1. EBSD

Electron backscatter diffraction measurements were performed using a Zeiss Merlin scanning electron microscope (SEM) equipped with an EDAX Hikari camera. The

measurements were performed using an acceleration voltage of 20 kV and 10 nA probe current. For the mappings, a step size of 400 nm was chosen.

Points with a confidence index (CI) lower than 0.1 were removed during post-processing. Apart from grain CI standardisation, no cleanup of the datasets was performed. The orientations of the data points remained unchanged.

Misorientations exceeding 15° were considered as high angle grain boundaries (HAGBs) and are highlighted in black in the inverse pole figure (IPF) maps and in the grain orientation spread (GOS) maps, or in white in the kernel average misorientation (KAM) maps.

IPF maps are displayed with respect to the orthogonal sample directions. Grain orientation spread maps were obtained by calculating the average orientation individually for each grain. The orientation spread is then the average deviation between the orientation of each point inside the grain and the average orientation. KAM maps were calculated using only 1st neighbour points with misorientations between 0° and 5°.

3.3.2. TEM

A TEM specimen was prepared by the focused ion beam (FIB) method using an AURIGA CrossBeam system from Carl Zeiss AG. In the first step, a lamella was thinned to 200–250 nm thickness by FIB. In the second step, the lamella was flash polished at 12 V for 50 ms in order to remove the layer that has been amorphised during FIB preparation. The flash polishing removes preparation induced defects and thus allows TEM observations of dislocations and other lattice defects [36].

The TEM investigations were performed using a Tecnai F20 FEG transmission electron microscope from FEI. The microscope has an accelerating voltage of 200 kV and a 0.14 nm resolution limit. The tungsten structure was imaged using conventional bright field microscopy with an ORIUS SC600 camera.

3.3.3. Auger electron spectroscopy (AES)

A Physical Electronics PHI 680 Xi Field Emission Scanning Auger Nanoprobe was used for AES. The analyses were performed with 10 keV acceleration voltage and 10 nA beam current for the electron beam. The beam size was close to 40 nm (determined according to ISO 18516). To remove the carbon (C) and oxygen (O) contaminants from the surface and to make the grain structure visible, a 15-minute period of sputter etching was applied before data acquisition. For sputter etching an argon (Ar) ion beam with an ion current of 500 nA was used. During data acquisition, a continuous sputter etching setting with very low ion acceleration was used to prevent a redeposition with oxygen and carbon out of the vacuum.

For quantitative measurements in AES, peak-to-peak height measurements from the derivative spectra were used. The accuracies of such measurements are typically around ± 20 %.

To improve the measurement accuracy, the produced W-Pd laminates were first quantified precisely by a Camebax Microbeam electron probe micro analysis (EPMA) with a beam size of about 1 µm. The EPMA analyses were followed by spectral AES measurements for determination of the sensitivity factors. For both methods, measurement areas of ca. 10 µm x 10 µm were placed at specific positions of the tungsten and the palladium layer. With the data achieved in this way, the laminate samples can be used as calibration standards for further AES analyses. These data were used to converge the AES sensitivity factors by means of an approximation algorithm. For AES data reduction, the following sensitivity factors were used: W-Pd laminate: Pd (at 333 eV): 0.147; W (at 182 eV): 0.091. For the W-Cu and the W-V laminates it was not necessary to determine specific sensitivity factors because there was no diffusion found within the detection limits of the method.

4. Results and discussion

This section is organised as follows. To understand the fundamental deformation mechanisms associated with laminated composites, the results of a study entitled "W-AgCu laminates and the proof of principle" will be presented first. Afterwards we focus on W-Cu laminated plates and pipes, and discuss their technical maturity. Finally, the mechanical behaviour of laminated composites with a high melting point interlayer, such as W-V and W-Pd laminates, will be analysed and the potential of laminates without interlayers, W-W laminates, will be discussed.

4.1. W-AgCu laminates and the proof of principle

The aim of this section is to elucidate the deformation and fracture mechanisms of tungsten laminated composites. For such a study, the reactivity between the tungsten sheets and the interlayer material must be eliminated as a variable. Model systems comprised of mutually insoluble materials should be selected to avoid such reactions. In addition, a model system should consist of an interlayer material that has mechanical and physical properties at least somewhat representative of the material that is likely to be used in practical composites. Tungsten and an eutectic silver copper alloy were selected for this study because they fulfil the aforementioned requirements.

The sections below will address the following questions:
- What is the damage tolerance of W-AgCu laminates (L-S)?
- What are the main energy dissipation mechanisms in tungsten laminated composites (plastic deformation of the tungsten foils, plastic deformation of the interlayer sheets, creation of new surfaces)?
- What is the origin of the anisotropy of the Charpy impact properties (L-S, LT-S, T-S)?
- What is the reason for the improved Charpy impact properties of recrystallised W-AgCu laminates compared to their recrystallised plate material counterparts?
- What are the tensile properties of W-AgCu laminated composites?

4.1.1. The damage tolerance of laminated W-AgCu composites (L-S)

In this section we demonstrate the crack resistance and damage tolerance of W-AgCu laminates by performing three-point bending tests at room temperature.
The laminated specimens consist of eight layers of tungsten and seven layers of AgCu foil and represent the L-S crack system, without notch, 1.5 mm thickness. Benchmark experiments have been performed on pure tungsten plate material, L-S, without notch, 1 mm, thickness. These two materials can sustain approximately the same loads, making it a fair comparison. The results of the three-point bending tests are displayed in Fig. 4, where the load is plotted against the displacement of the striker (or more precisely: the displacement of the cross-head of the load frame).
It can be clearly seen that the plate material fails by fast fracture. The fracture behaviour of the laminated composite is rather different. After cracking of a tungsten ply the crack is arrested in the soft AgCu interlayer. This behaviour is indicated graphically by a serrated load–displacement curve.
The total number of steps in the load–displacement curve is more or less identical with the number of tungsten layers of the laminate. So each serration can be associated with the fracture of one tungsten ply.
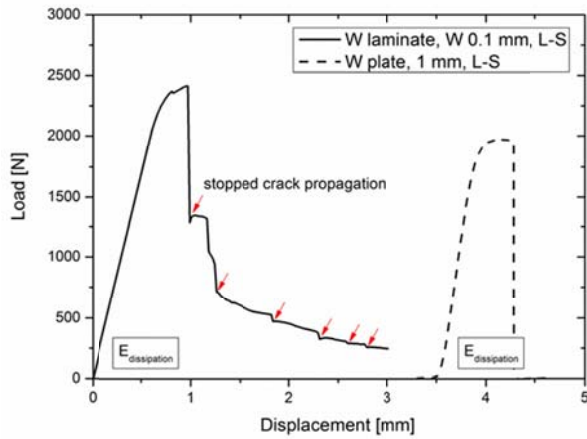
Fig. 4. Damage tolerance of laminated W-AgCu composites tested in the L-S orientation and at room temperature.

Finally, the area below the load–displacement curve is equivalent to the dissipated energy, which is higher for the laminated composite compared to the tungsten plate material. This finding will be confirmed in the next section, where Charpy impact properties will be described.

4.1.2. The anisotropy of the Charpy impact properties (L-S, LT-S, T-S) and the main energy dissipation mechanisms

In this section, we identify the origin of the anisotropy of the Charpy impact properties and elucidate the main energy dissipation mechanisms in tungsten laminated composites. We evaluate both the energy-temperature-diagrams and the fracture path to plot a map of energy dissipation mechanisms for laminated W-AgCu composites.

A laminated plate was made by stacking alternate layers of tungsten and AgCu. From this plate, KLST specimens representing the L-S, T-S, and LT-S crack systems were cut. Benchmark experiments were performed on pure tungsten plate material, L-S, KLST-type. The results of the Charpy impact tests are displayed in Fig. 5A, where the dissipated energy is plotted against the test temperature.
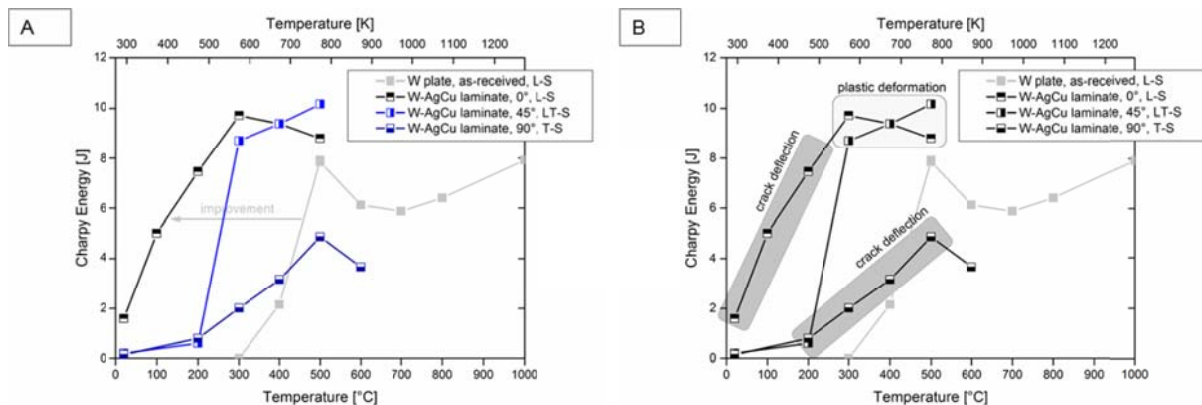

Fig. 5. A: The energy dissipation of tungsten laminated composites is highly anisotropic. B: Map of deformation and energy dissipation mechanisms for laminated W-AgCu composites. Crack deflection is triggered by dislocation activity.

18

It can be clearly seen that the brittle-to-ductile transition of the laminated composite occurs at a temperature which is approximately 300 K lower compared to the brittle-to-ductile transition of the benchmark plate material.

Furthermore, the dissipated energy is highly anisotropic. The difference in the energy dissipation behaviour of L-S and T-S samples can be explained as follows: The texture analyses of the severely cold-rolled tungsten foils show the highest intensities for the rotated cube component, {100}<011>. By considering the 90°-rotation symmetry of the rotated cube component (rotation around the <100> axis), the same mechanical properties in the rolling direction (0°) and perpendicular to the rolling direction (90°) would be expected (Fig. 3). In other words, by considering the crystallographic texture only, the Charpy impact properties of L-S and T-S samples should be identical. However Fig. 5A shows that this is not the case. Samples with an L-S crack system dissipate a considerable amount of energy even at a temperature of and below 300°C (573 K), whereas for the T-S oriented samples the amount of dissipated energy is rather low. As both types of samples possess the same crystallographic texture, this difference in Charpy energy can only be explained by the anisotropy of the grain shape. Fig. 3 provides an illustration of the top surface of the tungsten foils and displays the grain size anisotropy. The grain size in the rolling direction (L-direction) is larger than that perpendicular to the rolling direction (T-direction). This means that from the statistical point of view, the ligament plane of an L-S sample faces fewer low-toughness grain boundaries compared to the ligament plane of a T-S sample. So the difference in the energy dissipation behaviour of L-S and T-S samples is a grain shape effect.

By analysing the tested samples, further information about the fracture and deformation behaviour can be gained. Fig. 6 displays images of selected samples with respect to the sample orientation (L-S, LT-S, and T-S) and test temperature (RT, 300°C (573 K), and 500°C (773 K)).

Let us consider the LT-S samples first. At a test temperature of 200°C (473 K) and below, the samples dissipate less energy. The tungsten sheets fracture in a brittle manner, whereas the AgCu interlayers fracture in a ductile manner. Despite the ductile failure of the AgCu layers, the overall composite has very low energy dissipation at this test temperature (Fig. 5), indicating that the amount of dissipated energy caused by plastic deformation of the AgCu interlayer can be neglected when analysing the main energy dissipation mechanisms in laminated composites. Samples tested at room temperature show very straight cracks in the tungsten sheets. This manifestation is associated with a fracture along the primarily cleavage plane of tungsten, i.e. the {100} cleavage plane. The crack propagation plane is directly aligned with the preferred {100} cleavage plane, allowing for the straight, brittle failure of the tungsten layers.

At a test temperature of 300°C (573 K) and above, the deformation mechanisms suddenly change. Now the samples can dissipate a considerable amount of energy. The tested samples are characterised by plastic deformation of the tungsten and the interlayer sheets. Only the most highly stressed tungsten plies failed. The fracturing of these tungsten plies is manifested in a zig-zag shape following the {110} planes, which are the second cleavage planes for tungsten. This shows that in the range of 200°C (473 K) to 300°C (573 K) a change of the preferred cleavage plane takes place. This change is accompanied by the onset of plastic deformation of the tungsten foils.
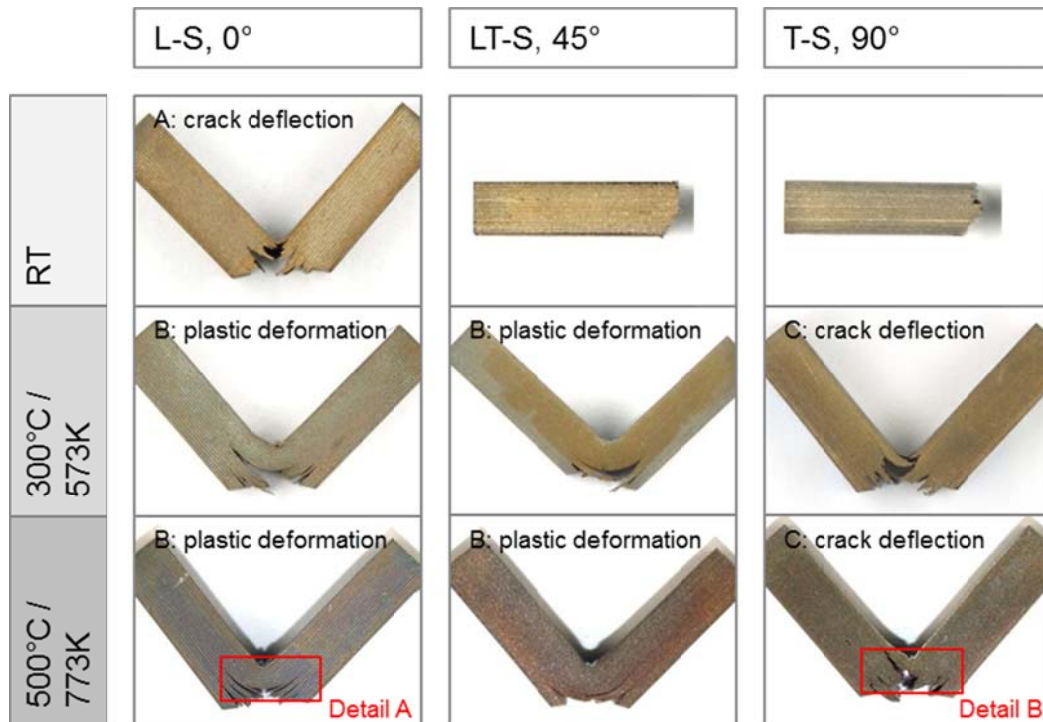
Fig. 6. Images displaying the fracture and deformation behaviour of W-AgCu laminates with respect to the test temperature and sample orientation.

The fracture behaviour of L-S samples is rather different. At room temperature, the fracture path does not penetrate straight along the ligament plane. Moreover the fracture path is deflected and deviated. This crack deflection takes place both (i) at the interface of the tungsten sheets and the interlayer and (ii) in the tungsten sheet by intergranular delamination. The energy dissipation mechanism associated with this type of fracture behaviour is the creation of new surfaces. With increasing test temperature, the number of tungsten sheets that deform plastically increases. However the most stressed tungsten plies still fail (Fig. 7, Detail A).

Finally, the crack path analyses of samples with a T-S crack system provide further insights. At room temperature, the crack path penetrates along the ligament plane in a very straight line; there is almost no crack deflection. With increasing test temperature, the mechanism of crack deflection becomes more pronounced (Fig. 7, Detail B). This indicates that the mechanism of crack deflection is a thermally activated process. More precisely, we infer that the onset of crack deflection is caused by the plastic deformation of the tungsten foils, which in turn is thermally activated.
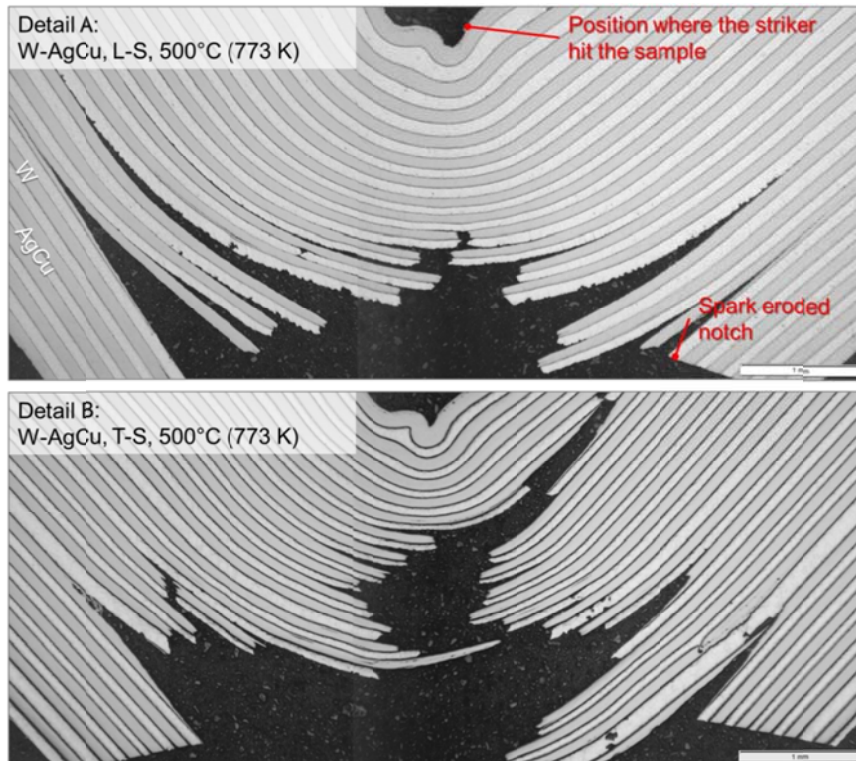
Fig. 7. Optical micrographs showing samples representing (i) plastic deformation (Detail A) and (ii) crack deflection (Detail B) as the main deformation mechanism.

This section yields the following major results: The fracture and deformation behaviour of W-AgCu laminates is dominated by the mechanical behaviour of the tungsten foils. The fracture behaviour can be explained by microstructural features of the tungsten foils such as the preferred cleavage planes and the grain size anisotropy (Fig. 3). Furthermore, the main energy dissipation mechanism has been identified to be the plastic deformation of the tungsten foil (Fig. 5B). It is determined that contributions to the total amount of dissipated energy from the plastic deformation of the interlayer or the creation of new surfaces can be neglected.

While in this section the laminates were built of tungsten sheets with an ultrafine-grained microstructure, the laminates in the next section will be made of foils in the recrystallised condition.

4.1.3. Unravelling the deformation mechanisms in recrystallised W-AgCu laminated composites

The aim of this section is to introduce a very important deformation mechanism associated with laminated composites. The mechanism is based on the dislocation-interface interaction and can be described as dislocation absorption/transmission at the body-centred-cubic (bcc)–face-centred-cubic (fcc) interface.

It is also common knowledge that moving dislocations are annihilated at the crystal surface [37]. Here we will show that this type of dislocation annihilation impacts on the tensile properties of tungsten foils. In particular, for foils that are characterised by a high surface-to-volume ratio and especially for foils with a coarse-grained microstructure, the mechanism of dislocation annihilation on the surface severely impacts the mechanical response. Furthermore we will show that for tungsten laminated composites, the dislocation-interface

interaction (e.g. absorption and transmission of dislocations at the interface) impacts on the Charpy properties.

The Charpy impact properties of recrystallised W-AgCu laminates are extraordinary and demand an in-depth discussion. To provide a sound basis for such a discussion we will first present and discuss the tensile behaviour of recrystallised tungsten foils and plates.

Fig. 8A displays the tensile behaviour of recrystallised tungsten plates (1 mm thickness, 1 h at 2000°C (2273 K) in hydrogen) and foils (0.1 mm thickness, 1 h at 2000°C / 2700°C (2273 K / 3073 K) in hydrogen). Tensile tests were performed at 600°C (873 K). For more details the reader is referred to Ref. [34]. The engineering stress–strain curve of the tungsten plate is characterised by a pronounced hardening and a total plastic strain of about 28 %. The deformation curve is smooth. The tensile behaviour of the recrystallised foil is very different. The total plastic strain is in the same range as that of the recrystallised plate material. However, the engineering stress–strain curve shows severe serrated yielding. This behaviour is astonishing as both samples have the same metallic purity (> 99.97 wt % W) and microstructure (grain size). Their main difference is their thickness and thus their surface-to-volume ratio. So the following question arises: Which microstructural mechanisms cause the plastic instabilities (yield drops, serrated flow) of tensile tested coarse-grained tungsten foils? Note: recrystallised tungsten foils can be regarded as quasi-single crystals, as their microstructure contains several grains that reach from one surface of the foil to the other. For real single crystals with macroscopic dimensions and tested in a tensile test, the stress–strain curves are smooth and do not show serrated yielding [4]. This is a further hint that the origin of the serrated flow of the recrystallised foils must be somehow linked with their surface-to-volume ratio and the dislocation-surface-interaction.
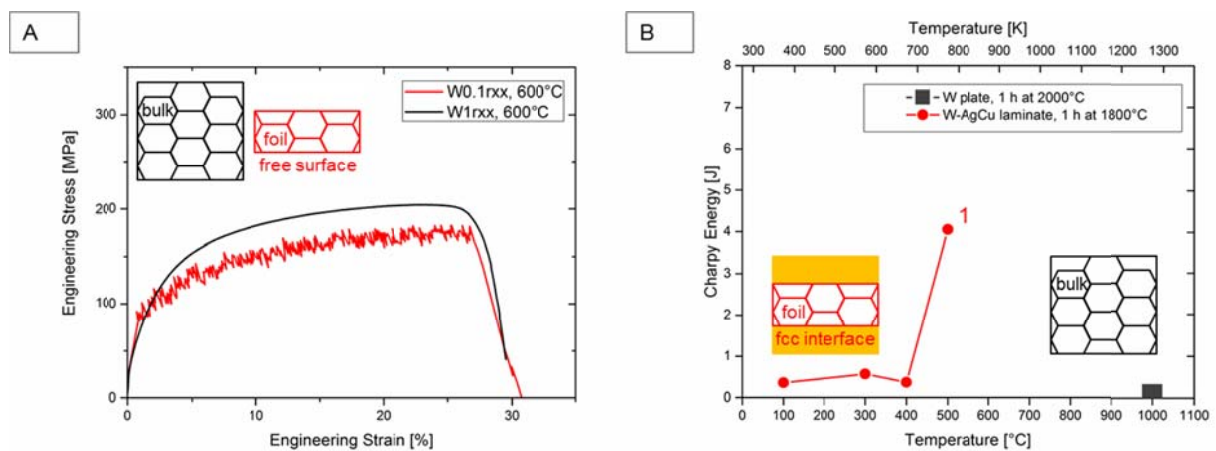

Fig. 8. The interaction between dislocations and the crystal surface or, respectively, the bcc–fcc interface impacts on the mechanical properties. A: The tensile behaviour of recrystallised tungsten plates and foils is very different. Recrystallised foils show plastic instabilities, which are most likely caused by strain localisation and propagation (strain bursts) followed up by dislocation-surface-interactions (dislocation annihilation). B: The Charpy impact properties of recrystallised W-AgCu laminates may benefit from the bcc–fcc interface which may allow the absorption and transmission of dislocations.

At this point it is worth recalling the mechanisms that cause serrated yielding and plastic instabilities. The problem can be traced back to two major types of plastic deformation. These are (i) the interactions between moving dislocations and solute atoms [37], and for pure metals, (ii) the modes of strain localisation and propagation (strain bursts) [38, 39].
Serrated flow may be caused by solute atoms. As any motion of solute atoms is strongly temperature dependent, the ranges of low (relaxation of solute atoms in the dislocation core

region), intermediate (formation and breakaway from impurity clouds), and high temperatures (dragging of impurity clouds) can be distinguished.

The intermediate temperature region is also referred to as the "Portevin–Le Chatelier (PLC) region". In this region, fluctuations and serrations in the load curve occur. This phenomenon is the PLC effect and can be described as follows: In the PLC region, the temperature is high enough for clouds of solute atoms (Cottrell atmospheres) to be formed around the dislocations. This locking of dislocations and their breakaway from the impurity clouds is the reason for the serrations in the load curve.

Beyond the PLC region, and thus at high temperatures, the deformation curve is smooth again. Now the diffusional processes are fast enough to establish a solute cloud at dislocations immediately after breakaway from their obstacles.

Serrated flow may also be caused by various modes of strain localisation and propagation. Ritschel et al. [39] and Luft et al. [38] reported the tensile behaviour of predeformed molybdenum single crystals. The deformation curve shows pronounced work softening accompanied by serrations. The authors associated the yield drops with the formation of dislocation-free cells. The mechanisms described by Ritschel et al. [39] and Luft et al. [38] can most likely not be applied to the recrystallised tungsten foils as the manifestation of the serrations are severely different.

A popular classification of serrations in substitutional alloys can be found in Brindley and Worthington's work [40], which distinguishes between type A, B, and C serrations. Type A is associated with nearly smooth continuous propagation of a deformation band over the specimen length with a sharp serration whenever a new band is initiated at one end of the specimen. Type B corresponds to the intermittent propagation of a narrow plastic zone. In type C serrations, extremely large stress drops occur, with plastic bands appearing at random within the specimen.

By considering this theoretical background and comparing the manifestation of load drops of the recrystallised tungsten foils with serrations reported in literature, we finally arrive at the conclusion that the physical origin of the plastic instabilities of the load curve from Fig. 8A is most likely caused by strain localisation and propagation (strain bursts). We classify the plastic instabilities as type B serrations. As the yield drops occur for the recrystallised foils (0.1 mm thickness) but not for the recrystallised plates (1 mm thickness) and not for macroscopic single crystals, we infer that the origin of the serrated yielding may be strain localisation and propagation (strain bursts) followed up by dislocation-surface-interactions (dislocation annihilation).

Dislocations-surface-interactions impact on the tensile properties of thin tungsten foils. In the next part, we will show that dislocation-interface interactions impact the Charpy properties of tungsten laminated composites as well.

A laminated plate was made by stacking alternate layers of recrystallised tungsten (1 h at 1800°C (2073 K)) and AgCu. From this plate, KLST specimens with an L-S crack system were cut. Benchmark experiments were performed on recrystallised tungsten plate material (1 h at 2000°C (2273 K)), L-S, KLST-type. The results of the Charpy impact tests are displayed in Fig. 8B, where the dissipated energy is plotted against the test temperature.

The results show that the BDT of the recrystallised laminate occurs at a temperature which is at least 500 K lower than the BDT temperature of its recrystallised plate material counterpart (at the maximum tested temperature of 1000°C (1273 K), the recrystallised plate does not have any measurable energy absorption, indicating that its BDT is higher than 1000°C (1273 K)). This improvement is astonishing as the recrystallised tungsten foils and the recrystallised tungsten plate have the same metallic purity (> 99.97 wt % W) and microstructure (grain size). This raises the question of what mechanisms cause this enormous decrease of the BDT temperature. To elucidate the physical origin of this behaviour we will now first present in-depth SEM and TEM analyses of the Charpy impact test sample representing the lowest temperature of the ductile regime (indicated by "1" in Fig. 8B). This is followed by a brief overview of the current discussion on the controlling mechanisms of the BDT and crack-tip

plasticity. By making use of both the electron microscopy analyses and the theoretical background, we will finally arrive at a mechanism-based assumption.

Fig. 9 displays the Charpy impact test sample composed of recrystallized tungsten and AgCu interlayers tested at 500°C (773 K), indicated by "1" in Fig. 8B. The SEM image shows a plastically deformed sample. So the dissipated energy of 4.1 J is caused by plastic deformation of the recrystallised tungsten foils and the AgCu interlayers and not by any other energy dissipation mechanisms such as the creation of new surfaces. This makes it possible to focus on dislocation activity when discussing the impact properties.

Furthermore, Fig. 9 displays regions where in-depth SEM analyses have been performed. These regions are referred to as Detail A and Detail B, representing the sample part where the highest compression stress occurred, as well as Detail C, representing the region of the highest tensile stress.
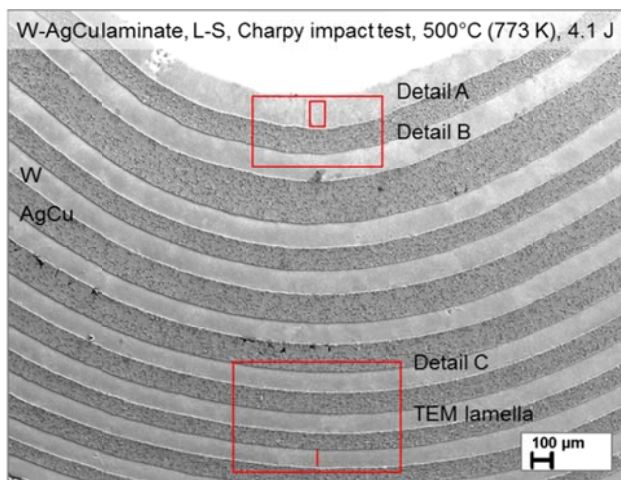

Fig. 9. SEM image of the Charpy impact test sample, indicated by "1" in Fig. 8B. The sample was composed of recrystallized tungsten and AgCu interlayers. The red frames show areas where detailed EBSD analyses have been performed.

An EBSD analysis of Detail A can be found in Fig. 10. The inverse pole figure map clearly demonstrates severe gradients within the grains, which can be referred to pronounced dislocation activity. This impression is confirmed by the grain orientation spread map. This map represents gradients within regions surrounded by high angle grain boundaries. Finally, Fig. 10 displays the kernel average misorientation map. This map indicates areas or bands with increased misorientation (highlighted in green). These bands are of the greatest interest and are displayed in more detail in Fig. 11.
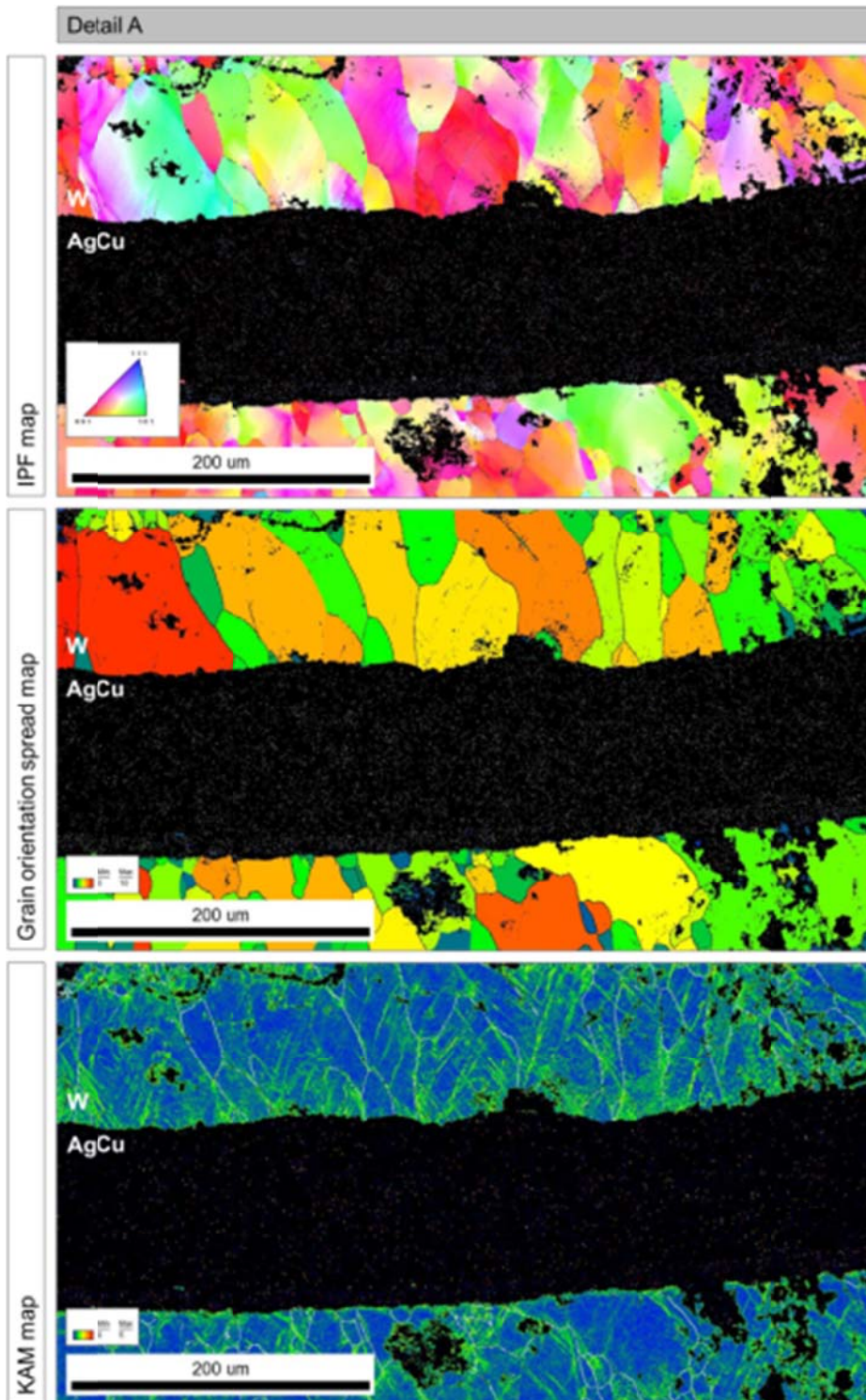
Fig. 10. EBSD analyses of Detail A. Inverse pole figure (IPF) map, grain orientation spread (GOS) map, and kernel average misorientation (KAM) map.

Fig. 11 gives the EBSD analyses of Detail B, as referred to in Fig. 9. Again the inverse pole figure map displays severe colour gradients which visually represent the orientation gradients. The kernel average misorientation map clearly indicates areas of increased misorientation. These areas have the shape of a band and appear systematically by a parallel shift. By plotting a misorientation profile and performing a point-to-point and point-to-origin analysis, the areas of increased misorientation can be identified as subgrain boundaries (misorientation < 5°; point-to-point analysis shows a peak) and localised strain

25

(point-to-origin analysis shows a peak). It is recalled that strain localisation (strain burst) followed up by dislocation annihilation at the foil surface is the mechanism that we assumed to be responsible for the serrated flow of the tensile tested recrystallised tungsten foils.
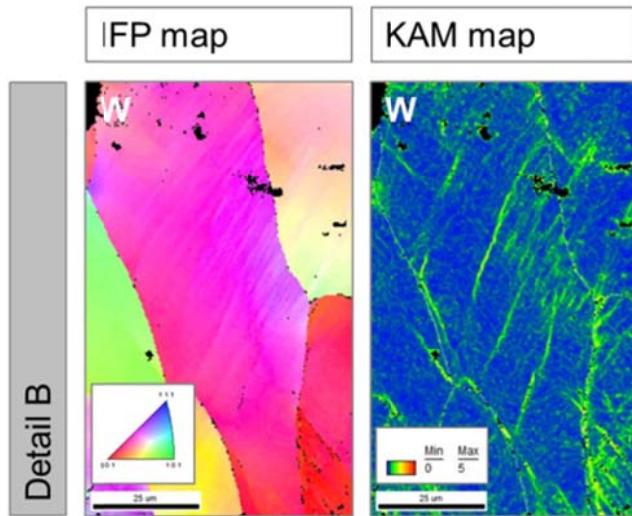

Fig. 11. EBSD analyses of Detail B. The areas of increased misorientation indicate subgrain boundaries and localised strain.

From the assessment of Detail C (representing the region where the highest tensile stress occurred), the same main conclusion can be derived (Fig. 12). The inverse pole figure map shows gradients too. However, the crystallographic texture of the recrystallised tungsten foils in their undeformed condition (highest intensities for the rotated cube component, {100}<011> [31]) can still be inferred. Note that the IPF map in Fig. 12 is displayed with respect to the normal direction of the tungsten foils. From the grain orientation spread map, further interesting insights can be gained. With increasing distance from the most highly stressed region, the misorientation inside the grains decreases. This is indicated by the increase of areas coloured in blue with increasing distance from the notch root.
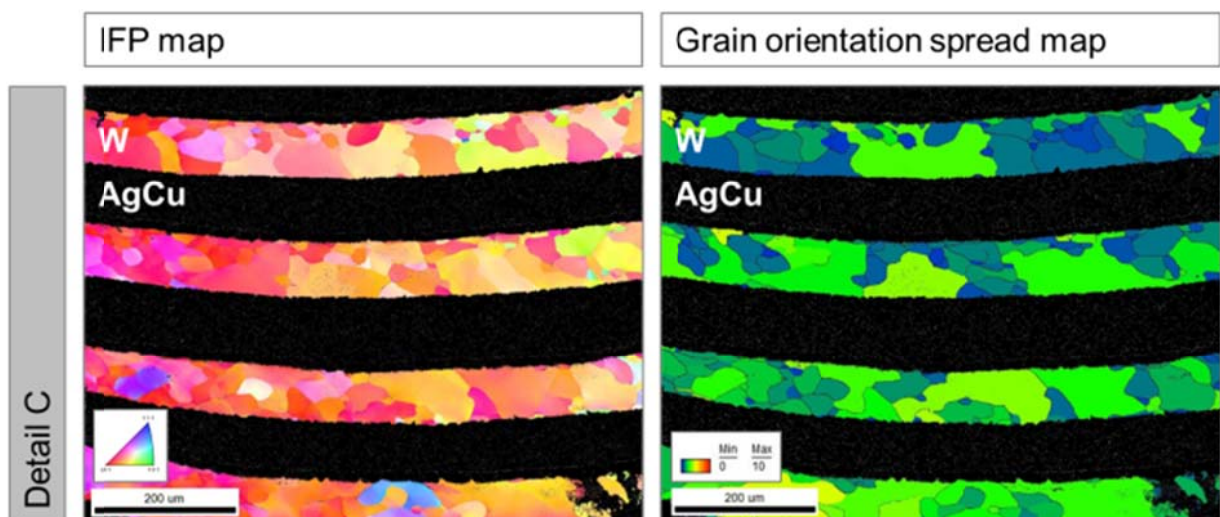

Fig. 12. EBSD analyses of Detail C. The IPF map is displayed with respect to the normal direction of the tungsten foils. Furthermore, the grain orientation spread map displays a decrease of misorientation with increasing distance from the notch root.

The EBSD analyses provided an overview impression of the microstructure of the deformed Charpy test samples. For more details on the dislocation activity, a TEM analysis was performed and will be presented in the next paragraph.

A TEM lamella was prepared in order to characterize the deformed microstructure. The lamella was taken out from sample "1" from the region where the highest tensile stress occurred. The position of the TEM lamella as well as its orientation relative to the Charpy impact test sample can be found from Figs. 13A-C. The red frame in Fig. 13C gives the position from which the TEM bright-field images have been taken. An overview of the deformed microstructure can be derived from Figs. 13D and E. These images display severe dislocation activity and thus confirm that the energy dissipation of sample "1" is at least somewhat caused by plastic deformation. In contrast, nearly no dislocations are seen in the recrystallised tungsten material in the undeformed condition, as seen in a bright-field TEM image in Ref. [31].
Further insights into the dislocation arrangements can be gained from Figs. 13F and G. These images display detailed views representing areas with an inhomogeneous (Fig. 13F) and a homogeneous (Fig. 13G) dislocations distribution. Fig. 13F shows that close to the grain boundary the dislocation density is low, whereas at a distance of about 500 nm and parallel to the grain boundary, an area of increased dislocation density can be found.
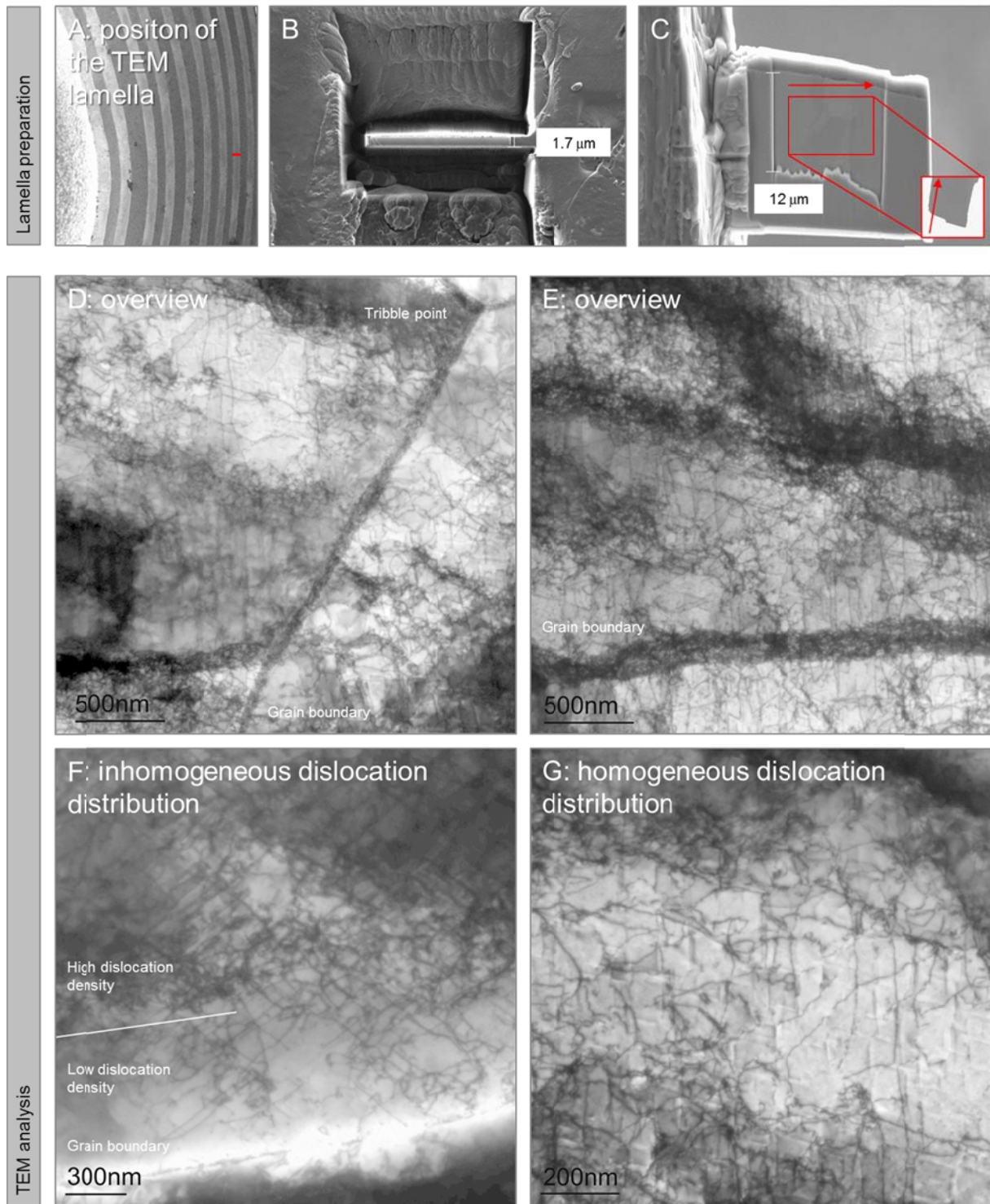
Fig. 13. A TEM lamella was prepared in order to analyse the deformed microstructure close to the notch root of sample "1" (A-C). Bright-field images provide an overview (D, E) as well as a detailed view (F, G) of the dislocation arrangements.

The TEM analysis clearly demonstrates that significantly more TEM analyses are needed to clearly display a mechanism-based idea of the manifestation of the various dislocation arrangements. The main result obtained from the TEM investigation is that the main energy dissipation mechanism of sample "1" can be traced back to dislocation motion. The main question to address is why dislocation motion is favoured in tungsten sheets of a recrystallised W-AgCu laminate compared to its recrystallised plate material counterpart. We

will provide an assumption to this question by considering issues of the brittle-to-ductile-transition and crack-tip plasticity next.

The elucidation of crack-tip plasticity is the key to identifying the mechanisms controlling the brittle-to-ductile transition. Crack-tip plasticity is governed by the emission of dislocations, which is a two-step process starting with the nucleation of dislocations followed by the dislocation glide.

The question of whether the BDT is determined mainly by dislocation nucleation or by dislocation mobility has been the subject of several experimental and theoretical investigations. Models describing the BDT as a nucleation-controlled event assume that the lack of active dislocation sources prevents the emission of a sufficient number of dislocations to provide effective shielding [41, 42]. Models describing the BDT as a mobility-controlled event assume that dislocations are generated in large numbers but cannot leave the crack-tip region fast enough and thus inhibit the instantaneous nucleation of further dislocations [43, 44]. The latter model is what we make use of to describe the deformation behaviour of the Charpy impact sample "1".

Fracture will occur if the Griffith critical stress intensity, K_{IC}, is reached at the crack tip [45]. The externally applied stress intensity, $K_{applied}$, may differ from the effective stress intensity at the crack tip, $K_{effective}$, as the effective stress intensity at the crack tip is affected by the elastic stress fields from dislocations (Fig. 14A).

Transmission electron microscopy analyses revealed particular features of the crack-tip region, such as the dislocation free zone (DFZ) [46]. The appearance of a dislocation free zone at the crack tip can be examined by considering the elastic interaction between a crack and a dislocation. The shear stress, σ_{yz}, on a screw dislocation emitted from a sharp mode III crack along the coplanar slip plane is given near the crack tip by

$$\sigma_{yz}(x) = \frac{K_{applied,III}}{(2\pi x)^{1/2}} - \frac{\mu b}{4\pi x} \tag{4}$$

where x is the distance from the crack tip to the dislocation, $K_{applied,III}$ is the applied stress intensity, μ is the shear modulus, and b is the Burgers vector. The first term in Eq. (4) represents the elastic crack stress and the second term is the image stress. These two stresses are plotted in Fig. 14A as a function of x. The origin of the dislocation free zone can be explained as follows: if a shielding dislocation is emitted from the crack tip, it is expected to move away from the crack tip. The dislocation will come to a rest at x_1, where the total stress on the dislocation is balanced by the friction stress of the lattice, σ_f. The region between the crack tip and x_1 is dislocation free and is referred to as the dislocation free zone (DFZ).

Eq. (4) describes the shear stress on a single screw dislocation. The description of a stress field of the crack-tip equilibrium configuration that considers (i) the shielding by a group of dislocations, (ii) the applied stress, σ_a, and (iii) a crack of finite length is mathematically more complicated. Details on the stress field of a crack-tip equilibrium configuration can be found in Ref. [46].

It can be seen from Fig. 14B that the stress field has a singularity at the crack tip and that the stress decreases to the friction stress, σ_f, at the end of the dislocation free zone (position x_1). The stress remains at the friction stress, σ_f, throughout the plastic zone as no work-hardening is assumed (position a). The stress decreases to the applied stress, σ_a, in the elastic zone outside the plastic zone. The distance from the crack tip to the end of the plastic zone, a, will now play an important role in the interpretation of the deformation behaviour of the Charpy impact sample "1".
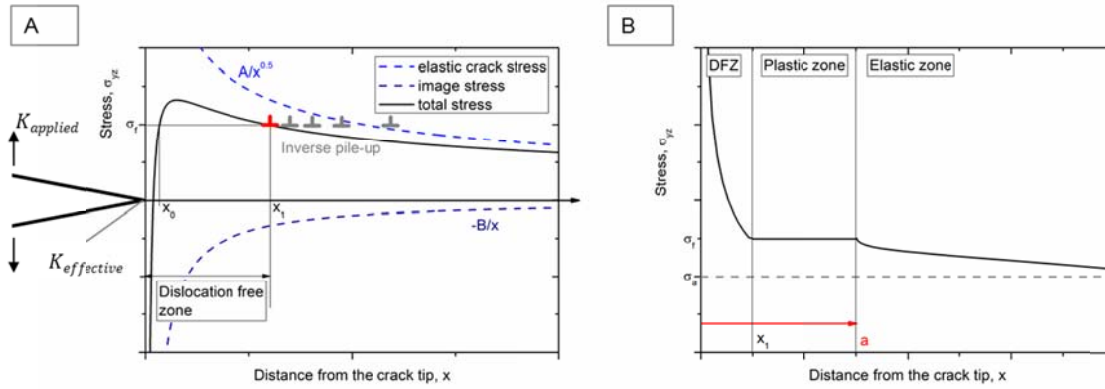
Fig. 14. A: The dislocation free zone can be explained by considering the stress on a dislocation near the crack tip (here, the mode III crack along the coplanar slip plane). The total stress is obtained by adding the elastic crack stress and the image stress. The position of the inverse pile-up is shown in grey. The stress field of the dislocations forming the inverse pile-up is not considered in Eq. (4). x_0 denotes the critical distance for a nucleation criterion. B: Stress field ahead of the crack tip, in equilibrium configuration, at $y = 0$ as a function of x. A distinction between the dislocation-free, plastic, and elastic zone is made.

The main question is why the BDT of the recrystallised laminate occurs at a temperature which is several hundreds of K lower than that of its recrystallised plate material counterpart. The recrystallised tungsten foils and the recrystallised tungsten plate have the same metallic purity (> 99.97 wt % W) and microstructure (grain size). What distinguishes both is the fact that the laminated composite possesses several bcc–fcc interfaces. These interfaces may allow the absorption and transmission of dislocations.

We finally arrive at the following assumption. We assume the BDT to be controlled by dislocation motion. If the dislocations cannot leave the crack-tip region fast enough, the instantaneous nucleation of further dislocations is inhibited and so is the shielding of the crack tip. The effective stress intensity at the crack tip, $K_{effective}$, will reach the Griffith critical stress intensity, K_{IC}, and fracture occurs.

The situation may appear slightly different in the laminated composites. Again, dislocations are generated in large numbers at nucleation sites in the tungsten sheet. Both a dislocation free zone and a plastic zone are formed ahead of the crack tip (Fig. 14B). We assume that if the plastic zone reaches the bcc–fcc interface, the dislocations may be absorbed or transmitted at the bcc–fcc interface. Due to the absorption/transmission of the dislocations at the interface, further shielding dislocations can be nucleated at the crack tip. This in turn decreases the effective stress intensity at the crack tip, $K_{effective}$, and so on.

From this it can be inferred that the BDT in recrystallised laminated W-AgCu composites is determined by the question of whether or not the distance from the crack tip to the end of the plastic zone, a, reaches the bcc–fcc interface, or in other words, whether or not the dislocations reach the tungsten-interlayer-interface. This question is in turn closely related to the dislocation velocity, which is a function of the resolved shear stress and temperature. If our assumption is true, then a decrease in tungsten layer thickness should result in a further decrease of the BDT temperature.

To furnish evidence, further well-defined experiments are essential.

What we have neglected in the discussion so far is the impact of residual stresses on the mechanical properties of laminated composites. The next section will show that at least for the tensile properties of W-AgCu laminates, residual stressed do not have a pronounced impact.

4.1.4. Tensile properties of W-AgCu laminated composites

In this section, we present the tensile properties of W-AgCu laminated composites. The laminates consisted of three layers of 100 μm-thick tungsten foil (as-received condition) and two layers of 100 μm-thick AgCu foil, and had a total thickness of 0.5 mm. Benchmark experiments were performed using cold-rolled tungsten foils with a thickness of 100 μm. All samples were aligned in such a way that the tensile loading direction was congruent with the rolling direction of the tungsten foils (0°).

The results of the tensile tests can be seen in Figs. 15A and B. In Fig. 15A the tensile properties of technical pure tungsten foils are displayed. The tests have been performed at room temperature and at 600°C (873 K). It is noteworthy that the ultrafine-grained tungsten sheets show plastic deformation at room temperature. Furthermore, it is important to note, that the foils possess a low hardenability. The stress-strain curve can be characterised by a high hardening rate at the beginning of plastic deformation. This is followed up by a very flat manifestation of the stress-strain curve which indicates that the nucleation and annihilation of dislocations seems to be somehow balanced out. Finally, the uniform elongation, A_u, is relatively high. The elongation to fracture, A, is a function of the sample's thickness, however the uniform elongation, A_u, is almost independent of the sample's thickness [47].
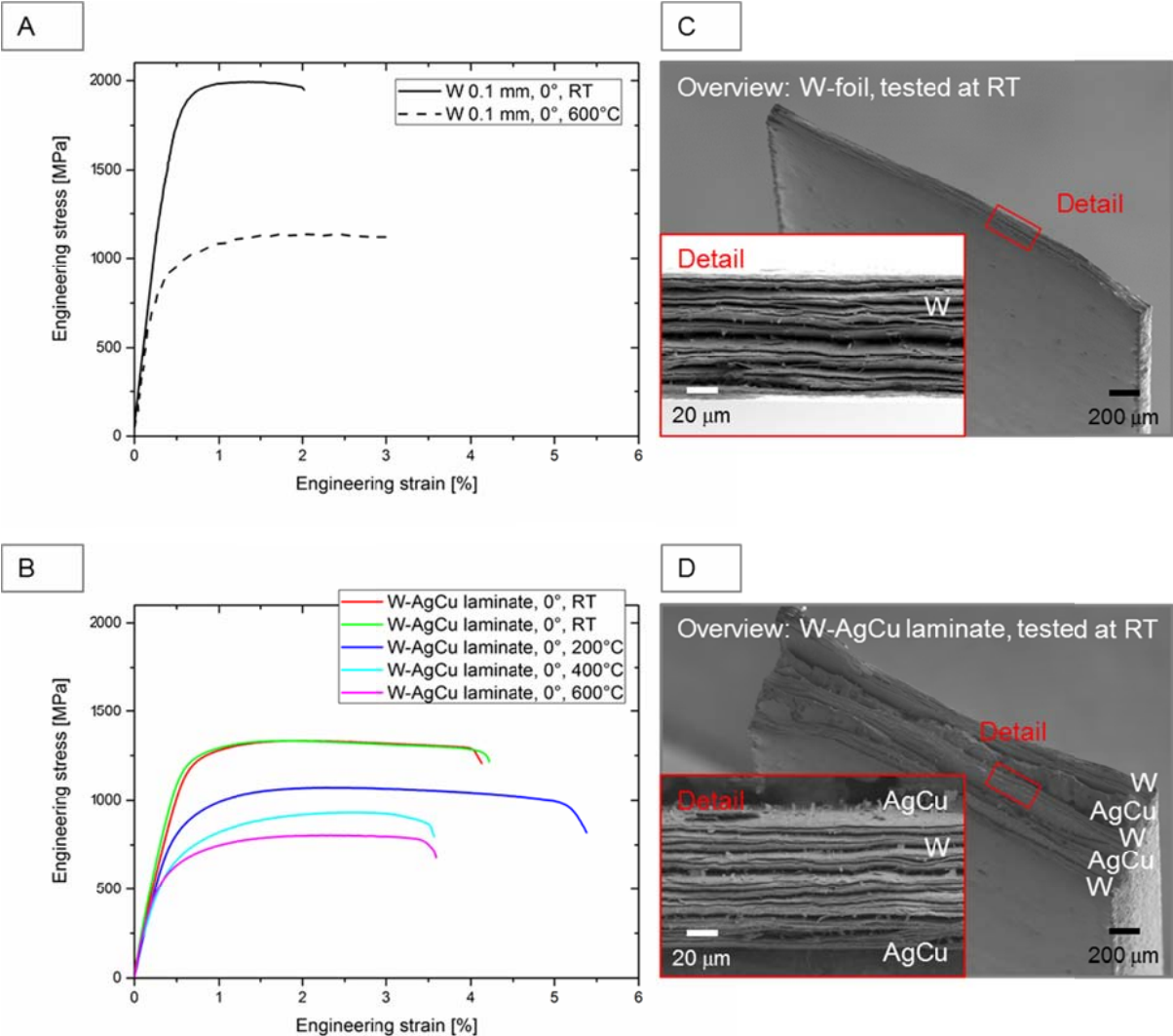

Fig. 15. A: Tensile properties of pure tungsten foils serving as a benchmark. B: Results of tensile tests performed on W-AgCu laminated composites. C, D: Fractured surfaces of samples tested at room temperature.

31

The results of the tensile tests of W-AgCu laminated composites can be seen in Fig. 15B. Tensile tests have been performed at room temperature, 200°C (473 K), 400°C (673 K), and 600°C (873 K). When comparing the results of the laminated composites with the results of the pure tungsten foils, it can be concluded that (i) the ultimate strength of the laminated composites is about 60 % of the ultimate strength of the pure tungsten foils, which is reasonable when considering that the laminated composites consist of 60 vol % tungsten and 40 vol % AgCu, (ii) the plastic strain increases slightly, and (iii) the fractured surfaces of the pure tungsten foils and the fractured surfaces of the tungsten sheets of W-AgCu laminated composites show the same characteristics (Figs. 15C and D). More or less, the stress-strain-curves of the tungsten foils and the W-AgCu laminated composites are very similar. This indicates that the tensile properties of the W-AgCu laminated are dominated by the plastic deformation of the tungsten foils and that the impact of the AgCu interlayer or the impact of residual stresses can be neglected.

In this section, we reported the results of a model system made of mutually insoluble materials: W-AgCu. In the next section, a further model system of mutually nonreactive materials, tungsten and copper, will be investigated.

4.2. W-Cu laminates

This section is organised as follows. The evolution of the Charpy impact properties during ageing (10, 100 and 1000 h at 1000°C (1273 K) in vacuum) will be presented first. This comprises an analysis of the evolution of the microstructure of the tungsten sheets (hardness, SEM) and of the tungsten-copper interface (AES). Afterwards, we will focus on the tensile properties of the laminates. Finally the use of W-Cu laminates plates and pipes for high heat flux components will be discussed based on the latest results of high heat flux test campaigns.

The following sections will address the questions:
- How do the Charpy impact properties change through annealing for 10, 100 and 1000 h at 1000°C (1273 K)?
- Is there a relation between the evolution of the hardness of the tungsten sheets and the evolution of the BDT temperature of the laminates?
- What is the role of the copper interlayer in the unique tensile properties of W-Cu laminates?
- What is the performance of W-Cu laminated pipes in a high heat flux test?

4.2.1. Charpy impact properties of W-Cu laminates

The aim of this section is to identify the evolution of the fracture mechanisms of aged W-Cu laminated composites. This is undertaken by a comparison of the evolution of the microstructure with the evolution of the Charpy impact properties.

The laminated specimens consist of 20 layers of tungsten and 19 layers of copper foil, and represent the L-S crack system, KLST-type. Four material conditions are considered: (i) the as-produced condition and the annealed conditions (ii) 10 h, (iii) 100 h, and (iv) 1000 h at 1000°C (1273 K) in vacuum.

4.2.1.1. Evolution of the microstructure of the tungsten sheets (hardness, SEM, AES)

The evolution of the hardness of the W-phase is displayed in Fig. 16, where the hardness (HV0.1) is plotted against the annealing time in a logarithmic scale. The diagram clearly shows the exponential evolution of the hardness, represented by a straight line in the semi-logarithmic plot. The evolution of the hardness allows the kinetics of the recrystallisation processes in the tungsten foil to be determined. This issue will be treated by the end of this section.
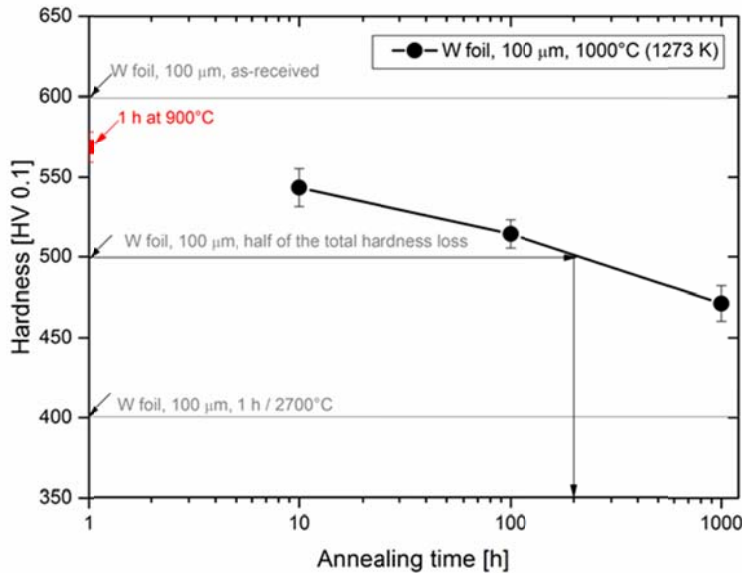

Fig. 16. Semi-logarithmic plot of the evolution of the hardness in tungsten sheets of the material conditions (i) as-produced, and annealed for (ii) 10 h, (iii) 100 h, and (iv) 1000 h at 1000°C (1273 K). The results of these isothermal heat treatments allow determining an apparent activation energy for half of the total hardness loss.

A further impression of the evolution of the microstructure can be gained from Fig. 17. This series of SEM images presents the microstructure of the tungsten sheets after various isothermal heat treatments. Furthermore, this figure gives some insight into the recrystallisation behaviour of the tungsten sheets.
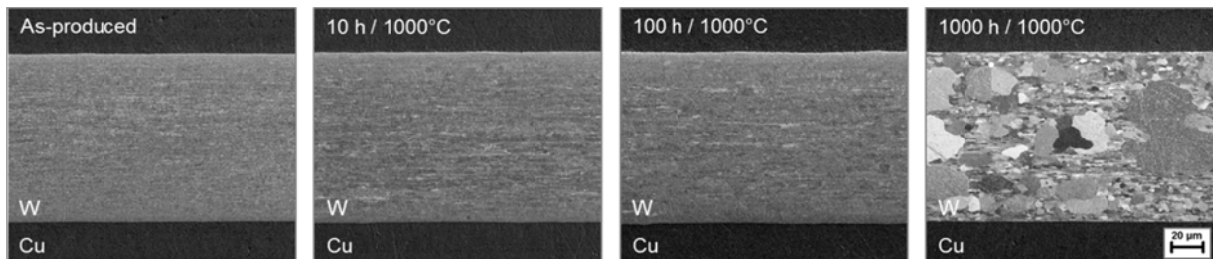

Fig. 17. SEM images displaying the evolution of the tungsten microstructure of a W-Cu laminated composite through annealing.

Fig. 17 also confirms the mutual nonreactivity of tungsten and copper, as the interface of tungsten and copper appears to be sharp even after annealing for 1000 h at 1000°C (1273 K).

In order to assess the tungsten-copper interface in more detail, AES linescans have been performed. The results are shown in Fig. 18, where the atomic concentration of tungsten is plotted against the position of the measurement. For the AES linescans, a step size of about 1.5 μm was used. The deviated result of the curve representing the tungsten-copper interface after 100 h at 1000°C (1273 K) can be attributed to the size of the electron beam

33

diameter (40 nm, according to ISO 18516). At the data point referred to as "1" in Fig. 18, the electron beam diameter partly covered and thus partly excited the copper phase.

With respect to the electron beam diameter and the step size of the AES analysis, no diffusion of tungsten into copper and vice versa was detected.
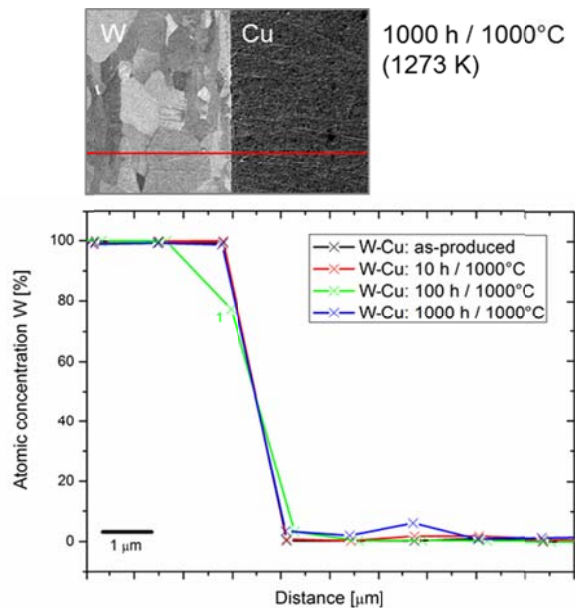

Fig. 18. AES line scans confirm the mutual nonreactivity of tungsten and copper.

The mutual nonreactivity of tungsten and copper makes W-Cu laminates an excellent model material for the elucidation of deformation and fracture mechanisms of tungsten laminated composites.

4.2.1.2. Evolution of the Charpy impact properties

In Section 4.1. "W-AgCu laminates and the proof of principle", we came to the conclusion that the main energy dissipation mechanism in tungsten laminated composites is the plastic deformation of the tungsten foils. Therefore, the key issue for understanding the Charpy impact properties is to identify the deformation mechanisms of the tungsten foils.

With respect to the microstructure we distinguish between (i) deformation mechanisms associated with the cold-rolled, ultrafine-grained microstructure (assumption: ordered glide of screw dislocations that move along the HAGBs channels, confined plastic slip [48]) and (ii) deformation mechanisms associated with coarse-grained thin foils (assumption: strain localisation and propagation (strain bursts) followed up by dislocation-surface-interactions (dislocation annihilation), Fig. 8A).

The change of the Charpy impact properties through annealing for 10, 100 and 1000 h at 1000°C (1273 K) is displayed in Fig. 19. As a type of benchmark experiments, Fig. 19 also includes the Charpy impact results obtained from as-produced W-AgCu laminates and recrystallised W-AgCu laminates.

For the ease of discussion, the graph representing the properties of the as-produced W-AgCu laminates is referred to as "1", the graph representing the properties of the as-produced W-Cu laminates is referred to as "2", and the graph representing the properties of the recrystallised W-AgCu laminates is referred to as "3".

34

Prior to the tests, we expected the following distribution of the curves. Curve "1" represents the case where the deformation mechanisms associated with the ultrafine-grained microstructure (i.e. ordered glide of screw dislocations) are dominant. Curve "3" represents the case where deformation mechanisms associated with coarse-grained thin foils (i.e. dislocation annihilation or respectively dislocation absorption/transmission at the bcc-fcc interface) are dominant. We had the expectation that through annealing the Charpy impact properties severely deteriorate, as the deformation mechanisms associated with the ultrafine-grained microstructure are no longer present, and the deformation mechanisms associated with coarse-grained thin foils do not yet exist in their full extent.

However, the results plotted in Fig. 19 yield a different picture: with increasing annealing time the Charpy impact properties gradually worsen, and the BDT temperature gradually increases. This result allows for a declaration of a best case limit (curve "1") and a worst case limit (curve "3"). The definition of curve "3" as the worst case limit seems to be reasonable and rational, as the coarse-grained microstructure of the tungsten sheets (1 h at 1800°C (2073 K)) cannot become any further coarse-grained by further annealing. This finally gives the result that the Charpy impact properties of the annealed W-Cu laminates lie in between the limits bounded by curve "1" and curve "3".

By comparing the results of the Charpy impact properties of the as-produced W-AgCu laminates (curve "1") to those of the as-produced W-Cu laminates (curve "2"), further interesting insight of the deformation mechanisms can be derived. W-AgCu and W-Cu laminated composites have both in common that their tungsten-interlayer interfaces are sharp. Both are model systems comprised of mutually insoluble materials. Furthermore, they have in common that the contribution of the interlayer (AgCu or Cu) to the total amount of the dissipated energy can be neglected. Therefore, their main distinguishing characteristic is the state of the microstructure of the tungsten sheets. In the case of the W-AgCu laminate, the joining technology was brazing and the joining-process-caused heat treatment experienced by the tungsten plies was 1 min at 800°C (1073 K). In the case of the W-Cu laminate, the joining technology was diffusion bonding, and the joining-process-caused heat treatment experienced by the tungsten plies was 1 h at 900°C (1173 K).

This result shows that during a heat treatment of 1 h at 900°C (1173 K) the as-rolled lattice defect arrangements change, which severely impacts on the mechanical properties of the tungsten sheets and thus the laminates. This is a further hint of the temperature sensitivity of a cold-rolled, ultrafine-grained microstructure and shows the necessity of developing a microstructure stabilised tungsten material.

In other words, curve "1" represents a laminate made of tungsten sheets in their as-received condition, while curve "2" represents a laminate in an early state of recovery/recrystallisation. Therefore, the differences between the Charpy impact properties of the as-produced W-AgCu laminate (curve "1") and the as-produced W-Cu laminate (curve "2") can be traced back to the recovery/recrystallisation processes.
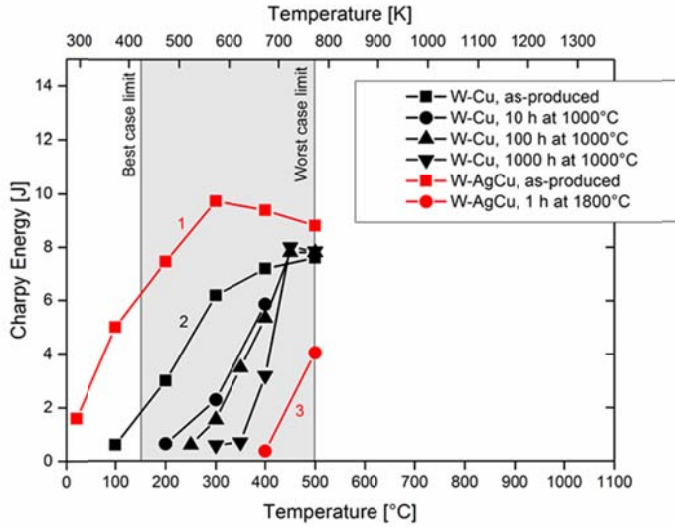
35

Fig. 19. Evolution of the Charpy impact properties through thermal ageing. With increasing annealing time the BDT temperature gradually increases.

Finally, Fig. 19 allows for determining the BDT temperatures. The value of the BDT temperature is determined from the Charpy curves as the temperature corresponding to half the value of the upper shelf energy. The BDT temperatures are summarised in Table 6.

Table 6
BDT temperatures determined from Charpy impact tests.

	W-AgCu, as produced	W-Cu, as produced	W-Cu, 10 h at 1000°C (1273 K)	W-Cu, 100 h at 1000°C (1273 K)	W-Cu, 1000 h at 1000°C (1273 K)	W-AgCu, 1 h at 1800°C (2073 K)
BDT temperature	100°C (373 K)	220°C (493 K)	330°C (603 K)	350°C (623 K)	400°C (673 K)	500°C (773 K)

By comparing of the evolution of the hardness of the tungsten sheets of the W-Cu laminates and the evolution of the BDT temperature of the laminates, a linear relation between the hardness (HV0.1) and the BDT temperature can be anticipated (this anticipation is confirmed by Fig. 12 in Ref. [31] where the BDT temperature of 100 μm-thick tungsten foils is plotted against the annealing temperature). By plotting the BDT temperature against the hardness (HV0.1), a linear relation of the form

$$T_{BDT}(HV0.1) = 1539\,K - 1.9 * HV0.1 \tag{5}$$

where T_{BDT} is the BDT temperature, can be derived. This result of a linear relation between the BDT temperature and the hardness is of a preliminary nature and has to be confirmed by further systematic tests. However it comes as no surprise, as both the relation between the BDT temperature and the grain size [49], and the relation between the hardness and the grain size can be expressed by a Hall-Petch relation [32].

Finally, Figs. 20A and B show the evolution of the contribution of the two deformation mechanisms discussed so far: (i) deformation mechanisms associated with the ultrafine-grained microstructure (i.e. ordered glide of screw dislocations), and (ii) deformation mechanisms associated with coarse-grained thin foils (i.e. dislocation annihilation or respectively dislocation absorption/transmission at the bcc-fcc interface).

In Fig. 20A we make use of the following relations: the hardness of the tungsten plies of a W-Cu laminate in the as-produced conditions relates to a heat treatment of 1 h at 900°C (1173 K), the hardness of the tungsten plies of a W-Cu laminate annealed for 10 h at 1000°C (1273 K) relates to a heat treatment of 1 h at 1060°C (1333 K), the hardness of the tungsten plies of a W-Cu laminate annealed for 100 h at 1000°C (1273 K) relates to a heat treatment of 1 h at 1200°C (1473 K), and the hardness of the tungsten plies of a W-Cu laminate annealed for 1000 h at 1000°C (1273 K) relates to a heat treatment of 1 h at 1350°C (1623 K) (see Ref. [31]).

In the regime of recovery i.e. the regime where no migration of HAGBs takes place, the contribution of the deformation mechanisms associated with the ultrafine-grained microstructure may slightly decrease. However this is just an assumption as the contribution of the as-rolled lattice defects on the mechanical properties are not yet understood to its full extend.

Furthermore, the contribution of the dislocation absorption/transmission at the bcc-fcc interface gradually increases with increasing grain size. The grain size increases by the movement of high angle grain boundaries. As the movement of the high angle grain boundaries starts when the recovery processes are advanced, the red curve in Fig. 20 B is horizontal in the recovery regime and then gradually increases with increasing annealing temperature/time, until a saturation position is reached, at which a single grains covers the entire thickness of the foil and that in turn impedes further grain growth in the S-direction.
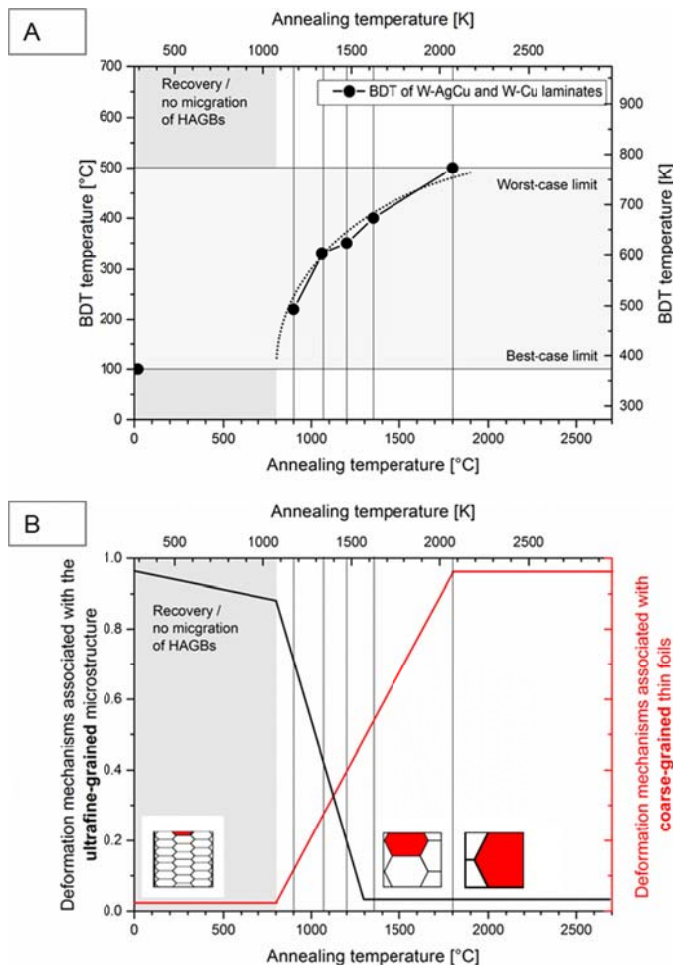

Fig. 20. A: Evolution of the BDT temperature of W-Cu and W-AgCu laminates. A similar results was found for monolithic tungsten (see Fig. 12 in Ref. [31]. B: Evolution of the contribution of selected deformation mechanisms on the Charpy impact properties.

In this section we presented and discussed the evolution of the Charpy impact properties of W-Cu laminates. In the next section, we will show how an activation energy of the annealing kinetics can be derived from Fig. 16.

4.2.1.3. Quantification of annealing kinetics of the tungsten foils: activation energy

The previous sections demonstrated that the tungsten-copper interface stays sharp even after annealing for 1000 h at 1000°C (1273 K). Therefore, the assumption that there is no lattice diffusion and even no considerable grain boundary diffusion of tungsten in copper and vice versa seems reasonable. In the case that the tungsten foils are not affected by any diffusion interaction with copper, they can be regarded as individual foils and their recrystallisation kinetics can be derived from the evolution of the hardness (Fig. 16).
In particular, the activation energy for half recrystallisation, $Q_{X=0.5}$, and the apparent activation energy for half of the total hardness loss, $Q_{\Delta HV/2}$, are important to describe the annealing kinetics, and are an indirect measure of the recrystallisation mechanisms.
Using the Johnson–Mehl–Avrami–Kolmogorov (JMAK) plots, it is possible to calculate the time where 50 % of the volume is recrystallised, $t_{0.5}$. By plotting $ln(t_{0.5})$ against $1/T$, the slope of the fitted line is the activation energy for half recrystallisation, $Q_{X=0.5}$.
A further approach to quantify the annealing kinetics is obtained by the time when half of the hardness loss has occurred [50]

$$\Delta HV/2 = (HV_{as-rolled} + HV_{rxx})/2. \tag{6}$$

In Eq. (6) HV_{rxx} is the hardness of the fully recrystallised state. For the tungsten foils assessed here, the hardness in the as-rolled condition, $HV_{as-rolled}$, is unknown. So instead we used the hardness of the as-received condition which gave a value of $HV_{as-received}$ = 600 HV0.1. Note that due to this modification our calculated activation energy may be overestimated. In the fully recrystallised state, the hardness reaches a value of HV_{rxx} = 400 HV0.1 [31]. The dependence of the time of half of the hardness loss, $t_{\Delta HV/2}$, on the annealing temperature closely follows an Arrhenius relation

$$t_{\Delta HV/2} = t^*_{\Delta HV/2} * \exp\left\{\frac{Q_{\Delta HV/2}}{RT}\right\} \tag{7}$$

with a prefactor, $t^*_{\Delta HV/2}$, the universal gas constant, R = 8.3144598 J/(mol*K), and an apparent activation energy for half of the total hardness loss, $Q_{\Delta HV/2}$. For an annealing temperature of 1000°C (1273 K) the time of half of the hardness loss is 200 h (Fig. 16), and for an annealing time of 1250°C (1523 K) it is 1 h (Fig. 10 in Ref. [31]). By making use of these data and Eq. (7) an apparent activation energy for half recrystallisation of 341.6 kJ/mol (or 3.54 eV) can be derived.
The obtained activation energy for half recrystallisation allows extrapolation of the recrystallisation kinetics to lower temperatures. Accordingly, at 900°C (1173 K) and 800°C (1073 K), half recrystallisation would not be achieved before 0.36 years or 9.3 years respectively. These values are much lower than those obtained from hot-rolled plates, as discussed in Ref. [50], demonstrating clearly the accelerating effect of the stored energy on the recrystallisation kinetics of severely cold-rolled tungsten foils.

Table 7
Comparison of (apparent) activation energies: recrystallisation, grain growth after recrystallisation, bulk self-diffusion and grain boundary diffusion.

Type of activation energy	Value in [kJ/mol] ([eV])	Material	Reference

Half recrystallisation	579 (6.01)	Hot-rolled W plate, 67 % thickness reduction	Alfonso et al. [51]
Half recrystallisation	352 (3.65)	Hot-rolled W plate, 90 % thickness reduction	Alfonso et al. [50]
Half of the hardness loss	341.6 (3.55)	Severely cold-rolled W foils	*This study*
Grain growth after recrystallisation	396 (4.1)	hot-rolled W plate, 75 % thickness reduction	Yuan et al. [52]
Bulk self-diffusion	502 – 628 (5.21 – 6.52)	W	Lassner and Schubert [4]
Grain boundary diffusion	377 – 460 (3.91 – 4.77)	W	Lassner and Schubert [4]

Table 7 gives a comparison of several activation energies for recrystallisation obtained from different tungsten plates. It can be found that the activation energy decreases with increasing degree of deformation.

The activation energy for half recrystallisation of a hot-rolled tungsten plate with a thickness reduction of 67 % is in the range of bulk self-diffusion in tungsten [51]. However, the activation energies for half recrystallisation of a hot-rolled tungsten plate with a thickness reduction of 90 % [50] and the activation energy for half of the total hardness loss of a severely cold-rolled foil are in the range of grain boundary diffusion in tungsten.

In this section, we have analysed the Charpy impact properties of W-Cu laminates. In the next section, the focus will be on their tensile properties.

4.2.2. Tensile properties of W-Cu laminates

The aim of this section is to present and discuss the tensile behaviour of W-Cu laminated composites.

The material was built of three layers of 100 μm-thick tungsten foil (as-received condition) and two layers of 100 μm-thick copper foil, brazed together into a laminate with a total thickness of 0.5 mm and thus the laminate consisted of 60 vol % W. From this laminate, tensile test specimens were cut by spark erosion. The samples were aligned in such a way that the tensile loading direction was congruent with the rolling direction of the tungsten foils (L-direction, 11-direction).

This section is organised as follows: first, the four stages of deformation associated with W-Cu laminates are briefly described. This is followed by a comparison of the tensile properties of tungsten foils and W-Cu laminated composites. Finally the role of the copper interlayer on the unique tensile properties of W-Cu laminates is discussed.

4.2.2.1. Four stages of deformation

Studies on the tensile behaviour of W-Cu and W-CuCrZr (CuCrZr: 0.5 – 1.2 wt % Cr, 0.03 – 0.3 wt % Zr, Cu balance) laminates have been reported by Hoffmann and Weeton [22] and Hohe et al. [24].

Hoffmann and Weeton performed tensile tests on W-Cu laminates and gave consideration to the laminate failure modes and the experimentally determined stress-strain relations, to obtain an indication of the deformation behaviour. Four stages of deformation were observed:

- Stage 1: Elastic deformation of W, elastic deformation of Cu
- Stage 2: Elastic deformation of W, plastic deformation of Cu
- Stage 3: Plastic deformation of W, plastic deformation of Cu
- Stage 4: Fracturing of W and Cu

In particular, fracturing of the tungsten sheets was indicated by a serrated load-strain curve [22].

With the help of Mohr's circle of stress and a finite element stress analyses, the manifestation of the different stages of deformation can be explained as follows:

Let us consider the material synthesis first. The W-Cu laminates are produced by brazing at 1084°C (1357 K). The melting temperature of copper is regarded as the stress-free temperature; thus, the temperature at which the laminated composite is free from any residual stresses is high. During cooling from 1084°C (1357 K) to room temperature, residual stresses establish and gradually increase with decreasing temperature. This can be justified by considering the mismatch of the coefficients of thermal expansion of the tungsten (4.5 ppm/K, 20–100°C (293–373 K)) and the copper phase (17.0 ppm/K, 20–100°C (293–373 K)). The residual stresses that are established during cooling are of compression type in the tungsten phase and of tension type in the copper phase.

Fig. 21 shows the Mohr's circle of stress, in which the stress configuration of both the tungsten phase and the copper phase of a W-Cu laminate in the as-produced configuration can be seen (black dots).
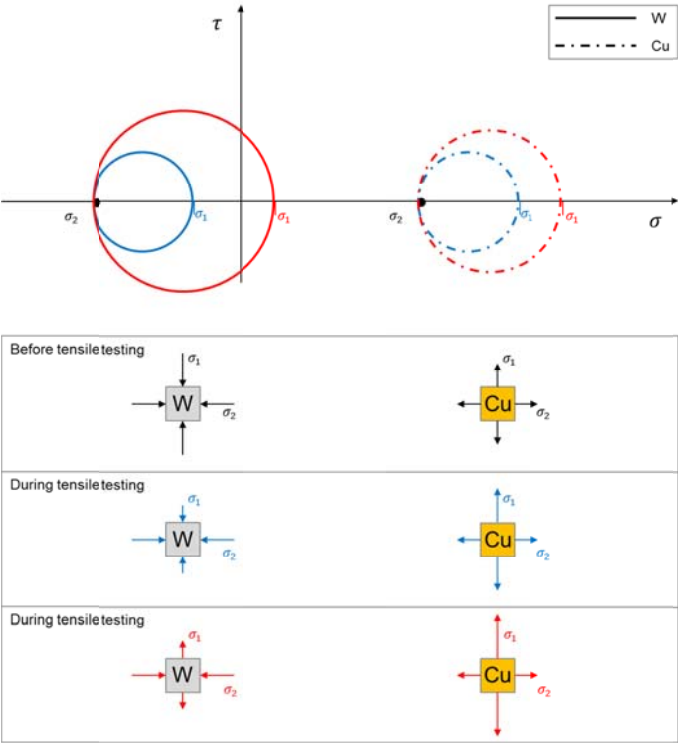

Fig. 21. Mohr's circle of stress of the tungsten phase (solid lines) and the copper phase (dotdashed lines). The stress configuration before tensile testing is marked by the black dots. With increasing tensile stress the blue and finally the red stress configuration is established.

Let us now consider the stress evolution during tensile testing. The tensile tests start in the stage 1 configuration in which both the tungsten phase and the copper phase are in the elastic regime. During tensile testing the deviatoric stresses increase. Note that for standard J_2-plasticity only the deviatoric stresses enter the yield function and thus cause plastic deformation, whereas the hydrostatic stresses result in an entirely elastic deformation.

Next, the laminate enters in its stage 2 configuration and continues with a partially elastic (W) and partially plastic (Cu) deformation. This is continued up to the point where the stresses in the tungsten phase also cause yielding. Now both phases, tungsten and copper, are in their plastic regime. This configuration is referred to as stage 3 (Fig. 22). It can be anticipated from Fig. 21 that the tungsten phase reaches its yield criterion (deviatoric stresses) at a very low σ_1 stress value. This is realised by the compression mode of the σ_2 stress. So for the tungsten phase, a compression stress perpendicular to the tension stress direction can be regarded as ideal state.

The situation looks different for the copper phase. The copper phase has tensile stress components both in the 1- and in the 2-direction. This stress configuration makes the copper phase very sensitive to void formation and increases the risk of brittle failure.

Finally stage 3 is bounded by the fracturing of the laminate, which is referred to as stage 4.

Hohe et al. calculated the tensile behaviour of W-CuCrZr laminated composites by means of an energy-based homogenisation procedure in conjunction with a finite element analysis of a representative volume element. The result of a W-CuCrZr laminate with 60 vol % W can be found in Fig. 22, where ranges of stage 2 (elastic deformation of W, plastic deformation of Cu) and stage 3 (plastic deformation of W, plastic deformation of Cu) are indicated by arrows.
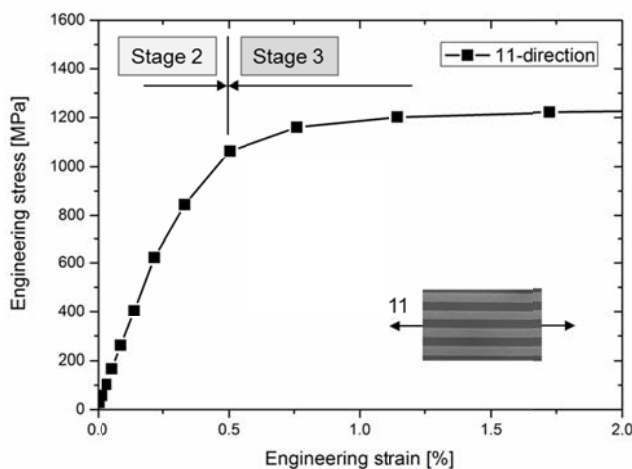

Fig. 22. Effective engineering stress-strain curve of a W-CuCrZr laminated composite with 60 vol % W tested at 200°C (473 K) under uniaxial loading conditions. The results are derived from a numerical exploration by means of an energy-based homogenisation procedure in conjunction with a finite element analysis of a representative volume element [24].

In the next section, we will show the tensile properties of W-Cu laminates. The results are discussed against the background of the four stages of deformation that were introduced here.

4.2.2.2. Comparison of room-temperature tensile properties of tungsten foils and W-Cu laminated composites

In this section, we compare the room-temperature tensile properties of three types of microstructures. These are: (i) 100 μm-thick tungsten foils in their as-received condition, (ii) W-Cu laminates in their as-produced condition, and (iii) W-Cu laminates in their annealed

condition (1 h at 900°C (1173 K) in vacuum). The motivation for the annealing of the laminates was to produce a tungsten phase that represents a microstructure in an early state of recovery/recrystallisation and which is at least somehow similar to the microstructure of the tungsten sheets of the diffusion bonded W-Cu laminates used for the Charpy impact tests in the previous section. Furthermore, the tensile properties of W-Cu laminated composites tested at 300°C (573 K), 400°C (673 K), 500°C (773 K), and 650°C (923 K) are displayed (Fig. 23B).

The room-temperature tensile properties of tungsten foils and of W-Cu laminated composites in their as-produced condition were reported in Refs. [34] and [53]. The tensile testing of the annealed W-Cu laminates is first reported here. The tests were performed in displacement controlled mode at an extension rate of 0.1 mm/min. Longitudinal strain was measured using strain gauges that were positioned directly on the sample.

The tensile properties are displayed in Figs. 23A and B, where the engineering stress is plotted against the engineering strain. The black curve in Fig. 23A represents 100 μm-thick tungsten foils in their as-received condition, tested at room temperature. It is important to see that the tungsten foils show plastic deformation at room temperature. These foils are thus an example of a monolithic tungsten material that exhibits room-temperature ductility.
The room-temperature tensile properties of W-Cu laminates in their as-produced condition are displayed by the red line in Fig. 23A. The ultimate tensile strength is 916 MPa and the total elongation to fracture, A_t, is 15.5 % [53]. This elongation at room temperature is a remarkable result and raises the question of what mechanisms cause this extreme elongation.
Let us first consider the four stages of deformation of W-Cu laminated composites. As shown in Fig. 22, the W-Cu laminate is in its stage 2 condition (the tungsten phase is in the elastic regime and the copper phase is in the plastic regime) shortly after the beginning of the tensile testing. With increasing tensile loading, the stress in the tungsten phase increases, and finally, the tungsten phase also is in its plastic regime. This point refers to the end of stage 2 and the beginning of stage 3. In Fig. 23A, the beginning of stage 3, thus the point from which both the copper phase and the tungsten phase are in their plastic regime, is marked by a red arrow, numbered as "1". This arrow gives the position at which tungsten starts to yield. The question that now arises is why the yielding tungsten phase can reach up to 15 % plastic deformation (elongation to fracture, A). This behaviour is extraordinary and requires further explanation.
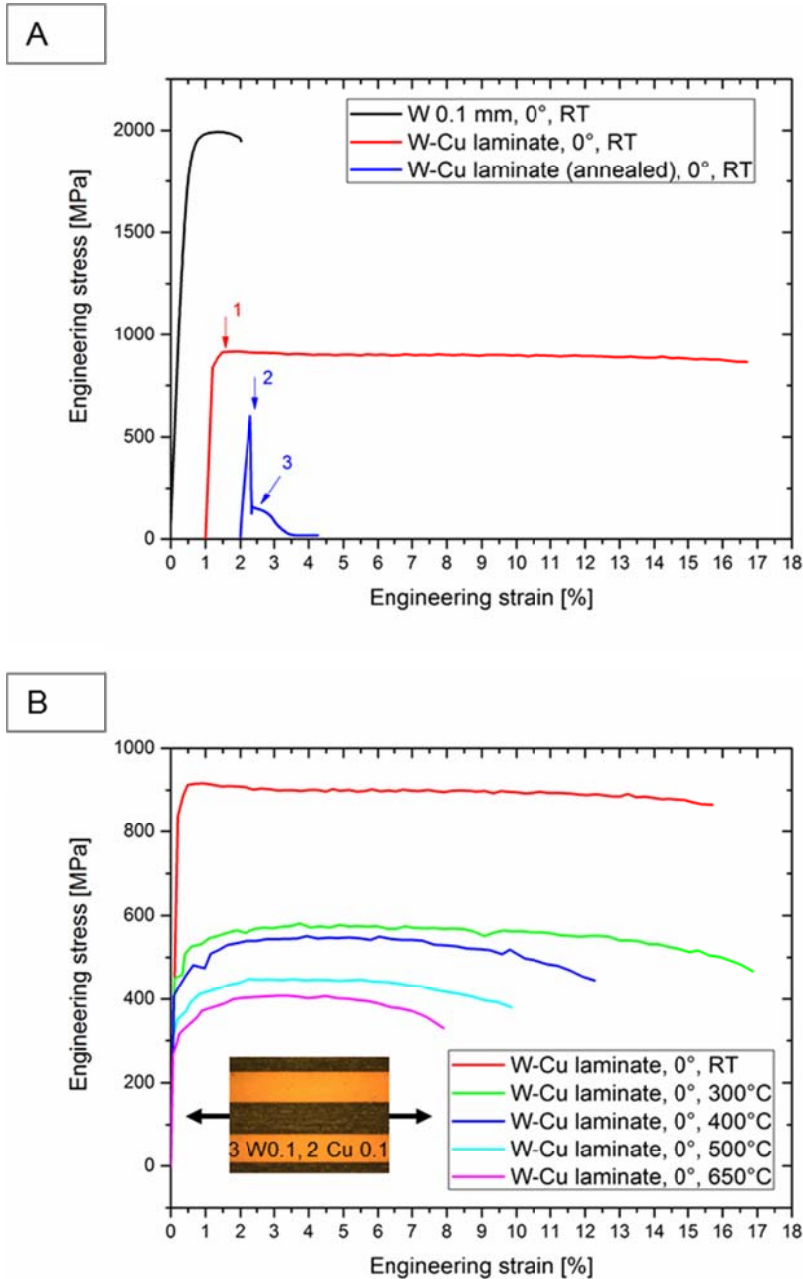
Fig. 23. A: Comparison of the room-temperature tensile properties of (i) tungsten foils, and W-Cu laminated composites in their (ii) as-produced and (iii) annealed (1 h at 900°C (1173 K)) conditions. B: Temperature dependence of the tensile properties of W-Cu laminates. All samples were aligned in such a way that the tensile loading direction matched the rolling direction of the tungsten foils (0°, 11-direction). Data is replotted from Ref. [53].

The room-temperature tensile properties of W-Cu laminates in their annealed condition (1 h at 900°C (1173 K) in vacuum) can help to elucidate the deformation mechanisms in laminated composites. Their tensile properties are shown by the blue curve in Fig. 23A. The blue arrows numbered as "2" and "3" denote important positions of the tensile curve. The microstructural events associated with these positions can be described as follows. Position "2" describes the moment at which the first tungsten ply starts to fracture. The fracturing of the tungsten ply is accompanied by a severe yield drop in the stress-strain curve. At position "3", all tungsten plies are completely broken. Therefore, the yield drop from position "2" to position "3" describes the fracturing of all the three tungsten plies.

43

The copper plies are not affected by the fracturing of the tungsten plies. They stay intact and can bear further loads. The arrow numbered as "3" gives the position at which only the copper plies contribute to the stress-strain curve. The smooth decrease of the stress-strain curve represents the necking of the copper plies. The tensile test was stopped at a total elongation to fracture, A_t, of about 2 %, as no more information could be gained from the curve.

The tensile properties of W-Cu laminates in their annealed condition (1 h at 900°C (1173 K) in vacuum) can help to explain the room-temperature properties (e.g. total elongation to fracture, A_t, of 15.5 %) of W-Cu laminates in their as-produced condition.

It can be clearly seen in Fig. 23A that the fracturing of a tungsten ply is accompanied by a yield drop in the stress-strain curve. We propose the hypothesis that the fracturing of at least one tungsten ply is always accompanied by a yield drop. The general validity of this hypothesis is confirmed by the results of the three-point bending tests, as shown in Fig. 4. In Fig. 4, each yield drop is associated with the fracturing of one tungsten ply.

One may assume that the hardening behaviour of the red curve is caused by multiple cracks in the tungsten sheets, and that the copper phase may be able to sustain the load up to the final failure. However, we do not think that this is a reasonable explanation, as cracking of a tungsten sheet is always accompanied by a yield drop, and in the red curve, no plastic instabilities can be found.

A further important issue is the impact of recovery/recrystallisation. The red curve represents a laminate made of tungsten sheets in their as-received condition, while the blue curve represents a laminate with an advanced recovered/recrystallised tungsten phase. The differences in the tensile properties of the as-produced W-Cu laminate (red curve) and the annealed laminate (blue curve) can therefore be traced back to recovery/recrystallisation processes. This in turn clearly demonstrates that the deformation mechanisms associated with the as-produced laminates strongly depend on as-rolled lattice defect arrangements. Note that the same argument was used when describing the evolution of the Charpy impact properties of W-Cu laminates through annealing (Fig. 19).

Table 8

Comparison of the room-temperature tensile properties of selected tungsten foils and W-Cu laminated composites.

		W-Cu laminates (Hoffmann and Weeton [22])	W-Cu laminates, as-produced condition	W-Cu laminates, annealed condition
W-foil	Thickness	0.127 mm	0.1 mm	0.1 mm
	Condition	4 h at 982°C (1255 K)	As-received	1 h at 900°C (1173 K)
	(Total) elongation to fracture	A approx. zero	A_t = 2 %	-
W-Cu laminate (> 20 vol % W)	(Total) elongation to fracture	A approx. zero	A_t = 15.5 %	A approx. zero

An earlier study on the room-temperature tensile properties of W-Cu laminated composites was performed by Hoffmann and Weeton [22]. It is worth comparing their results with ours, to identify similarities and differences (Table 8).

Hoffmann and Weeton used tungsten foils with a thickness of 0.127 mm. The composites were fabricated by vacuum hot pressing the stack of foils at 982°C (1255 K) for 4 h. Tensile tests at room temperature were performed on tungsten foils that experienced the same heat treatment as the laminated composite (982°C (1255 K) for 4 h). The average tensile strength of the tungsten foil was 1482 MPa, and the specimen exhibited essentially zero elongation to

fracture, A, at room temperature. Furthermore, Hoffmann and Weeton performed tensile tests on W-Cu laminated composites. For composites that had greater than 20 vol % tungsten, they found zero elongation to fracture.

In our study, we used tungsten foils with a thickness of 0.1 mm. In tensile tests at room temperature, the tungsten foil had about 2 % total elongation to fracture, A_t. When joined together with copper foils, the W-Cu laminate (60 vol % W) showed a significant improvement to 15.5 % total elongation to fracture, A_t, at room temperature. However, when the laminate is heat treated for 1 h at 900°C (1173 K), the elongation to fracture, A, is essentially zero.

It is likely, that the tungsten phase of the W-Cu laminated composites fabricated by Hoffmann and Weeton is in an early state of recovery/recrystallisation. This again demonstrates the importance of the as-rolled lattice defect arrangements and shows the necessity of developing a microstructure stabilised tungsten material.

Further insight into the fracture and deformation mechanisms of W-Cu laminated composites can be gained from SEM analyses. Fig. 24 gives a comparison of the manifestation of the fractured surfaces of room-temperature tensile tested (i) 100 μm-thick tungsten foils in their as-received condition, (ii) W-Cu laminates in their as-produced condition, and (iii) W-Cu laminates in their annealed condition (1 h at 900°C (1173 K) in vacuum).

For ease of interpretation of the SEM images, a rough description of the most common fracture mechanisms is given. Intergranular fracture occurs when the grain boundaries are the preferred fracture path in the material. Transgranular (or cleavage) fracture occurs when the fracture path propagates along specific crystallographic planes. Both fracture types, intergranular and transgranular, can either be classified as ductile or brittle.

The fractured surfaces of the tungsten foil and W-Cu laminates look very different and can be characterised as follows.

The fracture type of the single tungsten foil can be described as an intergranular fracture. It has been shown previously that the fracture surface exhibits fine dimples that are typical of a ductile fracture [6]. For these reasons we introduced the term "intergranular fracture with micro-ductile character" to characterise this type of surface.

The fracture surface of the tungsten phase of the tensile tested W-Cu laminate in its as-produced condition looks very different. At low magnification, the fractured surface can be classified as transgranular.

Finally, Fig. 24 displays the manifestation of the fractured surface of annealed W-Cu laminated composites. Again, the tungsten foils show transgranular fracture. In general, the fractured surfaces of the as-produced and annealed laminates are similar. This is a notable result, as the tensile properties of the laminates are very different. However, the difference in the tensile properties does not lead to a change in the fracture type of the fractured surface, at least at low magnification.
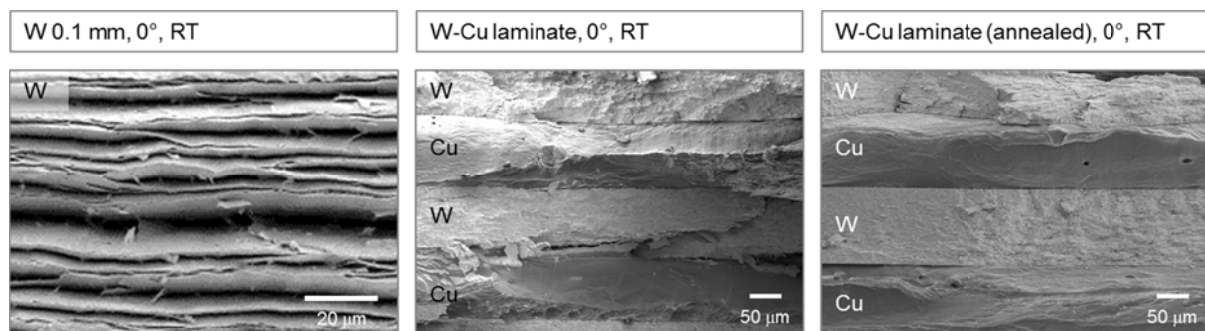

Fig. 24. Comparison of the manifestation of the fractured surfaces of the tensile tested tungsten foils and W-Cu laminated composites. The tensile tests were performed at room temperature.

In this section, we discussed the question of which mechanisms cause the extreme total elongation to fracture, A_t, of 15.5 %. This question can also be addressed in an alternative way: why is the total elongation to fracture, A_t, of a 100 µm-thick tungsten foil only 2 %? Answering the latter question appears to be much easier. It is well known that elongation results are very sensitive to variables, such as specimen geometry, and in particular, the foil thickness. It is also well known that for thin foils under tension, the necking process causes an early onset of plastic instability. With increasing foil thickness, the onset of plastic instability is retarded.

Based on these considerations, one may assume that a tungsten sheet with the same microstructure as the 100 µm-thick tungsten foil, but with a thickness in the range of that of the W-Cu laminate, may also be able to undergo a total elongation to fracture, A_t, of 15.5 % at room temperature. Furthermore, these considerations allow us to make an assumption of the role of the copper interlayer, namely, that it may retard the onset of the plastic instability that is caused by the necking process under tension loading.

However, we think that this is not the only explanation. The reason for this assumption can be seen in Fig. 15B, where the tensile properties of W-AgCu laminated composites are displayed. If the total elongation to fracture, A_t, of 15.5 % at room temperature is only caused by the thickness of the sample, then the total elongation to fracture of W-AgCu laminated composites should be in the same range. However, this is not the case. Thus, the origin of the total elongation to fracture, A_t, of 15.5 % at room temperature may be traced back to other mechanisms.

A further reason may be the ideal state of stress configuration of the tungsten phase. As the tungsten phase is in compression mode for laminates in their as-produced condition (hydrostatic stress), the tungsten phase reaches its yield criterion (deviatoric stresses) at a very low σ_1 stress value (Fig. 21). Due to the different melting temperatures of the interlayer of a W-Cu laminate (melting temperature of Cu is 1084°C (1357 K)) and a W-AgCu laminate (melting temperature of AgCu is 780°C (1053 K)), the residual stresses in the as-brazed conditions are different. From this, it follows that the residual stresses in the tungsten phase of a W-Cu laminated composite are higher than that of a W-AgCu laminate. This impacts the tensile properties in the following way: first, the onset of yielding in a material with high hydrostatic compression stresses is at a lower σ_1 stress value compared to a material that possessed low residual compression stresses, and second, the total elongation to fracture is higher for materials that possess high compression stresses in their as produced condition compared to materials that possessed low residual compression stresses in their as produced condition. The results of the tensile tests of W-AgCu and W-Cu laminates confirm these assumptions (Fig. 15B and Fig. 23B). Additionally, comparing the fracture surface of the tungsten layers in Fig. 15B to the fracture surface in Fig. 24 the different tungsten behaviour of these two composites is obvious.

These considerations also allow us to make an assumption on the role of the copper interlayer and tungsten-copper interface. The copper interlayer causes residual compression stresses in the tungsten phase during cooling down after brazing. These compression stresses are beneficial for the tungsten phase and for its ability to undergo plastic deformation. If delamination in the tungsten-copper interface occurs, then locally the residual stresses in the tungsten phase are severely decreased. It is assumed that the tungsten sheets of the laminate may then behave like individual tungsten foils. Thus, in the case of a delamination event, the total elongation to fracture, A_t, of the W-Cu laminates, may be in the range of the total elongation to fracture of a single tungsten foil.

We finally arrive at the conclusion that the mechanisms for the 15.5% total elongation to fracture, A_t, at room temperature are not yet understood in detail. Nevertheless, we think that we have provided some interesting results that may act as motivation for further systematic tests.

In this section, we discussed the tensile properties of tungsten laminated composites. In the next section the use of laminates in high heat flux components will be discussed.

4.2.3. W-Cu laminates from the technological perspective: caps, pipes, and high heat flux components

The aim of this section is to show and to discuss how W-Cu laminated composites can be used in plasma-facing components, and how they can act as both functional and structural tungsten.

This section is organised as follows: first, we will show how to deep draw caps and how to produce a 1000 mm long W-Cu laminated pipe. Afterwards, we will present the successful fabrication of selected divertor mockups, and discuss their high heat flux performance.

4.2.3.1. Caps and pipes

Fig. 25 displays a cross section of a deep drawn W-Cu laminated cap. The cap was deep drawn from a round disc. The disc was made of six layers of tungsten foil and five layers of a copper alloy, joint together by brazing. Each layer had a thickness of 0.1 mm. The tungsten foil was in its recrystallised condition. The inset on the left-hand side in Fig. 25 shows a photograph of the deep drawn cap and gives an impression of the smooth radii and the surface topology. The inset on the right-hand side in Fig. 25 displays a detailed view of the microstructure. The recrystallised and coarse-grained microstructure of the tungsten foils can be seen.

The deep drawing was performed in a vacuum chamber (operation pressure < 10^{-5} mbar), at 600°C (873 K), and with a cross-head velocity of 0.1 mm/min. For more details on how to deep-draw tungsten the reader is referred to Ref. [54].
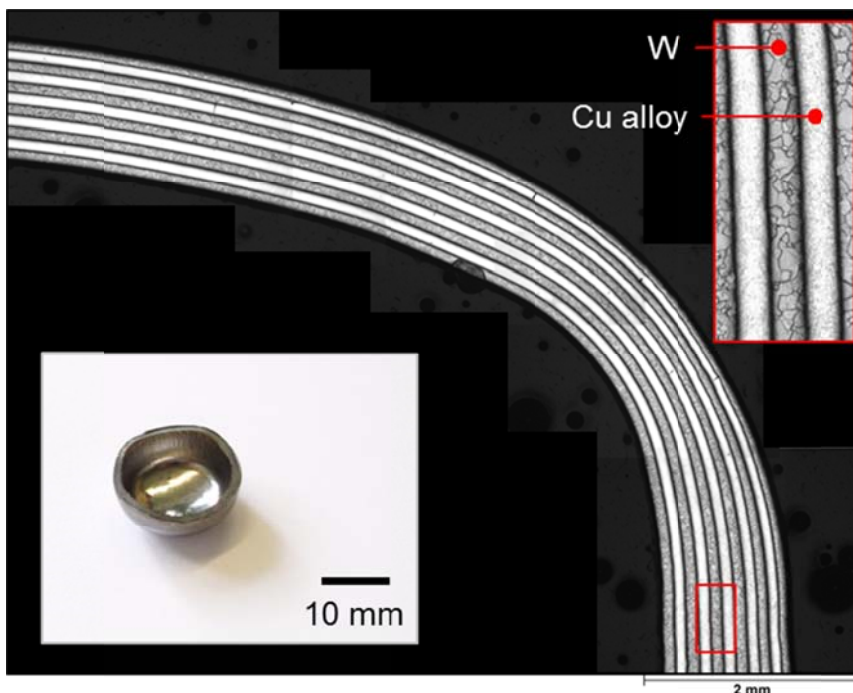

Fig. 25. Optical micrograph of the cross section of a deep drawn W-Cu alloy laminated cap. The W-Cu alloy laminate was in its recrystallised condition. The inset on the left-hand side provides a view inside the deep drawn cap.

Fig. 26A shows several W-Cu laminated pipes: one with a length of 1000 mm, four pipes with a length of 500 mm, as well as three mockups made of W-Cu laminated pipes. The pipes were made by coiling up a tungsten and a copper foil. Each foil had a thickness of 0.1 mm.

The tungsten foil was in its as-received condition. The joining technology was brazing. Each pipe has an outer diameter of 16 mm, a wall thickness of about 0.5 mm and was joined to austenitic steel (1.4571) plugs. The measured helium leak rate of the pipes was tested at room temperature. The helium leak rate is smaller than 1 x 10^{-9} mbar l/s, which is the resolution limit of the helium leak rate test device. Up to now, the mechanical properties of the pipes have been determined by Charpy impact tests (RT – 700°C (973 K)) [17], a burst test at room temperature at PLANSEE SE [55], and high heat flux tests at the Plataforma Solar de Almería, Spain [55].

In this paper we report high heat flux tests that were performed at the Garching large divertor sample test facility (GLADIS), at the Max Planck Institute for Plasma Physics (IPP), Garching, Germany [56, 57].

Fig 26B gives an impression of the high heat flux testing of W-Cu laminated pipes in GLADIS. The aim of the test was to determine the thermal performance of the W-Cu laminated pipes up to the thermal limit of heat transfer to the cooling water. Two pipes with a length of 500 mm (see Fig. 26A) were adapted to the GLADIS facility. The coolant was water with an inlet temperature of 15°C (288 K), a pressure of 10 bar, a velocity of 10 m/s, and a flow rate of 1.55 l/s. No swirl tape was used.

The following exposures were performed:
- 5 pulses at 8 MW/m², 10 s duration,
- 5 pulses at 10 MW/m², 10 s duration,
- 5 pulses at 13 MW/m², 10 s duration,
- 5 pulses at 15 MW/m², 10 s duration,
- 5 pulses at 17 MW/m², 10 s duration,
- 5 pulses at 20 MW/m², 10 s duration,
- 5 pulses at 23 MW/m², 10 s duration,
- 2 pulses at 28 MW/m², 3–3.4 s duration.

The outlet pipe failed at 28 MW/m², due to the expected onset of the boiling crisis, the so-called critical heat flux (CHF). For details on the calculation of the critical heat flux the reader is referred to the work by Tong [58]. A sudden collapse of the heat transfer resulted in an overheating of the outlet pipe.

In detail, the failure of the pipe was as follows: at 3 s heating (second pulse at 28 MW/m²) an overheating of the outlet pipe was detected and the pulse was stopped (3.4 s). Three seconds after the end of the loading, the pipe failed locally due to the inner pressure of 10 bar.

As the W-Cu pipes were directly cooled, the surface temperatures of the pipes were low. Due to the low emissivity of the low-temperature surfaces, no reliable surface temperature data can be provided.
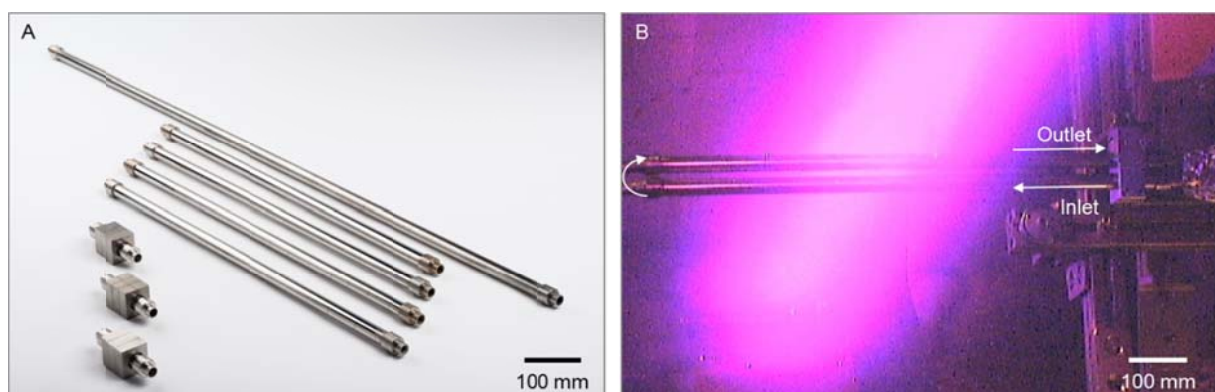

Fig. 26. W-Cu laminated pipes may be used as structural tungsten. A: Pipes with a length of up to 1000 mm can be produced. B: The pipes have been high heat flux tested in GLADIS, at the IPP in Garching, Germany.

In the next sections, we will show how W-Cu laminates can be used for the manufacturing of successful high heat flux components.

4.2.3.2. Fabrication and testing of mockups: W-Cu laminates used as functional tungsten

W-Cu laminated composites allow for tailoring thermo-physical properties, such as (i) the thermal conductivity, k, and (ii) the coefficient of thermal expansion, α, (CTE). This makes W-Cu laminates an interesting functional interlayer material.

Common to all contemporary divertor concepts is an interlayer at the boundary between the tungsten armour and the cooling structure. It has been demonstrated that an effectively designed interlayer can produce dramatic gains in power handling [59].

There are mainly two reasons to use a W-Cu laminate as an interlayer: (i) the coefficient of thermal expansion can be adjusted to lie in-between the limits bounded by the coefficient of thermal expansion of the tungsten armour (4.5 ppm/K, 20–100°C (293–373 K)) and the cooling structure (e.g. CuCrZr: 16.72 ppm/K, 20–100°C (293–373 K)), and (ii) due to the anisotropic thermal conductivity of the laminate (the thermal conductivity in the in-plane direction is higher than in the through-plane direction), the heat load can be more gently distributed in the cooling structure. However, to effectively design the W-Cu interlayer, knowledge about the evolution of the properties with temperature and the change of the properties with volume fraction are essential. This is why we will now re-evaluate the data from two self-contained studies on the thermo-physical properties of laminated composites from Seiss et al. [9] and Hohe et al. [24]. The result obtained and the mechanisms identified by these studies are useful in developing successful plasma-facing components.

Both studies show that the homogenised thermal conductivity both in the in-plane (linear rule of mixture, Eq. (1)) and in the through-plane direction (reciprocal rule of mixture, Eq. (2)) can be determined using the rules of mixture. The determination of the effective thermal conductivity is an entirely linear homogenisation problem, for which the rules of mixture provide rigorous mathematical bounds. However, the determination of the homogenised coefficients of thermal expansion is not a linear homogenisation problem. This is mainly due to two reasons: (i) tungsten has isotropic elastic constants while copper does not, and (ii) the copper phase may be in its plastic regime. This is why the rules of mixture fail to estimate the coefficients of thermal expansion.

Seiss et al. [9] performed several experiments on Mo-Cu multilayer materials that are used as heat spreader material in the field of thermal management for power electronics. They reported a peculiar behaviour of the coefficient of thermal expansion, which can be summarised as follows: (i) the homogenised coefficients of thermal expansion are found outside the region bounded by the rules of mixture (Fig. 27A), (ii) with increasing temperature, the coefficient of thermal expansion first decreases then gently increases (Fig. 28A), and (iii) the coefficient of thermal expansion changes during thermal cyclic loading [12]. The experimental results of Seiss et al. have recently been qualitatively confirmed by a numerical homogenisation analysis by Hohe et al. [24].
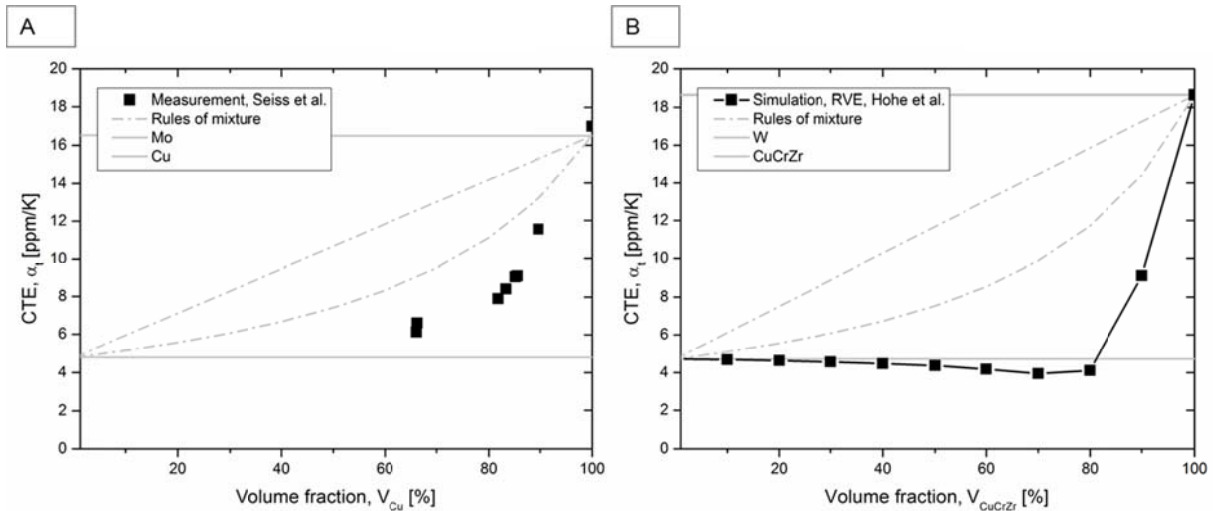
Fig. 27. Effective coefficients of thermal expansion are found outside the region bounded by the rules of mixture. Comparison of experimental data obtained from Mo-Cu multilayer composites (A: CTE in the in-plane direction, RT – 100°C (373 K)) with simulation results of W-CuCrZr laminates (B: CTE in the in-plane direction, RT – 600°C (873 K)). Both diagrams show qualitatively the same trends.

Hohe et al. used the method of representative volume elements (RVE) to determine the effective coefficients of thermal expansion in laminated W-CuCrZr composites. Similar to the results of Seiss et al., they found that the homogenised coefficients of thermal expansion are distinctively outside the region bounded by the rules of mixture (Fig. 27B), and that the coefficient of thermal expansion first decreases with increasing temperature (Fig. 27B). The reason for this effect is not yet understood, and is the topic of current studies. It is likely that the plastic deformation of the Cu-phase plays an important role. By decreasing the thickness of the copper layer, the yield stress in the Cu-phase increases according to the models presented in Section 2.2. "Strength". This offers the possibility of designing multilayer materials that operate solely in the elastic regime.
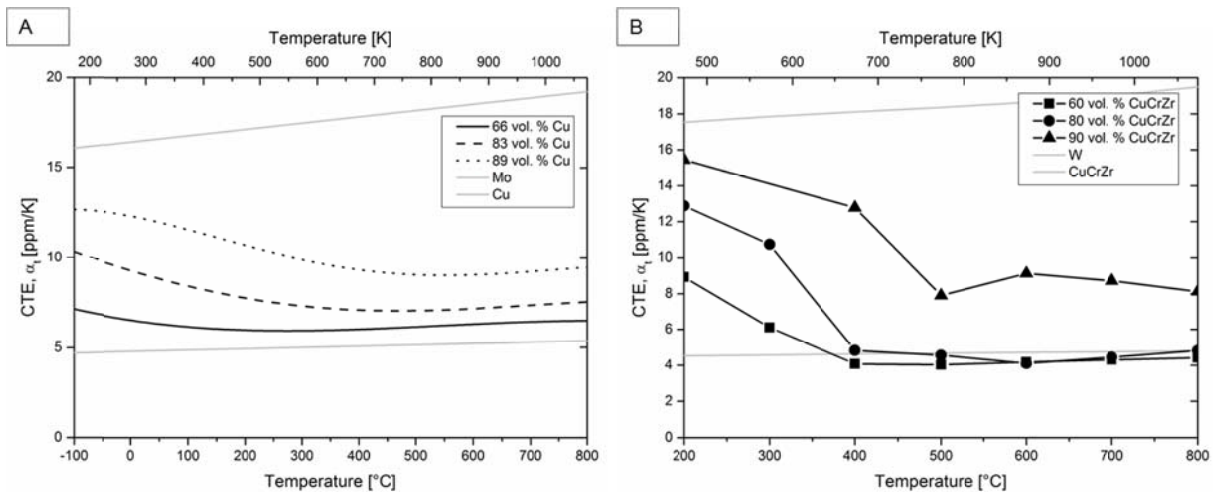

Fig. 28. With increasing temperature, the coefficient of thermal expansion first decreases and then gently increases. Comparison of experimental data obtained from Mo-Cu multilayer composites (A: CTE in the in-plane direction and related to RT) with simulation results of W-CuCrZr laminates (B: CTE in the in-plane direction and related to RT). Both diagrams show qualitatively the same trends.

We make use of these results when designing mockups for e.g. "flat tile", "saddle", or "monoblock" conceptual design studies.

Fig. 29 gives an impression of a so-called "flat tile" mockup. The flat tile concept has been assessed in-depth by Linke [60]. We modified the concept from Linke in the following way: The armour material is a hot-rolled tungsten plate with a thickness of 5 mm. The cooling structure is made of CuCrZr. The interlayer at the boundary between the tungsten armour and the cooling structure is a W-Cu laminated plate. An optical micrograph of the cross section clearly displays the tungsten armour, the W-Cu laminate, and the CuCrZr cooling structure (Fig. 29, Detail A).

The tungsten armour was joined to the CuCrZr cooling structure by diffusion bonding. The joining parameters were: vacuum, 600°C (873 K), 1 h, 35 MPa.

The flat tile concept slightly differs from the well-known monoblock concepts. The idea of the flat tile concept is to use the tungsten armour material only in the hottest regions of the mockup, that is the heat-loaded top surface. The role of the W-Cu laminated interlayer is to act as a heat spreader and to improve the heat load distribution in the cooling structure. Furthermore, the laminate may compensate for the mismatch of the coefficients of thermal expansion of tungsten and CuCrZr. The ongoing and future work on the "flat tile" conceptual design study and the projected high heat flux tests should provide answers to the following main questions: What is the heat removal capability of a flat tile mockup? Will the well-known "macro-crack" (or "main crack" or "deep crack" as it is often referred to) appear in the tungsten armour? Does a castellation produce gains in power handling?
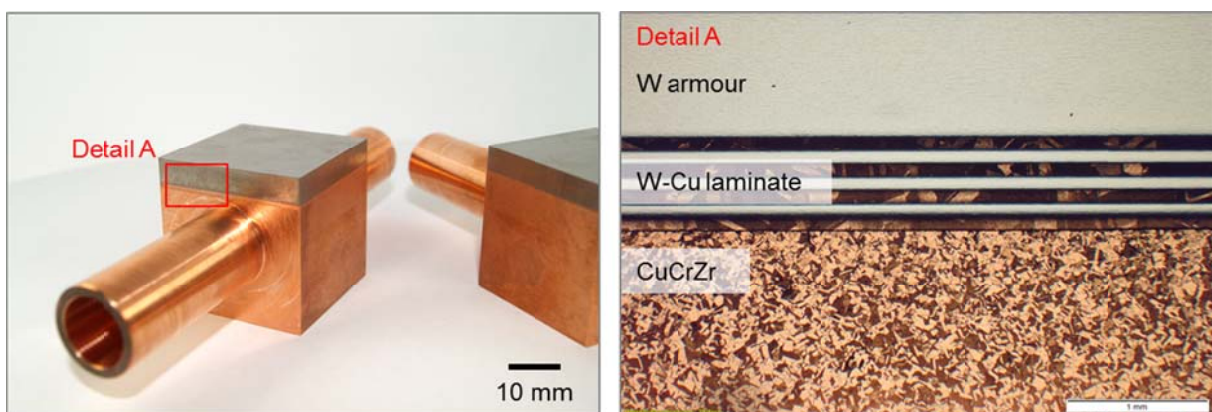

Fig. 29. Mockups of a so-called "flat tile" conceptual design study. A W-Cu laminates plate is used as a functional interlayer material (Detail A).

In a recent publication, we reported the so-called "saddle" conceptual design study [55]. The saddle mockup consisted of tungsten armour with the shape of half a monoblock (saddle), and the cooling structure was a pipe made of austenitic steel (1.4571, 316Ti). The interlayer was a W-Cu laminate. All components were joined by brazing. Such mockups were high heat flux tested in GLADIS. The test parameters for the coolant were: water, RT, 10 bar, 10 m/s, 1.13 l/s, no swirl tape. The mockup was able to withstand a heat load of 5 MW/m^2. At a heat load of 6 MW/m^2 the surface temperature increased significantly and the test was stopped. Post examination revealed that at a heat load of 6 MW/m^2 the copper phase of the W-Cu laminate started to melt.

Finally, Fig. 30 shows an optical micrograph of a cross section of a monoblock-based mockup of our "monoblock" design study.

The mockup is formed from the following components (from inside to outside): a corrosion protection layer (here: 1.4571, planned: 1.4016 (X6Cr17)), a structural pipe (here: Cu, planned: CuCrZr), a region where the structural pipe is reinforced by tungsten foils, and the tungsten armour.

The fabrication of such a mockup consists of several individual steps, such as the copper casting into the tungsten monoblock, the brazing of the laminated pipe, and the hot isostatic pressing of the corrosion protection layer into the structural pipe.
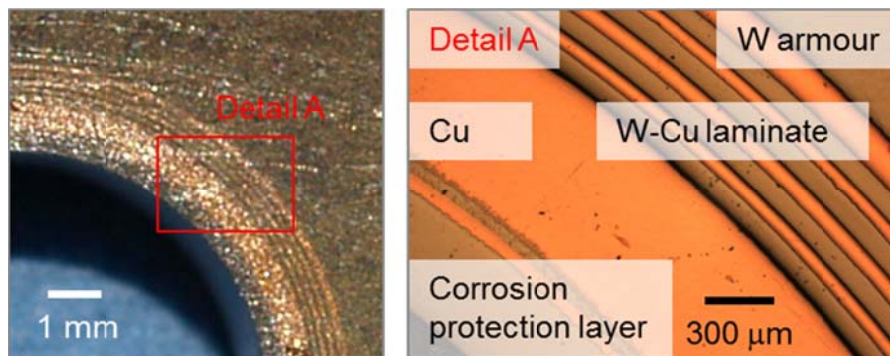

Fig. 30. Cross section of a mockup of our "monoblock" design study. The structural copper-based pipe is reinforced by tungsten foils. The inside surface of the pipe is made of a corrosion protection layer (e.g. 1.4016 (X6Cr17)).

In this section, we discussed the use of W-Cu laminates as a functional interlayer material (heat spreader, CTE mismatch compensator, structural pipe reinforcement). In the next section, the use of tungsten laminates as structural tungsten will be discussed.

4.2.3.3. Fabrication and testing of mockups: W-Cu laminates used as structural tungsten

W-Cu laminated composites possess improved Charpy impact and tensile properties as compared to coarse-grained plate tungsten (Figs. 19 and 23), and may be thus regarded as structural tungsten. In particular, the high-temperature, high-efficiency, helium-cooled divertor concepts demand for advanced structural materials [61-63]. For such concepts, W-Cu laminated composites may perform the function of a pipe for a cooling medium.

Figs. 31A and B show a mockup of a design study on the power handling capacity of a helium-cooled divertor. For details on the basic ideas of this design study the reader is referred to Ref. [64]. The mockup displayed in Fig. 31A consists of the following components: the tungsten armour is monoblocks with the dimensions of 32 mm x 32 mm x 12 mm. The monoblocks were cut from a tungsten rod by milling and turning. The position of the monoblock relative to the axis of the tungsten rod was such that the heat load direction is parallel to the axis of the rod. The plasma-facing surface was finished by grinding. The gaps between the monoblocks were 0.1 mm. The monoblocks were joined to the W-Cu structural cooling pipe by brazing with pure copper. The interlayer between the tungsten armour and the cooling pipe is pure copper with a thickness of 0.1 mm. The cooling pipe is a W-Cu laminate pipe with an outer diameter of 16 mm and a wall thickness of about 0.5 mm. The laminated pipe was produced by brazing of a coiled tungsten foil (0.1 mm, as-received condition) and a copper foil (0.1 mm). In order to easily adapt the mockup to the GLADIS test device, the laminated pipe is joined on both ends to steel plugs (1.4571).

Fig. 31B shows the mockup sliced open, to provide a view of the interior. A steel cartridge made from reduced activation ferritic martensitic (RAFM) steel can be seen. The steel cartridge is designed to perform effective helium cooling, or more precisely, to enable the helium jet impingement that increases the heat transfer coefficient.
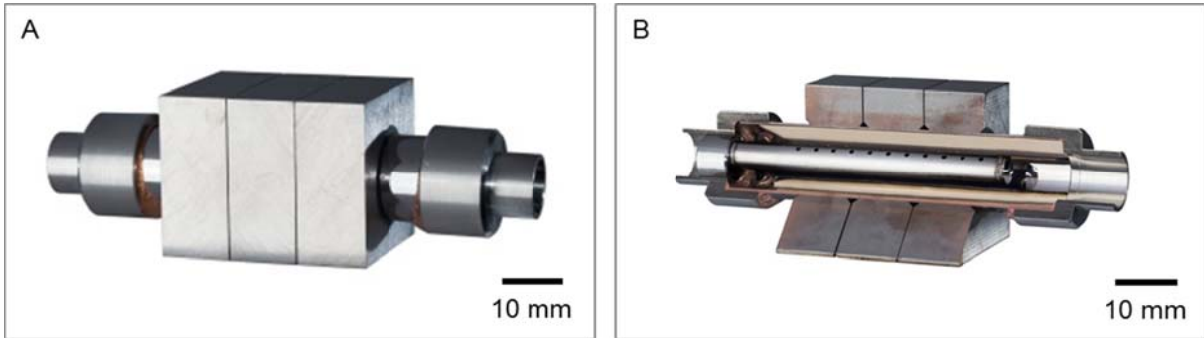
Fig. 31. Mockups of a conceptual design study on the power handling capability of an helium-cooled divertor. The mockups consist of: tungsten armour, W-Cu structural cooling pipe, RAFM steel cartridge. The laminated pipe is joined on both ends to steel plugs (1.4571).

The mockup from Fig. 31A was high heat flux tested in GLADIS. For these tests, the steel cartridge was removed and no swirl tape was used. The coolant was water and the coolant parameters were: RT, 10 bar, 10 m/s, 1.5 l/s. Fig. 32A shows the mockup during high heat flux testing and Fig. 32B displays the temperature distribution in the equilibrium condition at a heat load of 13 MW/m^2.
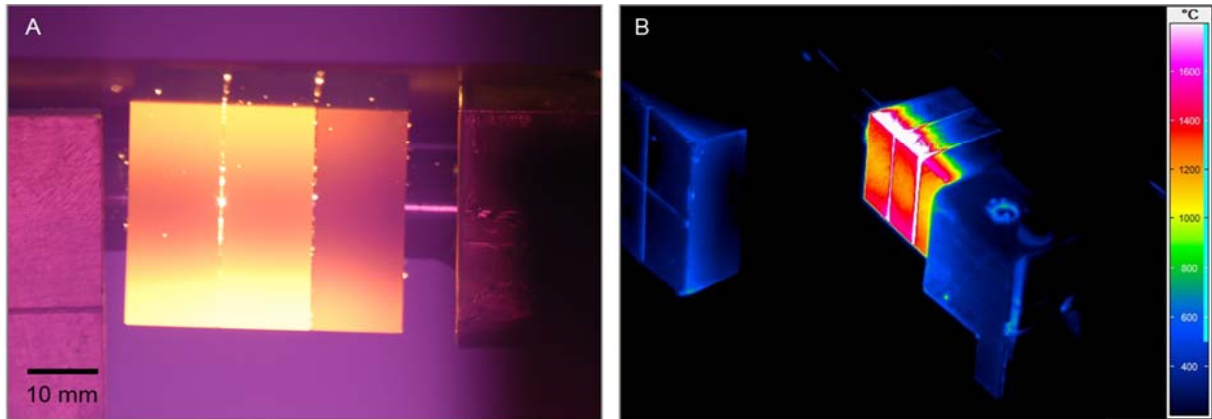

Fig. 32. A: Mockup from Fig. 31A during a high heat flux tested in GLADIS. B: Temperature distribution at the last pulse at 13 MW/m^2.

The following heat loads were applied:
- 3 MW/m^2, 10 s, two pulses,
- 5 MW/m^2, 10 s, two pulses,
- 6 MW/m^2, 10 s, two pulses,
- 3 MW/m^2, 10 s, two pulses,
- 8 MW/m^2, 10 s, two pulses,
- 10 MW/m^2, 10 s, two pulses,
- 13 MW/m^2, 10 s, two pulses.

In Fig. 33, the maximum surface temperature is plotted against the applied heat load. The surface temperature was measured by a two-colour pyrometer. The maximum surface temperature was also determined by a finite element method (FEM) analysis. Fig. 33 gives a comparison of the calculated and the measured maximum surface temperatures.

From the temperature measurement, a linear relation between the maximum surface temperature, $T_{surface}^{max}$, in °C and the applied heat load, $\dot{q}$, in MW/m^2 can be derived:

$$T_{surface}^{max} = 60.4 + 92.6 * \dot{q}. \tag{8}$$

Eq. (8) is a linear fit of the measured temperatures and is plotted in Fig. 33 by a dashed line. This equation allows for extrapolation of the experimentally determined data. According to Eq. (8), a heat load of 20 MW/m^2 would result in a maximum surface temperature of 1912°C (2185 K).
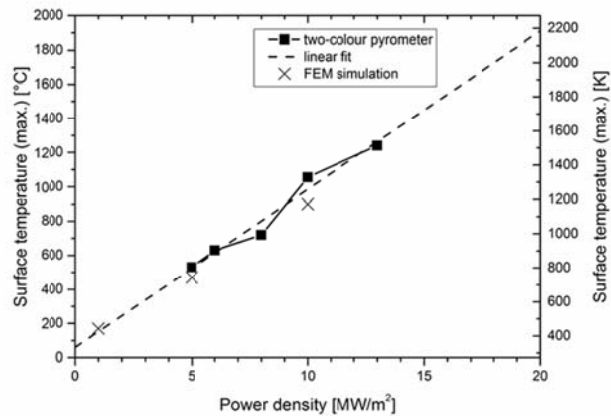

Fig. 33. Maximum surface temperature plotted against the heat load. Only the measured temperatures were used for the linear fit.

Heat flux screening was stopped after the second pulse of 13 MW/m^2 and the mockup was removed from the test device to check its status. During high heat flux testing, no cracks were detected. However, when the mockup was dismounted from the test device, characteristic cracks were visible: all monoblocks were cracked in the centre of the heat loaded surface (Fig. 34). Unfortunately, these cracks were not detectable during heat flux testing, so it is not possible to say at which heat flux the cracks first appeared.
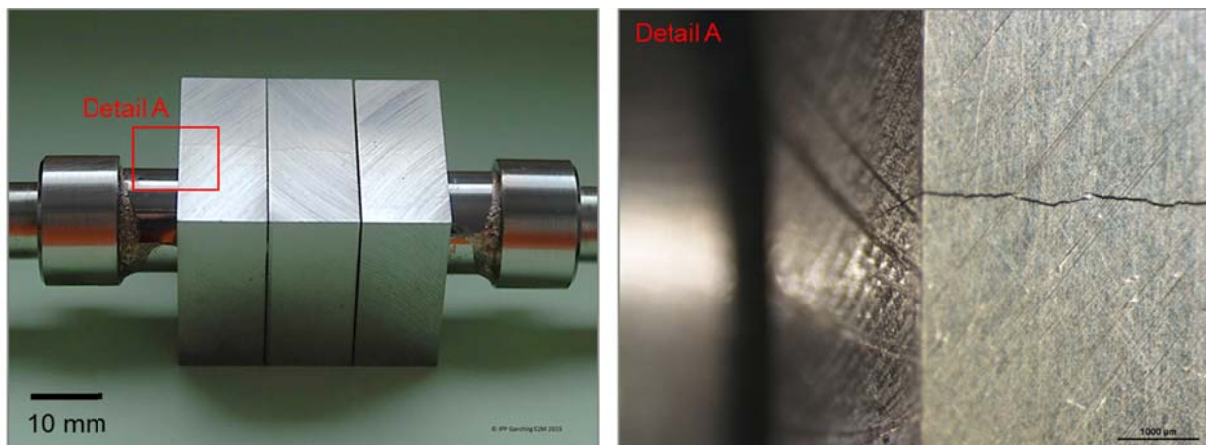

Fig. 34. Mockup after high heat flux testing in GLADIS. All tungsten monoblocks show the well-known damage referred to as "macro-crack".

The type of damage shown in Fig. 34 is well known and is referred to as "macro-crack" (or "main crack" or "deep crack"). The "macro-crack" is defined as follows. The crack plane normal is perpendicular to the axis of the cooling pipe, and perpendicular to the heat load direction. Furthermore, the crack occurs in the centre of the heat loaded surface.

The reason for the occurrence of such a type of damage is not yet understood in detail, and is the topic of current studies. One may argue that the tungsten microstructure may recrystallise in the vicinity of the heat-loaded surface during high heat flux testing, and that

54

the crack initiates during the cooling period, starting from the heat-loaded surface. However, the measured maximum surface temperatures (Fig. 33), as well as the duration of the applied loads, suggest that it is not very likely that recrystallisation in the tungsten armour took place. Another explanation for the origin of the "macro-crack" may consider the different coefficients of thermal expansion of the tungsten armour and the cooling structure. For the cooling pipe, a W-Cu laminate pipe was used. From Fig. 27, it can be seen that the coefficient of thermal expansion in the in-plane direction of a W-Cu laminate with 40 vol % Cu is nearly equal to that of pure tungsten. Therefore, this argument does not seem likely.

A possible way to overcome the issue of "main crack" may be the use of cold-rolled tungsten plates. One may assume that a "macro crack" will not appear when cold-rolled or severely cold-rolled tungsten plates are used for the monoblocks, as it has been demonstrated that cold-rolled plates possess a high crack growth resistance that increases with increasing degree of deformation [6].

A summary of selected high heat flux test campaigns is given in Table 9. To put the applied heat loads into perspective, some benchmark heat loads are given: sun on a beach: 0.001 MW/m^2; space shuttle re-entry: 0.1 MW/m^2; rocket nozzle throat: 5 MW/m^2; and high power electronic devices: 5–50 MW/m^2 [65].

Table 9
Summary of the results of selected high heat flux test campaigns. All mockups were made of W-Cu laminated composites. The laminates were either used as functional or structural tungsten.

Mockup name	Heat load in [MW/m^2]	Component: Armour material / interlayer / structural part	W-Cu laminate used as:	Coolant	HHF test device	Result	Reference
Saddle mockup	6	W / W-Cu laminate / austenitic steel (1.4571, 316Ti)	Functional interlayer material	Water, RT, 10 bar, 10 m/s, 1.13 l/s	GLADIS, IPP, Germany	Cu phase started melting	Reiser et al. [55]
W-Cu /Mo-Cu laminated pipe	4.5	Tests on the bare pipe	Structural part	Water, RT, 1.26 bar, 9 l/min	Solar furnace, PSA, Spain	Loss of the black surface coating	Reiser et al. [55]
W-Cu laminated pipe	28	Tests on the bare pipe	Structural part	Water, RT, 10 bar, 10 m/s, 1.55 l/s	GLADIS, IPP, Germany	Onset of boiling crisis	*This study*
Monoblock mockup	13	W / Cu / W-Cu laminate	Structural part	Water, RT, 10 bar, 10 m/s, 1.5 l/s	GLADIS, IPP, Germany	"macro-crack" in W armour	*This study*

Up to this point, only model systems comprised of mutually insoluble materials have been investigated. In the next section, laminates that show reactivity between tungsten and the interlayer will be analysed.

4.3. W-V and W-Pd laminates: On the performance of tungsten laminates with a high melting point interlayer

The aim of this section is to elucidate diffusion mechanisms in tungsten-vanadium and tungsten-palladium laminated composites and to correlate the evolution of the Charpy impact properties with the evolution of the microstructure.

Fig. 35 provides an overview of the evolution of the microstructure of W-Cu, W-V, W-Pd and W-Ti laminated composites. W-Cu laminates have been discussed earlier in this paper and the diffusion mechanisms and mechanical properties of W-Ti laminated composites have been reported in Ref. [27] (see Fig. 36). In this section we will focus on W-V and W-Pd laminates only.

Fig. 35. Overview of the evolution of the microstructure of selected tungsten laminated composites. The optical micrographs display the microstructure in the as-polished condition. However, the sample of the W-Cu laminate in the as-produced condition has been Cu-etched. From the Cu-etched microstructure it can be inferred that the Cu grains are very big and that the Cu plies have a nearly single-crystal character.
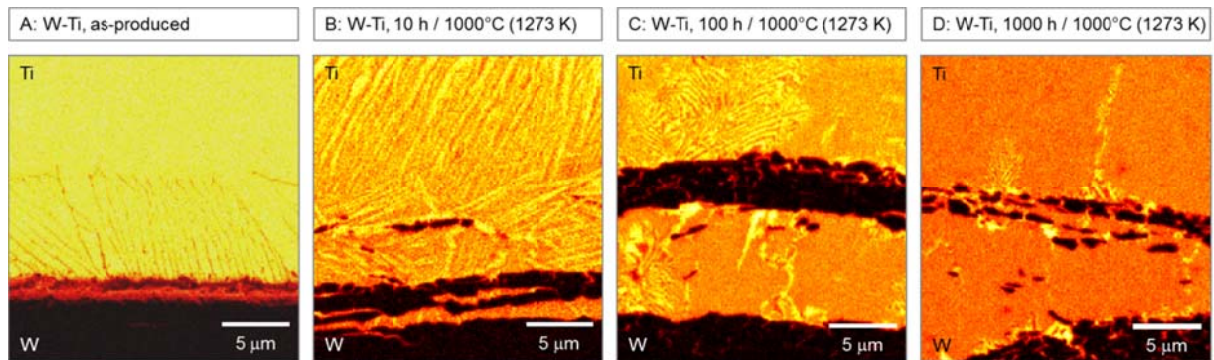
Fig. 36. AES analyses of the tungsten-titanium interface after annealing. Details can be found in Ref. [27].

The W-V laminates consisted of 20 layers of tungsten foil (0.1 mm) and 19 layers of vanadium foil (0.1 mm), while the W-Pd laminate was built up of 27 layers of tungsten foil (0.1 mm) and 26 layers of palladium foil (0.05 mm). The laminates were produced by diffusion bonding at 900°C (1173 K) for 1 h in vacuum. Charpy impact test samples were cut by spark erosion. The samples are of KLST type and represent the L-S crack system. Four conditions are considered: (i) as-produced, and annealed at 1000°C (1273 K) for (ii) 10 h, (iii) 100 h, and (iv) 1000 h.

The following sections will address the questions:

- What are the diffusion mechanisms in W-V and W-Pd laminated composites?
- How can AES analyses as well as thermodynamic and kinetic considerations contribute to an in-depth understanding of the evolution of the tungsten-interlayer interface?
- How do the Charpy impact properties of W-V and W-Pd laminates change through annealing for 10, 100 and 1000 h at 1000°C (1273 K))?

This section is organised as follows: first the diffusion mechanisms in W-V laminated composites are described. This comprises the simulation of diffusion as well as SEM and AES analyses of the tungsten-vanadium interface. Afterwards, diffusion mechanisms in W-Pd laminated composites are investigated. Finally, the Charpy impact properties are presented and discussed against the background of the evolution of the microstructure.

4.3.1. Diffusion mechanisms in W-V laminated composites

The diffusion mechanisms in W-V laminated composites are elucidated by evaluation of both the thermodynamic and diffusional properties of the V-W system and in-depth microstructural investigations by means of SEM and AES analyses. The laminates were produced by diffusion bonding at 900°C (1173 K) for 1 h in vacuum. Afterwards, the laminates were annealed for 10, 100 and 1000 h at 1000°C (1273 K).

4.3.1.1. Thermodynamic and diffusional properties of the V-W system

Tungsten and vanadium both crystallize in the body-centred cubic structure (bcc) and they form continuous solid solutions at higher temperatures. The thermodynamic dataset of V-W selected for the present work has been optimized by Bratberg [66]. Since no thermodynamic data for this system are available, this evaluation is based only on phase diagram data involving equilibria with the melt. At temperatures below 800°C, this dataset predicts a

miscibility gap in the alloys which has not been confirmed experimentally. However, the investigations of the present work are concerned only with higher temperatures.

The process of diffusion bonding and ageing is simulated with the software package DICTRA [67]. This program can handle interdiffusion processes in multi-component systems with strongly varying diffusion coefficients. In the program, the interdiffusion coefficients are calculated from the mobilities of the diffusing species and the thermodynamic factors which are available via the thermodynamic dataset [67]. Prior to the kinetic simulation, the mobilities of the components had to be evaluated from experimental data on the self-diffusion and impurity-diffusion coefficients, respectively. The self-diffusion coefficients for tungsten and vanadium have been taken from the compilation in the Landolt–Börnstein Handbook [68]. The impurity diffusion coefficient of vanadium in tungsten has been measured by Klotsman et al. [69]. Unfortunately, the impurity diffusion coefficient of tungsten in vanadium has not yet been reported in the literature. However, we estimated this value based on the interdiffusion profiles obtained in our present experiments. More details are given below in the discussion of the calculated diffusion profiles. In addition, the concentration dependence of the tracer diffusion coefficient of ^{48}V in V-rich alloys has been reported by Pelleg and Segel [70]. According to this investigation, the tracer diffusion coefficient D_V^* is independent of the concentration within the investigated range, 0-7 at.% W in vanadium. Here, we assume a similar behaviour for the tracer diffusion coefficient D_W^*. Based on this information, the diffusion coefficients have been calculated as a function of the composition at 1000°C. In Fig. 37 the results are shown for the tracer diffusion coefficients, D_V^* and D_W^* as well as for the

interdiffusion coefficient $\tilde{D}$. The diagram reveals that the values of the diffusion coefficients are decreased by ten orders of magnitude when passing from pure vanadium to pure tungsten. Such a strong variation of the diffusion coefficients results in extremely asymmetric concentration profiles during interdiffusion experiments. Accordingly, it can be expected that in V-rich regions of the sample the concentration profiles are quite extended, while in the W-rich part of the alloys practically no transport by (volume) diffusion occurs.
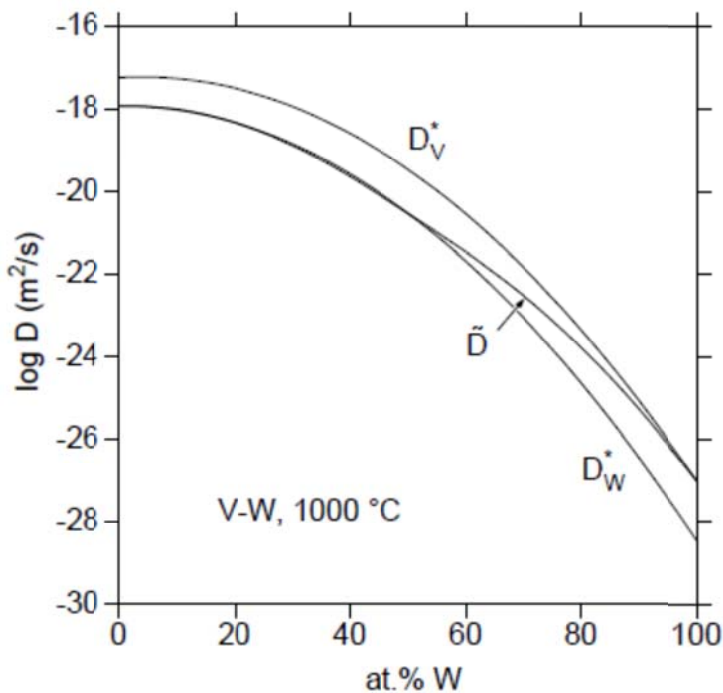
Fig. 37. Composition-dependent tracer diffusion coefficients, D_V^* and D_W^*, and interdiffusion coefficient, $\tilde{D}$, of the V–W system at 1000°C.

In Fig. 38 the concentration profile in the vicinity of the weld between a vanadium and a tungsten sheet is shown after annealing at 1000°C for 100 h. The symbols denote the values of the tungsten concentration which has been measured by Auger electron spectroscopy, while the solid line represents the calculated interdiffusion profile using the DICTRA program. It is striking that the calculation of the concentration profile on the V-rich side is quite good, whereas on the W-rich side not only quantitative but principal deviations from a simple interdiffusion profile are apparent. These deviations can be explained by the microstructure of the metal foils and by their different behaviour during recrystallization. Due to the manufacturing process, the tungsten foils possess an ultrafine-grained microstructure consisting of pancake-shaped grains with a thickness of about 0.5 µm in the S-direction. Contrary to tungsten, vanadium recrystallizes much faster and thus much bigger grain sizes are achieved in the vanadium sheets during the long-time annealings at 1000°C. Therefore, the transport processes in the tungsten sheets are dominated by grain-boundary diffusion while in the vanadium sheets volume diffusion prevails. Since the DICTRA program can only consider diffusion simulations with one independent space coordinate it is not possible to take into account the faster paths along grain boundaries. In particular, these diffusion calculations cannot simulate the local enrichment of vanadium on the tungsten side about 1 µm behind the weld seam. The reason for this effect is the increased diffusivity in the grain boundaries for both components, vanadium and tungsten, whereas these components are practically immobile in the interior of the tungsten grains. Therefore, on the W-rich side of the alloys, vanadium penetrates the microstructure only along the network of grain boundaries. In Fig. 38 the local minimum in the tungsten concentration on the right side indicates the location of a grain boundary which is cut in the given cross-section. Vanadium has diffused around the first tungsten grain along the grain boundaries and the V-concentration is raised at the back side of this grain. At the back side of the following grain, a similar increase in the V-concentration is yet missing because the diffusion time is not long enough.
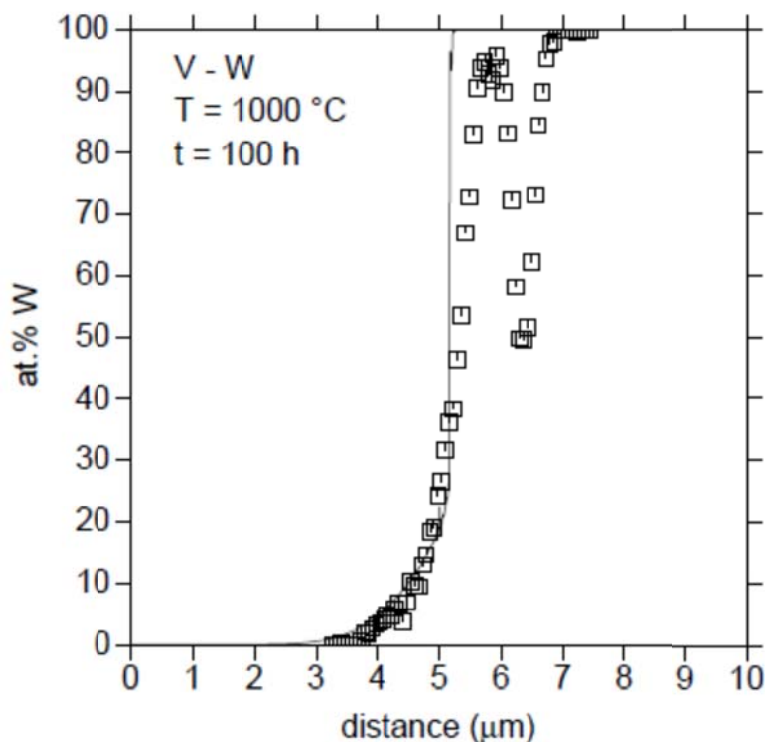
Fig. 38. Interdiffusion profile in W-V laminates after 100 h at 1000°C. The data points were obtained from AES measurements. The solid line represents the calculated diffusion profile.

However, in the V-rich alloys where volume diffusion prevails, the DICTRA program can be used for the determination of the concentration profiles and for the evaluation of diffusion coefficients. As mentioned above, the impurity diffusion coefficient of tungsten in vanadium has not yet been reported in the literature. However, according to Darken's formula [71], the interdiffusion coefficient coincides with the impurity coefficient in the case of a very diluted alloy, which is also demonstrated in Fig. 37. Therefore, the hitherto unknown value of the impurity diffusion coefficient of tungsten in vanadium has been adjusted with the DICTRA program by trial and error until the calculated interdiffusion profile was in satisfactory agreement with the experimental points on the vanadium-rich side, as shown in Fig. 38. The resulting value for the respective diffusion coefficient at 1000°C is:

$$D_W^*(x_V \rightarrow 1) = 1.2 \cdot 10^{-18} m^2 / s \, .$$

4.3.1.2. Evolution of the microstructure of W-V laminates through annealing

Figs. 39, 40 and 41 display the results of electron microscopy analyses of the microstructural evolution of the tungsten-vanadium interface during annealing. Fig. 39 displays a series of SEM images of the interface in the as-produced condition as well as after annealing for 10, 100 and 1000 h at 1000°C (1273 K). Fig. 40 provides AES line scans and Fig. 41 displays AES element mappings. These figures make it possible to identify the following diffusion mechanisms and microstructural changes during annealing.
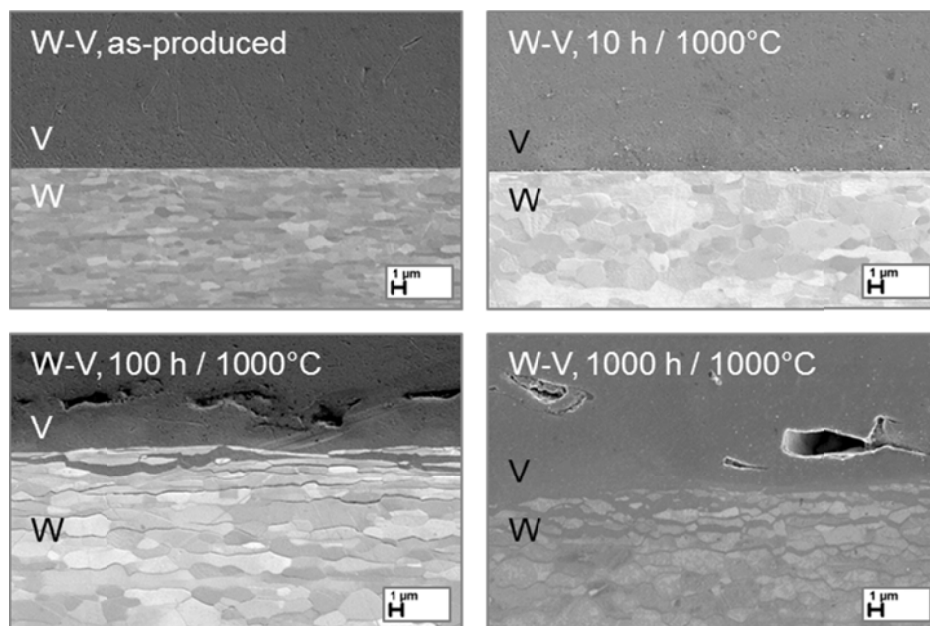

Fig. 39. SEM analyses of the tungsten-vanadium interface.

Let us start with the W-rich side first. The microstructure of the W-rich side is fine-grained in the as-produced condition. However, during a heat treatment of 10 h at 1000°C (1273 K), the median grain size increases (Fig. 39). Furthermore, there is nearly no volume diffusion of vanadium in tungsten, which can be clearly seen in the thermal colour maps from Fig. 41. Moreover, there is a pronounced grain boundary diffusion of vanadium along the tungsten grain boundaries. Grain boundaries are the preferred diffusion paths. This grain boundary diffusion causes the continuous detachment of whole tungsten grains. This is obvious when

considering e.g. the shape of the line of the element distribution of the 1000 h at 1000°C annealed samples from Fig. 40. The situation looks rather different for the V-rich side.
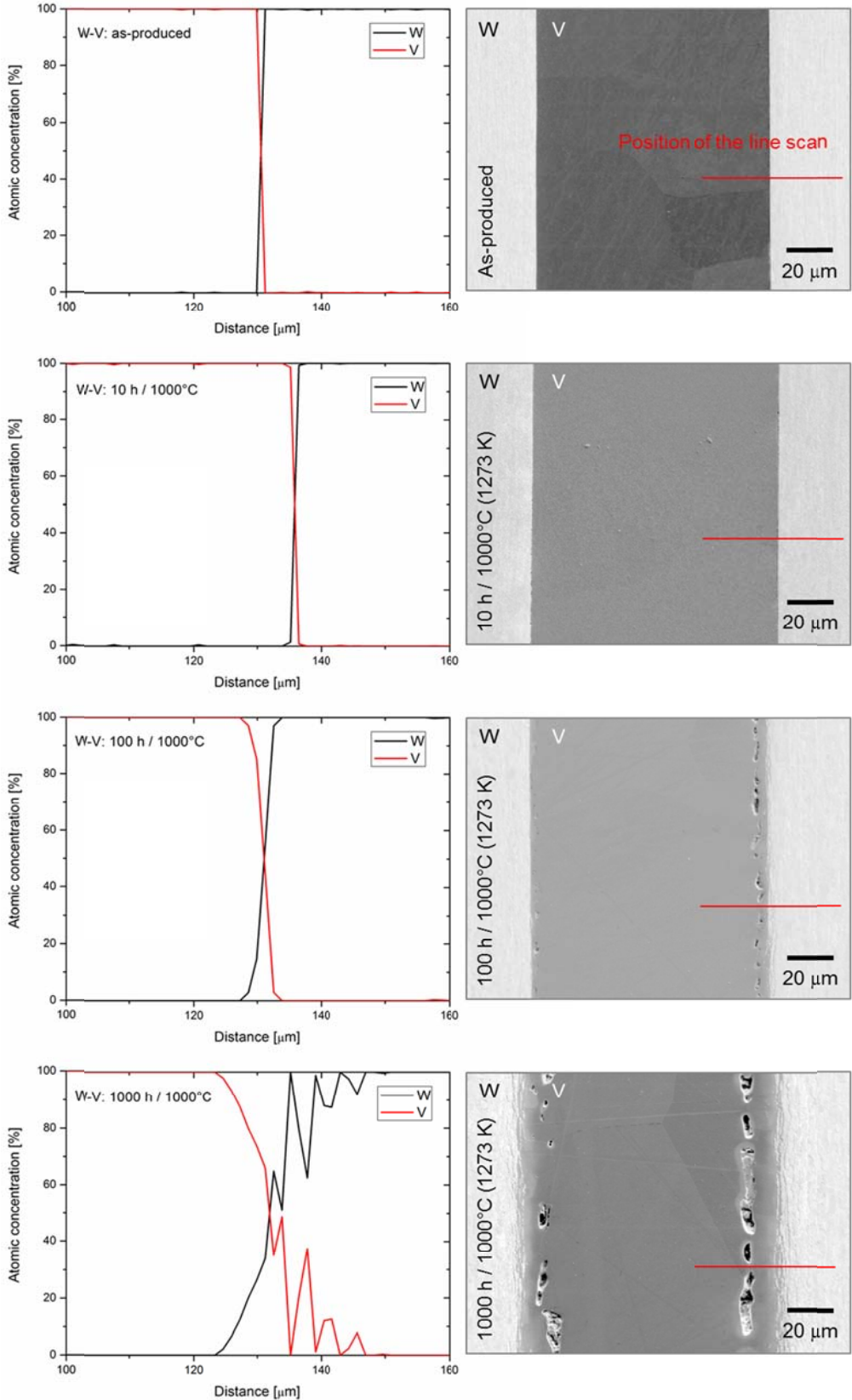

Fig. 40. AES line scans displaying the evolution of the tungsten-vanadium interface. The position of the line scans is marked by a red line in the SEM images.

61

The microstructure in the V-rich side is already coarse-grained in the as-produced condition. There are about one or two grains spanning the distance from one tungsten ply to the other. So for the V-rich side, lattice diffusion of tungsten in vanadium is of great importance. The volume diffusion of tungsten into vanadium can be clearly seen in the AES analyses in Fig. 40 and 41. So, in the interdiffusion zone of the V-rich side a continuous formation of a V-W solid solution takes place. Furthermore, the V-rich side shows rows of pores. These pores can be seen in the optical micrograph in Fig. 35 in samples that experienced a heat treatment of 100 h at 1000°C. The pores are situated in the interdiffusion zone and may be traced back to the Kirkendall effect. In Fig. 37 we showed that the diffusion of vanadium into tungsten is ten orders of magnitude faster than the diffusion of vanadium in tungsten. This causes a vacancy stream from the W-rich side to the V-rich side. Due to vacancy flux the V-rich side accumulates an excess of vacancies which has to be eliminated in order to restore the local thermodynamic equilibrium. In the case of our W-V laminates this process leads to the formation of Kirkendall pores in the V-rich part of the interdiffusion zone. However, it should be noted that in W-Ti laminates under similar conditions no Kirkendall pores have been found. This leaves the question of whether or not the formation of Kirkendall pores is a function of the microstructure of the V-rich or Ti-rich side. Ongoing work should elucidate this issue.
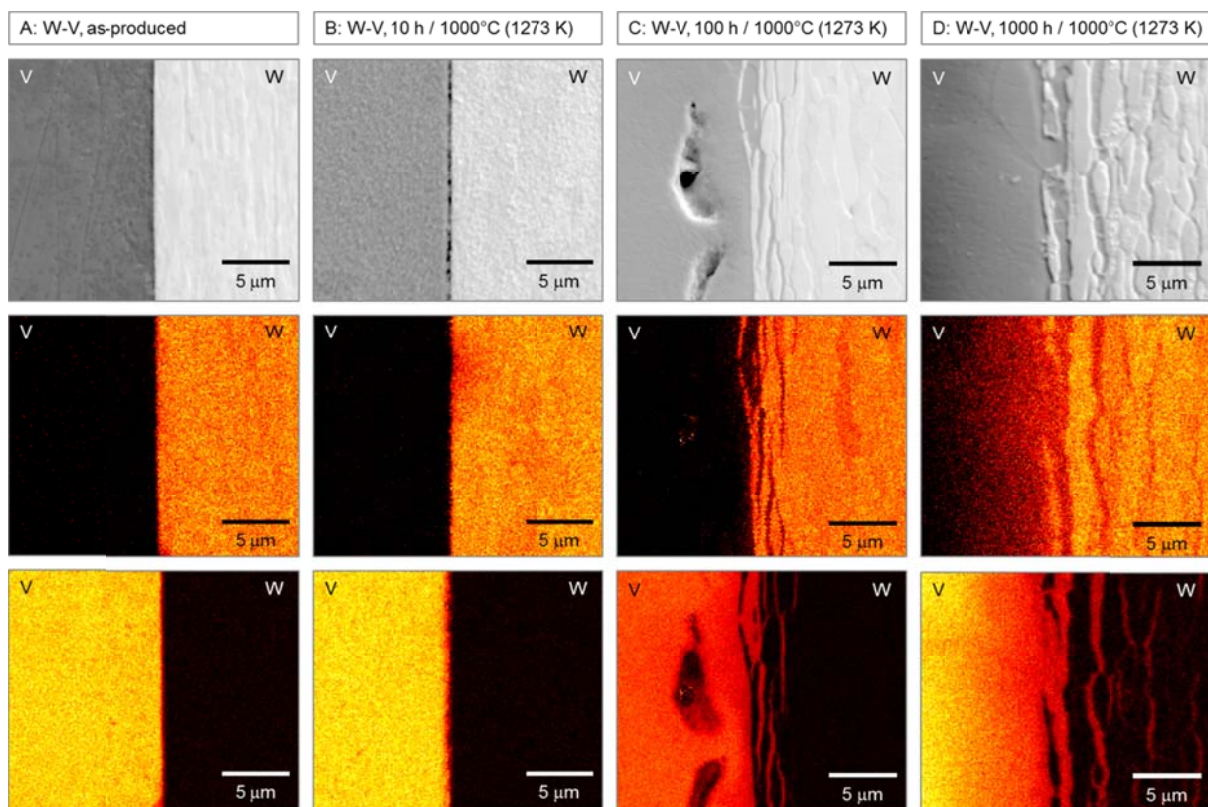

Fig. 41. AES analyses of the tungsten-vanadium interface in different ageing conditions. On the coloured thermal map, black refers to a low content and yellow to a high content of a specific element.

4.3.2. Diffusion mechanisms in W-Pd laminated composites

By analogy with the previous chapter, we will discuss diffusion mechanisms in W-Pd laminated composites by evaluating the thermodynamic properties of the Pd-W system and by assessing the evolution of the microstructure by means of electron microscopy analyses.

Again, the laminates were produced by diffusion bonding at 900°C (1173 K) for 1 h in vacuum. Afterwards, the laminates were annealed for 10, 100 and 1000 h at 1000°C (1273 K).

4.3.2.1. Thermodynamic and diffusional properties of the Pd-W system

The maximum solubility of tungsten in palladium at 1100°C (1372 K) is 21.5 at %, and the maximum solubility of palladium in tungsten at 1100°C is 1.5 at %. Below this temperature, the maximum solubility of tungsten in palladium and palladium in tungsten is expected not to change significantly [72].
Furthermore, it is suggested that the system has an intermediate Pd_3W-phase formed below 900°C (1173 K) and with a hexagonal structure. According to the present state-of-the-art, it is unknown up to which temperature the Pd_3W-phase is stable. Based on the results of our ageing experiments (up to 1000 h at 1000°C (1273 K)), we confirm that the intermetallic Pd_3W-phase is not stable at 1000°C.

It seems that in the Pd-W system only the self-diffusion coefficients are known [68], but the respective impurity diffusion coefficients and the interdiffusion coefficients have not yet been investigated. However, in view of the self-diffusion coefficients [68] we expect that the interdiffusion in the Pd-rich fcc phase is by several orders of magnitude faster than in the W-rich bcc phase. This assumption is corroborated below by the AES diffusion profiles.

4.3.2.2. Evolution of the microstructure of W-Pd laminates through annealing

Figs. 42, 43 and 44 display the results of electron microscopy analyses of the microstructural evolution of the tungsten-palladium interface during annealing. Fig. 42 displays a series of SEM images of the interface after annealing for 10 and 100 h at 1000°C (1273 K). Fig. 43 provides AES line scans and Fig. 44 displays AES element mappings. These figures make it possible to identify the following diffusion mechanisms and microstructural changes during annealing.
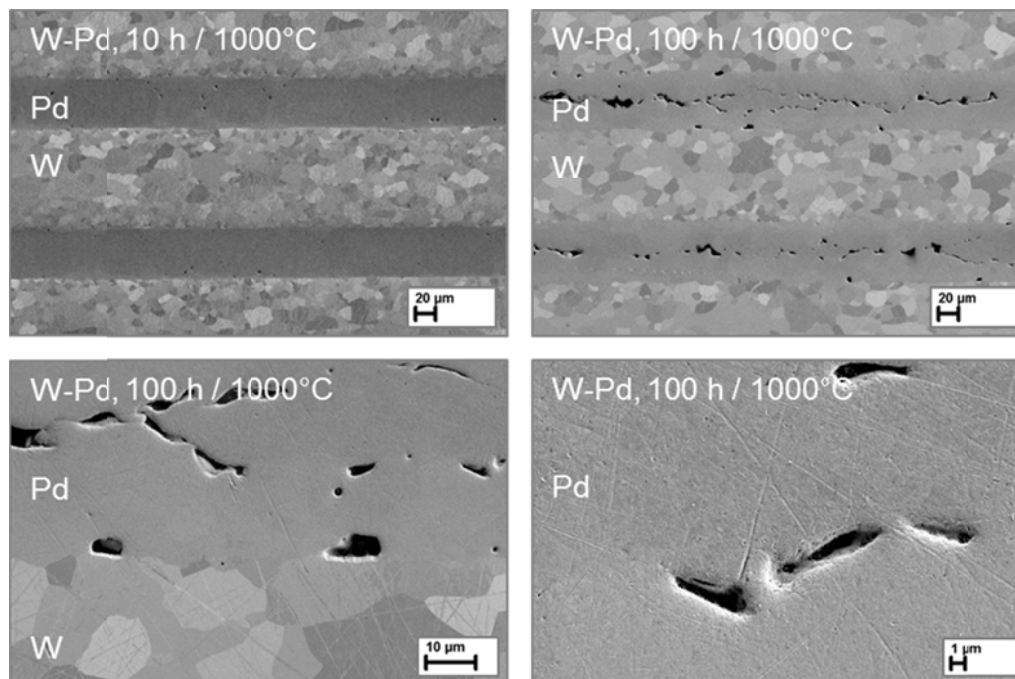

Fig. 42. SEM analyses of the tungsten-palladium interface.

The first point to mention is that the measurements of the AES line scans from Fig. 43 fit perfectly well with the data from the phase diagram. The phase diagram displays a maximum solubility of tungsten in palladium at 1100°C (1372 K) and below of 21.5 at %. This is more or less the value which is found in the Pd-rich phase after annealing for 1000 h at 1000°C (1273 K). Furthermore, the phase diagram reveals that there is only small solubility of palladium in tungsten. This statement is again confirmed by the line scans in Fig. 43, represented by very straight vertical lines at the palladium-tungsten interfaces. The solubility of tungsten in palladium and the very low solubility of palladium in tungsten at the relevant temperatures are also confirmed by the coloured thermal maps in Fig. 44.

Let us now focus on the W-rich phase. The lattice diffusion of palladium into tungsten is very slow and will be neglected in the further discussion. However, grain boundary diffusion will be taken into account. Astonishingly, the microstructure of the W-rich phase is already coarse-grained after a heat treatment of 10 h at 1000°C (1273 K). This distinguished the W-rich phase of the W-Pd laminate from the W-rich side of all the other laminates reported in this paper (i.e. W-Cu, W-V, W-Ti). The reason for this behaviour is unknown. One may speculate that the grain boundary diffusion of palladium into tungsten may enable the easy migration of high angle grain boundaries. However, this is just a vague assumption and is not grounded on a sound statistical basis.

The Pd-rich phase shows the formation of considerable pores after a heat treatment of 100 h and more at 1000°C (1273 K). The pores form a chain and are positioned in the very middle of the palladium plies. At first glance, one may speculate that the pores are caused by the Kirkendall effect. However, the formation of Kirkendall pores is in general in the interdiffusion zone. As the pores are predominantly found in the very middle of the palladium sheets, we assume that the explanation for the origin of the pores by the Kirkendall effect is not reasonable.
Moreover, one may speculate that the pores formation is caused by changes in the lattice parameter. The lattice parameter, a, has been measured by X-ray measurements. It was found that for 0 at % W the lattice parameter is 0.38889 nm. At a value of around 10 at % W, a minimum in the lattice parameter has been observed (a = 0.38857 nm) before it starts increasing with increasing tungsten content (20.2 at % W: a = 0.38925 nm) [72]. However, we do not think that this is a reasonable explanation either.
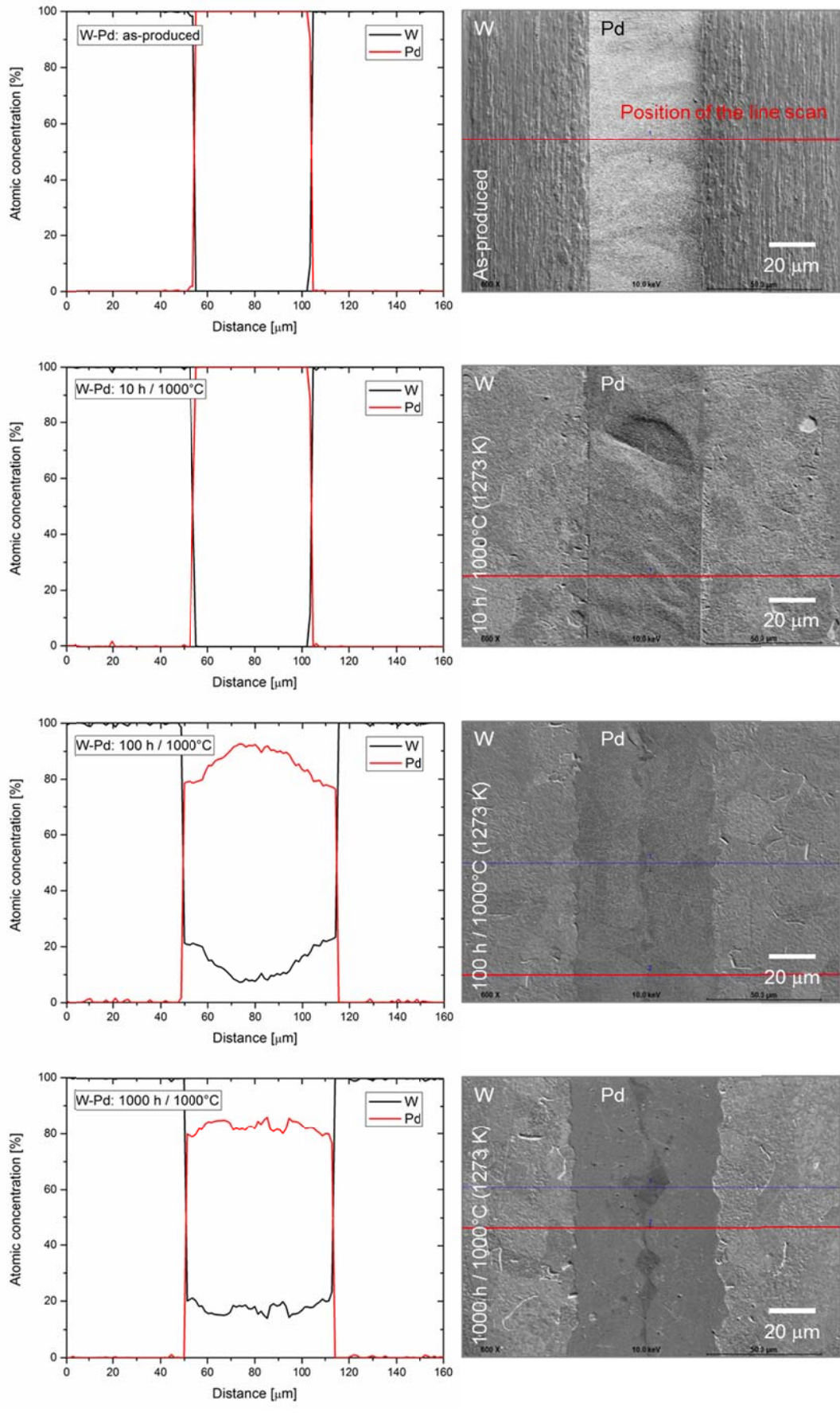
Fig. 43. AES line scans from tungsten to tungsten via the palladium interlayer.

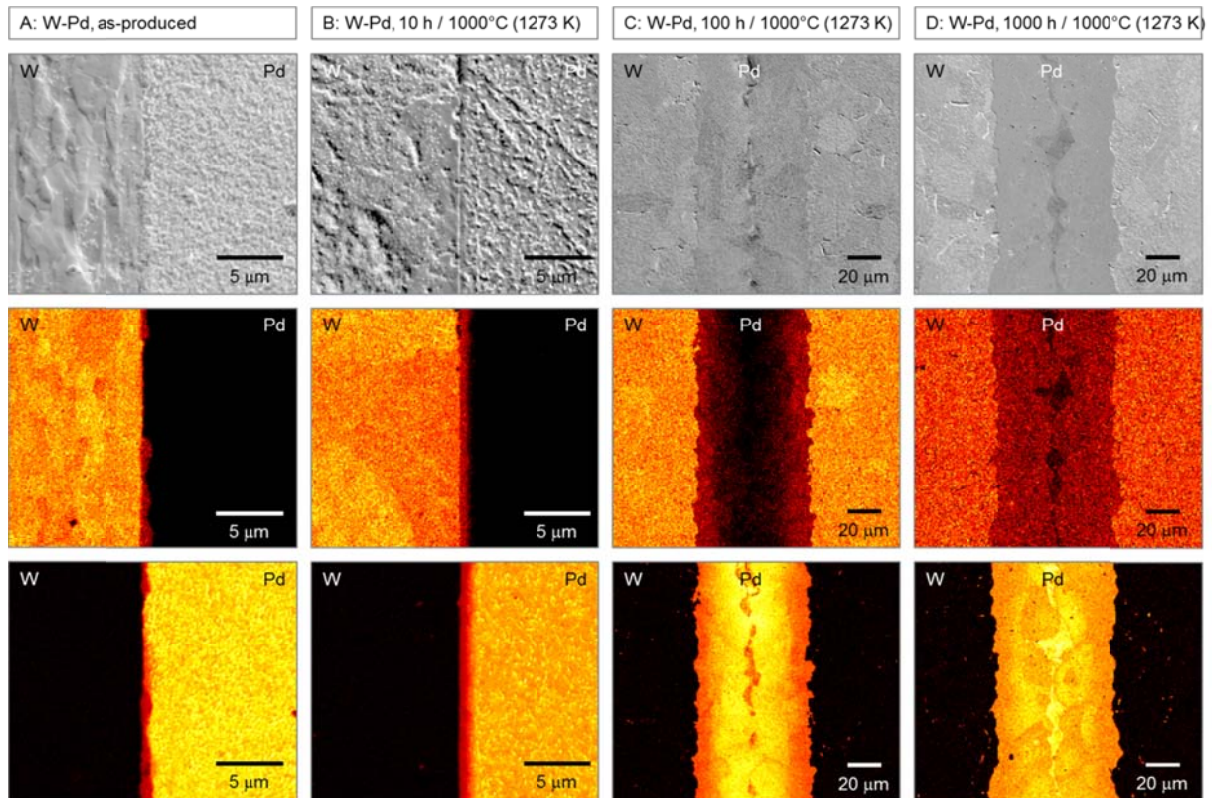| A: W-Pd, as-produced | B: W-Pd, 10 h / 1000°C (1273 K) | C: W-Pd, 100 h / 1000°C (1273 K) | D: W-Pd, 1000 h / 1000°C (1273 K) |

Fig. 44. AES analyses of the tungsten-palladium interface in different ageing conditions. On the coloured thermal map, black refers to a low content and yellow to a high content of a specific element.

All in all, we come to the conclusion that the formation of pores in W-V and W-Pd laminates needs to be assessed by further systematic tests. In particular, the fact that we did not find any pores in the annealed W-Ti laminates emphasises the necessity to look at this issue more closely.

4.3.3. Evolution of the hardness (HV0.1) through annealing

Figs. 45A and B show the evolution of the hardness of W-V and W-Pd laminated composites. In Fig. 45A, the hardness of the W-rich side is displayed, while in Fig. 45B the hardness of the V-rich or Pd-rich side is shown respectively. Furthermore, for the sake of comparison, these figures also include the evolution of hardness in W-Cu and W-Ti laminated composites. The hardness values were obtained from indentations that were positioned in the middle of the tungsten or the interlayer sheet.

Let us discuss the evolution of the hardness in the W-rich side first (Fig. 45A). Any changes of the hardness in the W-rich side can be traced back to (i) recovery and recrystallisation processes and (ii) grain boundary and volume diffusion of elements of the interlayer into tungsten.
The evolution of the hardness of the W-rich phase of W-Cu laminates serves as a benchmark, as for this type of laminate the evolution of the hardness in the W-rich phase is only caused by recovery and recrystallisation processes. Diffusion of copper into tungsten can be neglected.

Discussion of the evolution of the hardness of the W-rich side in W-V laminated composites is straightforward. Fig. 45A clearly shows the exponential evolution of the hardness, represented by a straight line on the semi-logarithmic plot. This behaviour is similar to that of W-Cu laminated composites. This shows that the impact of grain boundary diffusion or volume diffusion of vanadium in tungsten is below the resolution limit of the hardness measurement.

The situation looks different for the W-rich side of a W-Pa laminated composite. In the as-produced condition, the hardness of its W-rich side is congruent with the hardness of the W-rich side of a W-Cu or W-V laminated composite. However, after annealing for only 10 h at 1000°C (1273 K), the hardness reaches values of about 400 HV0.1, which is in the range of the hardness of a tungsten single crystal [4]. So, according to the hardness measurement, the W-rich side should possess a very coarse-grained microstructure, which is confirmed by the SEM images from Fig. 42. This leads to the question of what mechanisms cause this grain-coarsening of the W-rich side in W-Pd laminated composites.

As discussed in the previous section, the W-Pd phase diagram reveals that there is less solubility of palladium in tungsten. This is confirmed by the sharp phase boundary, as indicated by the AES analyses in Figs. 43 and 44. This means that only grain boundary diffusion of palladium into tungsten has to be considered. One may speculate that this grain boundary diffusion is very intense. Thus, after a short annealing time, most of the tungsten grains may be covered with palladium. One may further speculate that either (i) the palladium supports the migration of the tungsten HAGBs or (ii) volume diffusion of tungsten into the palladium grain boundary layer takes place, which produces a Pd-rich solid solution. However, these are only assumptions that have to be confirmed by further systematic tests.
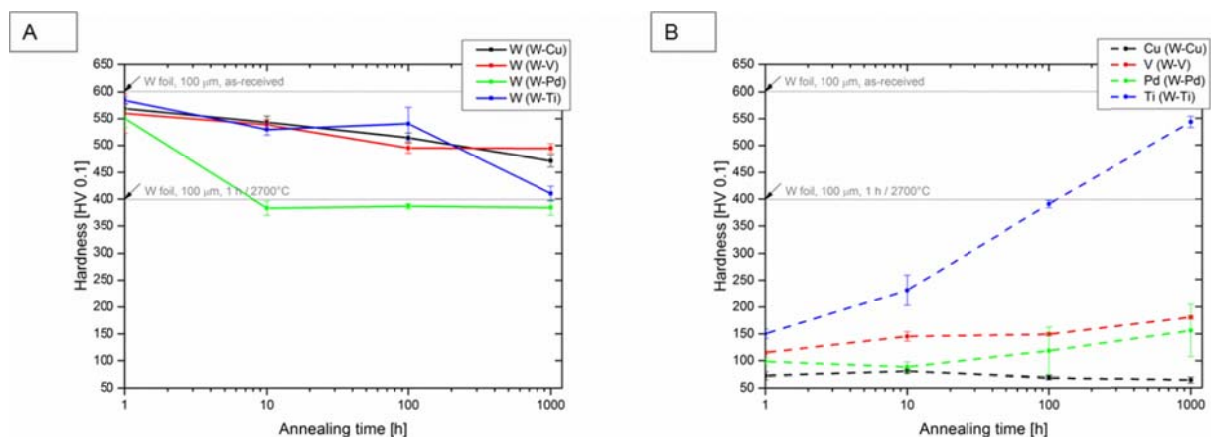

Fig. 45. Comparison of the evolution of the hardness (HV0.1) of the W-rich side (A) and the interlayer-rich side (B) of W-Cu, W-V, W-Pd, and W-Ti laminated composites. The indentation of the hardness measurement was positioned in the centre of the corresponding side. The conditions (i) as-produced (i.e. 1 h at 900°C (1173 K)) and annealed for (ii) 10 h, (iii) 100 h, and (iv) 1000 h at 1000°C (1273 K) are considered. Values represent the average from n = 6 indents (error bars: standard deviation).

Let us now discuss the evolution of the hardness in the V-rich and Pd-rich side (Fig. 45B). Both sides have in common that their microstructure is coarse-grained immediately after the synthesis of the laminate for 1 h at 900°C (1173 K). Thus any changes of the evolution of the hardness of the V-rich and Pd-rich side cannot be traced back to recrystallisation processes but have to be discussed against the background of (i) solid solution hardening and (ii) the formation of voids by e.g. the Kirkendall effect.

Again, the evolution of the hardness of the Cu-rich phase of a W-Cu laminate serves as a benchmark. For this type of laminate, the evolution of the hardness in the Cu-rich phase may not change through annealing, as (i) the Cu-rich phase is in its recrystallised condition immediately after the material synthesis and (ii) there is almost no solubility of tungsten in copper, so any effects caused by volume diffusion (solid solution hardening, void formation

by the Kirkendall effect) can be neglected. These assumptions are confirmed by the horizontal line in Fig. 45B, representing the evolution of the hardness of the Cu-rich phase.

In the V-rich side, the hardness increases slightly with increasing annealing time. Volume diffusion of tungsten into vanadium and the formation of a V-rich solid solution may not contribute to this increase in hardness. As can be seen from the AES line scans in Fig. 40, there is no measurable formation of a solid solution. Furthermore, the hardness measurement in the V-rich side is not affected by the formation of voids. The manifestation of the voids is at the borders of the vanadium interlayers, whereas the position of the indentations for the hardness measurements was in the centre of the vanadium layers. This leaves grain boundary diffusion of tungsten in vanadium as the only mechanism responsible for the slight increase in hardness.

In the Pd-rich phase of a W-Pd laminated composite, the hardness also increases slightly with increasing annealing time. However, the mechanisms causing this increase in hardness are different from those of the increase in hardness of the V-rich side of a W-V laminate. As can be seen from the line scans in Fig. 43, there is the formation of a Pd-rich solid solution, caused by volume diffusion of tungsten into palladium. This solid solution formation causes an increase in hardness. Note that the measured hardness values were obtained from areas that contained voids. So the measured hardness values give a homogenised value of the contributions of (i) solid solution and (ii) voids. The sum of both contributions leads to the overall increase in hardness.

In summary, the evolution of the hardness can be caused by (i) recovery and recrystallisation, (ii) the formation of a solid solution, and (iii) the formation of voids (e.g. the Kirkendall effect). The contributions of these mechanisms to the overall hardness differ from one laminate to another.

4.3.4. Evolution of the Charpy impact properties through annealing

Fig. 46 displays the change of the Charpy impact properties through annealing for 10, 100 and 1000 h at 1000°C (1273 K) for W-Cu (Fig. 46B), W-V (Fig. 46C), W-Pd (Fig. 46D), and W-Ti (Fig. 46E) laminated composites. For details on the evolution of the Charpy impact properties of W-Ti laminates, the reader is referred to Ref. [27]. The Charpy impact properties of a pure tungsten plate material serve as a benchmark and are shown in Fig. 46A. Details on the evolution of the microstructure of the annealed plate materials can be gained from the IPFs shown in Fig. 47. All samples represent the L-S crack system and are of KLST type.

In Sections 4.1. "W-AgCu laminates", and 4.2. "W-Cu laminates", we investigated the main energy dissipation mechanisms of the model systems W-AgCu and W-Cu. We came to the conclusion that the Charpy impact properties are governed by the plastic deformation of the tungsten plies. Based on this result, it is necessary to first focus on the tungsten microstructure and to discuss the evolution of the Charpy impact properties against the background of the evolution of the microstructure of the tungsten plies.
The following changes of the tungsten microstructure affect the Charpy impact performance: (i) recovery and recrystallisation, (ii) the formation of an intermetallic compound, and (iii) the formation of a solid solution.
Note that the volume diffusion of vanadium or palladium into tungsten is very low (see also titanium) and can thus be neglected. However, grain boundary diffusion of vanadium or palladium into tungsten and the subsequent volume diffusion of tungsten into the vanadium or palladium grain boundary layer have to be taken into account.

Let us start with the analysis of the evolution of the Charpy impact properties of the annealed plate material. Fig. 46A shows that plate material in its as-received condition starts to dissipate energy at a test temperature of 400°C (673 K) and reaches the upper shelf energy at 500°C (773 K). In the temperature range from 400°C (673 K) to 500°C (773 K), the transition from "brittle" to "delamination" takes place, thus we define 450°C (723 K) as the best case limit. Through annealing for 10 and 100 h at 1000°C (1273 K), the Charpy impact properties do not change significantly. However, after a heat treatment of 1000 h at 1000°C (1273 K) or 1 h at 2000°C, the Charpy impact properties are severely deteriorated. From this, we infer that the BDT temperature of recrystallised tungsten plates is higher than 1100°C (1373 K) and so is the worst case limit.

In Fig. 46B, we also defined a best case and a worst case limit for W-Cu and W-AgCu laminated composites. The best case limit results from Charpy impact tests on W-AgCu laminates that have been built up of tungsten foils in their as-received condition, whereas the worst cases limit was derived from Charpy impact tests on W-AgCu laminates made of recrystallised foils (1 h at 1800°C (2073 K)). A comparison of Figs. 46A and B clearly demonstrates the improvement of the impact properties of the tungsten laminates compared to pure tungsten plate materials in both their as-produced and recrystallised conditions.

The disadvantage of W-Cu laminated composites is that their operation window is limited at the upper end by the melting of the copper interlayer, which is at 1084°C (1357 K). Thus, the motivation for the W-V and the W-Pd laminates is to produce a multilayer material with an enhanced operation window at the upper temperature regime. However, we have to admit that these approaches failed, as can be seen in Figs. 46C and D. The Charpy impact properties of W-V laminates are good in their as-produced and their annealed for 10 and 100 h at 1000°C (1273 K) conditions. However, after a heat treatment of 1000 h at 1000°C (1273 K), the Charpy impact properties were severely deteriorated. This behaviour seems reasonable when considering the formation of the Kirkendall pores in the V-rich side (Figs. 35 and 39). These pores weaken the material's integrity and define the preferred fracture path in the laminated composites. Therefore, the W-V laminates, annealed for 1000 h at 1000°C (1273 K) do not fracture along the ligament plane, but fail by multiple delaminations and the crack path is within the V interlayer and guided by the chains of Kirkendall pores.

The situation for the W-Pd laminates is even worse, and can be seen in Fig. 46D. The impact properties are unacceptable in the as-produced condition and are severely worsened after 10 h at 1000°C (1273 K).

In summary, it can be said that the impact properties of W-Cu laminated composites are convincing. However, these laminates are limited at the upper operation window by the melting of the copper interlayer. This is why we produced and analysed laminates with a high melting point interlayer, such as W-V, W-Pd and W-Ti composites. It can be concluded that the impact properties of all these laminates deteriorate through annealing and that at least after a heat treatment of 1000 h at 1000°C (1273 K), the mechanical properties are unacceptable. Thus, the question of how to produce successful laminates with an increased operation window compared to W-Cu laminates arises. A possible strategy will be introduced in the next section.
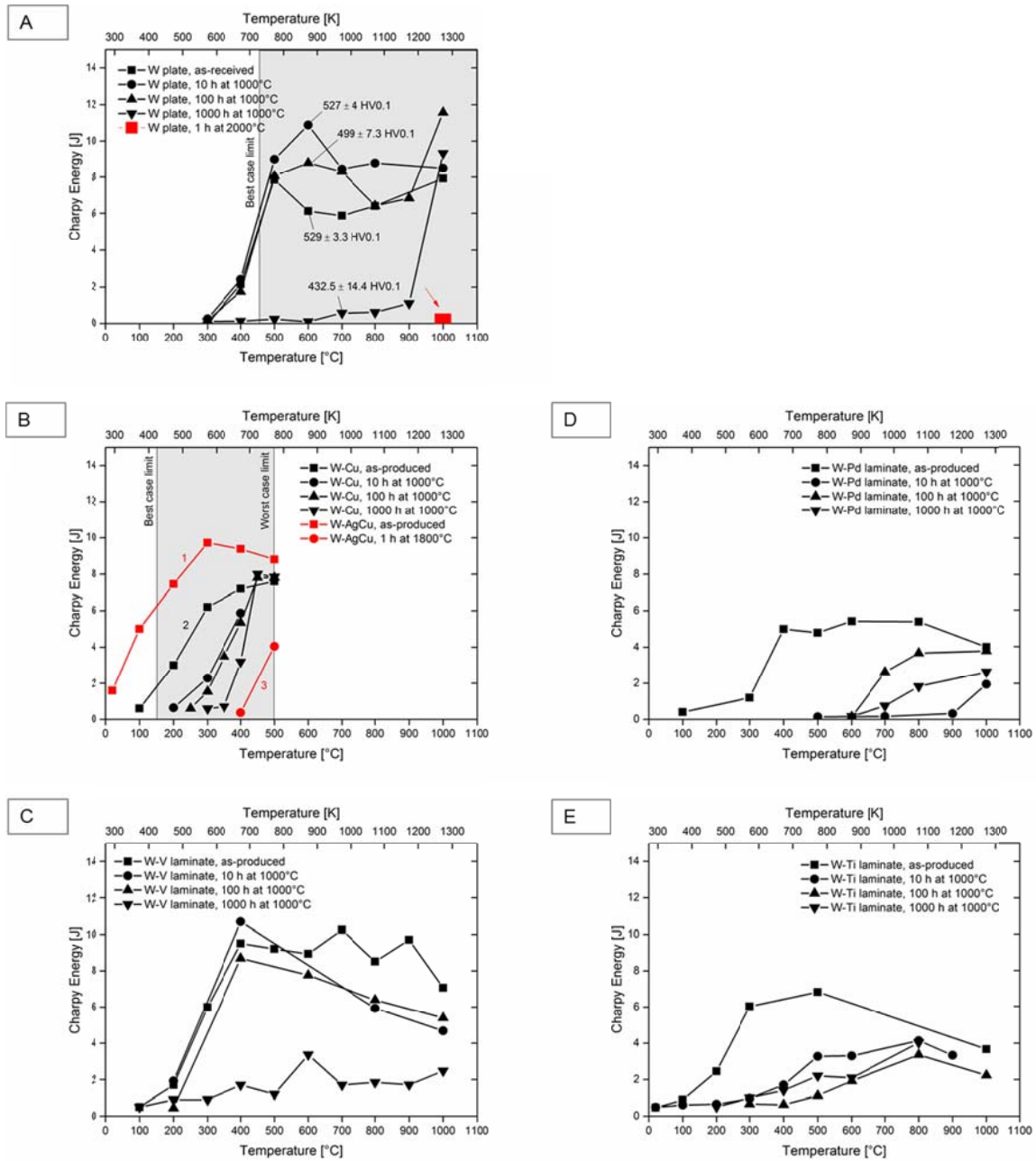
Fig. 46. Comparison of the evolution of the Charpy impact properties of W-Cu (B), W-V (**C**), W-Pd (D), and W-Ti (E) laminated composites. The results are benchmarked against the Charpy impact properties of the pure tungsten plate material (A).
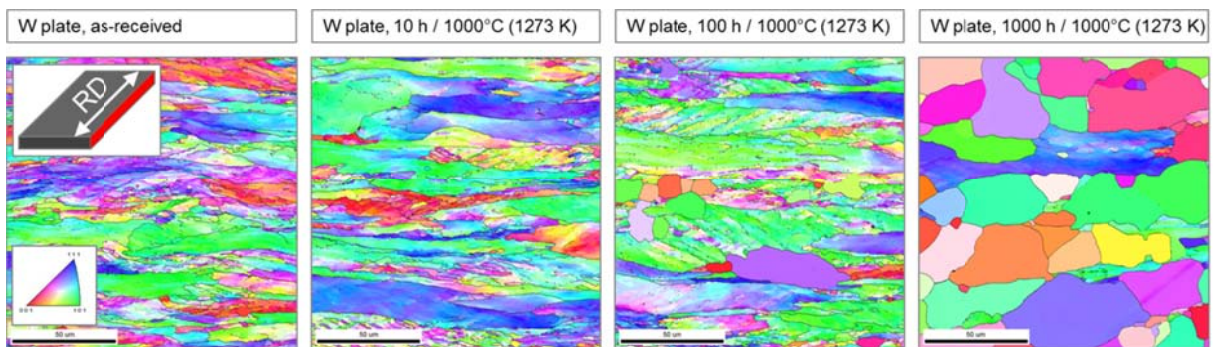

Fig. 47. Evolution of the microstructure of a hot-rolled tungsten plate during annealing. The IPFs provide a view in the T-direction. Misorientations exceeding 15° are considered as HAGBs and are highlighted in black. The

70

formation of recrystallisation nuclei, followed by primary recrystallisation (migration of HAGBs) can be seen. This shows that the recovery and recrystallisation behaviour of hot-rolled, coarse-grained tungsten sheets differs from that of heavily cold-rolled, ultrafine-grained tungsten sheets. For the latter, grains do not produce recrystallisation nuclei, so primary recrystallisation is suppressed and the deformation texture is inherited.

4.4. W-W laminates: On the potential of tungsten laminates without interlayers

The idea for the W-W laminated composites is to produce a material that is not a composite at all. It is a material that is made of tungsten foils only and no interlayer is used. In this way, we intend to produce a bulk material with a thickness of e.g. 1 mm or even more, that possesses an ultrafine-grained, cold-rolled microstructure, combined with the melting temperature of pure tungsten. Thus, W-W laminates can be regarded as a type of pure tungsten. The question is whether W-W laminates can be produced with a quality that allows for the determination of Charpy impact properties and whether the mechanical properties are still superior compared to the properties of the benchmark plate materials.

Charpy impact test samples with dimensions of 1 mm x 3 mm x 27 mm, without notch, were produced by diffusion bonding of 10 layers of 100 μm-thick tungsten foil. The bonding parameters were 1 h, 35 MPa, and vacuum. No interlayer was used. The bonding temperatures were 900°C (1173 K), 1000°C (1273 K), 1100°C (1373 K) and 1200°C (1473 K). The specimens represent the L-S crack system.

The impact of the joining temperature on the tungsten-tungsten interface can be seen in Fig. 48A. With increasing joining temperature, the quality of the interface continuously increases. However, with increasing joining temperature, thermally activated processes, such as recovery and recrystallisation, become more important. Thus, the sample joint at 1200°C (1473 K) shows the most coarse-grained microstructure compared to the microstructures of the samples joint at lower temperatures. This clearly demonstrates the necessity for not only producing an ultrafine-grained microstructure, but also for finding a way to stabilise this microstructure towards thermal energy.

Nevertheless, the W-W laminates that have been diffusion bonded at 1200°C (1473 K) have been characterised by means of Charpy impact tests, and the results can be seen in Fig. 48B. For details on the benchmark properties obtained from a hot-rolled and a recrystallised plate, the reader is referred to Ref. [7]. It is very encouraging and convincing to see that (i) W-W laminates are testable and (ii) their impact properties are superior compared to the properties of the benchmark materials. The sample tested at 300°C (573 K) can be seen in Fig. 48B.

This promising result may act as a motivation for further in-depth investigations of W-W laminates. The production of W-W laminated pipes by a hot isostatic pressing process is envisaged in the next step. However, the development of W-W laminated composites must necessarily also contain the development of a thermal-stabilised ultrafine-grained microstructure.
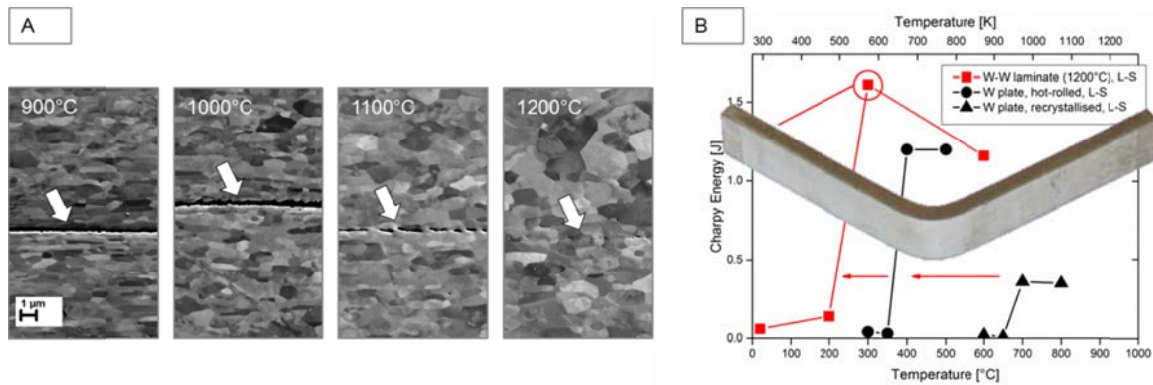
Fig. 48. Feasibility study on the potential of W-W laminated composites. A: W foils were diffusion bonded without the use of any interlayer. With increasing bonding temperature, the quality of the interface increases. B: Charpy impact tests demonstrate the performance of the W-W laminates. Their brittle-to-ductile transition occurs at a lower temperature compared to the brittle-to-ductile transition of the benchmark plate materials.

5. Summary and conclusions

The aim of this paper was to elucidate mechanisms of plastic deformation and fracture of tungsten laminated composites.

The motivation for investigating tungsten laminates was to determine whether a bulk material can be made that retains the toughness, crack growth resistance, brittle-to-ductile transition temperature, and tensile ductility of the thin, severely cold-rolled, ultrafine-grained tungsten foils.

We analysed model systems of mutually nonreactive materials, such as W-AgCu and W-Cu laminates. Furthermore, we assessed laminates that have been built up using a high melting point interlayer, such as W-V and W-Pd laminated composites (for details on W-Ti laminates, the reader is referred to Ref. [27]). Finally, we investigated laminates that were made of tungsten foils only. These laminates are referred to as W-W laminates as no interlayer is used.

Three-point bending, Charpy impact, and tensile tests have been performed to determine the mechanical properties in the as-produced condition and after annealing for 10, 100 and 1000 h at 1000°C (1273 K).

A further aim of this paper was to demonstrate the technical maturity of this type of material and to present the use of laminates in successful plasma-facing components of a nuclear fusion device. Components in which laminates were used as either heat spreaders, interlayers with an adjusted coefficient of thermal expansion, or even as structural pipes, have been introduced and characterised by means of high heat flux testing in GLADIS.

Finally, we elucidated the diffusion mechanisms in W-V and W-Pd laminated composites. This was done by evaluating the thermodynamic and diffusional properties of the V-W and Pd-W system and by performing in-depth microstructural investigations by means of SEM and AES analyses.

Our investigations yielded several results that are now summarised as follows.

Referring to the main questions posed in Section 4.1. "W-AgCu laminates", we can now answer the following questions:

- **What is the damage tolerance of W-AgCu laminates (L-S)?**
  At room temperature, the tungsten plate material fails by fast fracture. The fracture behaviour of the laminated composite is rather different. After cracking of a tungsten sheet, the crack is arrested in the soft AgCu interlayer. This behaviour is indicated graphically by a serrated load–displacement curve (Fig. 4).

- **What are the main energy dissipation mechanisms in tungsten laminated composites (plastic deformation of the tungsten foils, plastic deformation of the interlayer sheets, creation of new surfaces)?**

  The main energy dissipation mechanism has been identified as the plastic deformation of the tungsten foil (Fig. 5B). Further contributions to the total amount of dissipated energy, such as the plastic deformation of the interlayer or the creation of new surfaces, are of secondary importance.

- **What is the origin of the anisotropy of the Charpy impact properties (L-S, LT-S, T-S)?**

  The fracture and deformation behaviour of W-AgCu laminates is dominated by the mechanical response of the tungsten foils. The anisotropy of the Charpy impact properties can be traced to microstructural features of the tungsten foils, such as the preferred cleavage plane, crystallographic texture and the grain size anisotropy (Fig. 3).

- **What is the reason for the improved Charpy impact properties of recrystallised W-AgCu laminates compared to their recrystallised plate material counterparts?**

  The BDT of the recrystallised W-AgCu laminates occurs at a temperature that is at least 600 K lower than the BDT temperature of the recrystallised plate material counterparts. What distinguishes the recrystallised laminate from the recrystallised plate material is the fact that the laminated composite possesses several bcc–fcc interfaces. These interfaces may allow the absorption and transmission of dislocations. We assume that the absorption/transmission of dislocations at the interfaces supports the nucleation of further shielding dislocations at the crack tip (Fig. 14B). This mechanism may decrease the BDT temperature.

- **What are the tensile properties of W-AgCu laminated composites?**

  The tensile properties in terms of total elongation to fracture, A_t, of these laminates is quite similar to the tensile properties of pure 100 μm-thick tungsten foils (Figs. 15A and B). This result may be traced back to two mechanisms: (i) during tensile testing, delamination at the interface between tungsten and the AgCu interlayer may occur and thus the tungsten sheets of the laminate behave like individual foils, and (ii) the residual stresses in the W-phase of a W-AgCu laminate in its as-produced condition are not high enough to cause an improvement of the tensile properties.

Returning to the questions from Section 4.2. "W-Cu laminates", we can draw the following conclusions:

- **How do the Charpy impact properties change through annealing for 10, 100 and 1000 h at 1000°C (1273 K)?**

  In Fig. 19, the graph representing the properties of the as-produced W-AgCu laminates is referred to as "1" (deformation mechanisms associated with the ultrafine-grained microstructure are dominant), and the graph representing the properties of the recrystallised W-AgCu laminates is referred to as "3" (deformation mechanisms associated with coarse-grained thin foils are dominant).

  The evolution of the Charpy impact properties through annealing can be described as follows: with increasing annealing time, the Charpy impact properties gradually worsen and the BDT temperature gradually increases. This finally gives the result that the Charpy impact properties of the annealed W-Cu laminates lie in between the limits bounded by curve "1" (best case limit) and curve "3" (worst case limit) (Fig. 19).

- **Is there a relation between the evolution of the hardness of the tungsten sheets and the evolution of the BDT temperature of the laminates?**
  By plotting the BDT temperature, T_{BDT}, against the hardness (HV0.1), a linear relation of the form

$$T_{BDT}(HV0.1) = 1539\,K - 1.9 * HV0.1 \tag{5}$$

  can be derived. The linear relation between the BDT temperature and the hardness comes as no surprise, as both the relation between the BDT temperature and the grain size and the relation between the hardness and the grain size can be expressed by a Hall-Petch relation.

- **What is the role of the copper interlayer in the unique tensile properties of W-Cu laminates?**
  W-Cu laminated composites possess a total elongation to fracture, A_t, of 15.5 % in a tensile test at room temperature. We discussed two possible contributions of the copper interlayer: (i) it is well known that elongation results are very sensitive to variables, such as the foil thickness. It is also well known that for thin foils under tension, the necking process causes an early onset of plastic instability. With increasing foil thickness, the onset of plastic instability is retarded. With respect to the W-Cu laminates, we assume that the copper phase contributes to the retardation of the onset of the plastic instability that is caused by the necking process under tension loading. Note that if this assumption is true, then a delamination at the tungsten-copper interface may severely deteriorate the tensile ductility of the laminate. (ii) The copper phase causes residual stresses. The residual stresses that are established during the synthesis of the materials are of compression type in the tungsten phase (hydrostatic stresses). During tensile testing, the tungsten phase reaches its yield criterion (deviatoric stresses) at a very low σ_1 stress value (Fig. 21). Thus, for the tungsten phase, a compression stress perpendicular to the tension stress direction can be regarded as the ideal state. Again, in the case of a delamination event between the tungsten and the copper interlayer, the residual stresses locally vanish and the tensile properties of the laminate may severely deteriorate. Furthermore, the deterioration of the tensile properties after a heat treatment of 1 h at 900°C (1173 K) in vacuum clearly demonstrates that the mechanical response of the laminates is governed by the plastic deformation of the tungsten plies (Fig. 23A). So the most important issue is the plastic deformation of the tungsten plies; residual stresses and sheet thickness are of secondary importance.

- **What is the performance of W-Cu laminated pipes in a high heat flux test?**
  W-Cu laminated composites can be used as both functional tungsten (heat spreader, CTE mismatch compensator, structural pipe reinforcement (Figs. 29 and 30)), and structural tungsten (pipe for a cooling medium (Fig. 26)). Laminated pipes have been tested in GLADIS. The pipe failed at 28 MW/m², due to the onset of the boiling crisis, the so-called critical heat flux (Fig. 26).

In Section 4.3. "W-V and W-Pd laminates", we analysed composites with a high melting point interlayer. Our investigations yielded the following results:

- **What are the diffusion mechanisms in W-V and W-Pd laminated composites?**
  For the V-W system, the values of the diffusion coefficients (i.e. the tracer diffusion coefficients, D_V^* and D_W^*, as well as for the interdiffusion coefficient, $\tilde{D}$) are

decreased by ten orders of magnitude when passing from pure vanadium to pure tungsten (Fig. 37). Such a strong variation of the diffusion coefficients results in extremely asymmetric concentration profiles during interdiffusion experiments. Accordingly, it can be expected that in V-rich regions of the sample the concentration profiles are quite extended, while in the W-rich part of the alloys practically no transport by (volume) diffusion occurs. For the Pd-W system and in view of the self-diffusion coefficients [68] we expect that the interdiffusion in the Pd-rich fcc phase is by several orders of magnitude faster than in the W-rich bcc phase. This assumption is corroborated by the AES diffusion profiles.

- **How can AES analyses as well as thermodynamic and kinetic considerations contribute to an in-depth understanding of the evolution of the tungsten-interlayer interface?**
  W-V laminates: On the W-rich side of the laminate, vanadium penetrates the microstructure only along the network of grain boundaries. This causes a detachment of single tungsten grains from the tungsten bulk (Fig. 38).
  W-Pd laminates: It is suggested that the system has an intermediate Pd_3W-phase formed below 900°C (1173 K). According to the present state-of-the-art it is unknown up to which temperature the Pd_3W-phase is stable. Based on the results of our ageing experiments (up to 1000 h at 1000°C (1273 K)), we confirm that the intermetallic Pd_3W-phase is not stable at 1000°C.

- **How do the Charpy impact properties of W-V and W-Pd laminates change through annealing for 10, 100 and 1000 h at 1000°C (1273 K))?**
  The impact properties of W-Cu laminated composites are convincing. However, these laminates are limited at their upper operation window by the melting of the copper interlayer. This is why we produced and analysed laminates with a high melting point interlayer, such as W-V, W-Pd and W-Ti composites. It can be concluded that the impact properties of all these laminates deteriorate through annealing and that at least after a heat treatment of 1000 h at 1000°C (1273 K), the mechanical properties are unacceptable (Fig. 46).

Finally, in Section 4.4. "W-W laminates", the potential of W-W laminates has been investigated. The feasibility study can be summarised as follows:

- **Can W-W laminates be produced at such a high quality that Charpy impact properties can be determined and are these properties still superior compared to the properties of benchmark plate materials?**
  A W-W laminate is a material that is made of tungsten foils only and no interlayer is used. A stack of tungsten foils was diffusion bonded for 1 h and 35 MPa in vacuum. Samples bonded at 1200°C (1473 K) have been characterised by means of Charpy impact tests. Their BDT occurs at a lower temperature compared to the BDT of the benchmark plate materials.

We finally arrive at the main conclusion, which is that the mechanical response of the laminates is governed by the plastic deformation of the tungsten plies. The plastic deformation of the tungsten plies is enhanced and supported by beneficial residual stresses (see tensile properties of W-Cu laminates, Fig. 23A) and dislocation-interface interactions (see BDT of recrystallised laminates, Fig. 8B).

6. Outlook

In this paper we presented some findings related to the mechanical behaviour of laminated composites. One major result yielded by this paper is that the plastic deformation and fracture of tungsten laminated composites are governed by the plastic deformation of the tungsten plies. Therefore, the main key to understand the improved mechanical properties of tungsten laminated composites compared to their pure tungsten bulk counterparts is to understand the mechanisms of plastic deformation and fracture of severely cold-rolled, ultrafine-grained tungsten sheets.

The deformation mechanisms of ultrafine-grained tungsten foils have not been identified yet. In general, the expansion of the understanding of plastic deformation and fracture of conventional coarse-grained polycrystalline materials to materials with grain sizes in the range of nanometres is still incomplete [73]. Bonk et al. and Bonnekoh et al. recently reported studies on the deformation and fracture mechanisms of severely cold-rolled ultrafine-grained tungsten foils (degree of deformation (logarithmic), $\varphi = 4$; median grain size in the S-direction, 240 nm) [32]. Their exceptional results are currently discussed against the background of (i) the ordered glide of screw dislocations (confined plastic slip), (ii) the number and mobility of vacancies, (iii) dynamic/partial recrystallisation, (iv) impeded intragranular dislocation plasticity, and (v) intergranular deformation mechanisms, such as (v-a) grain boundary shear and slip, (v-b) grain rotation or grain boundary migration and (v-c) grain boundaries that act as sources and sinks for lattice dislocations [32, 74].

Against the background of the possible use of tungsten laminated composites in a high-temperature environment, the stabilisation of the ultrafine-grained microstructure is of the utmost importance. We have shown in this paper that the tungsten laminates lose their superior room-temperature properties after a heat treatment of 1 h at 900°C (1173 K). This shows the necessity of developing a tungsten material with a stabilised microstructure. In particular, potassium (K) -doped tungsten wires have proven very successful in suppressing the migration of HAGBs [75-79]. So the development of ultrafine-grained, potassium-doped tungsten foils should be the next step in material development.

However, tungsten laminated composites are much more complex than concentrating on the impact of the tungsten plies only. Residual stresses, dislocation-interface interactions (blocking, vs. absorption and transmission), detachment of the interface, and crack deflection are further important issues that need to be taken into account.

Among the laminated composites, W-Cu laminates and W-W laminates are the most promising candidates.

Against the background of a possible use of a laminate in a fusion device, copper may be replaced by CuCrZr (CuCrZr: 0.5 – 1.2 wt % Cr, 0.03 – 0.3 wt % Zr, Cu balance). Finally, the thickness of the copper interlayer may be decreased to below 1 μm. In this way, it is possible to establish a dimensional size effect, as the plastic zone in the copper phase is now confined and the dislocations have to channel.

The coefficients of thermal expansion of W-Cu laminates composites show several peculiarities: (i) the coefficients of thermal expansion are found outside the region bounded by the rules of mixture, (ii) with increasing temperature, the coefficient of thermal expansion first decreases then gently increases, and (iii) the coefficient of thermal expansion changes during thermal cyclic loading. These peculiarities may be traced back to the plastic deformation of the Cu-phase. By decreasing the thickness of the copper layer, the yield stress in the Cu-phase increases according to the models presented in Section 2.2. "Strength". This offers the possibility of designing multilayer materials that operate solely in the elastic regime.

Until now, we have focused on the Charpy impact properties of samples with a L-S, T-S and LT-S crack system. Ongoing investigations should therefore assess the impact properties of samples with an L-T and T-L crack system (Fig. 49).
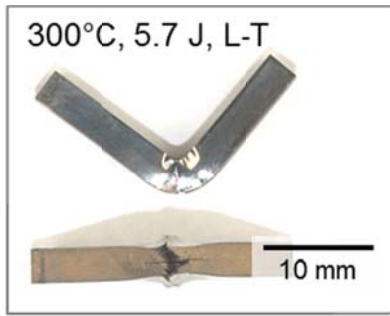
Fig. 49. Result of a Charpy impact test on W-AgCu laminated composites with an L-T crack system. The sample had dimensions of 3 mm x 3 mm x 27 mm, without notch. At a test temperature of 300°C (573 K) the sample dissipated 5.7 J.

This paper yields some interesting results that may hel to design successful irradiation campaigns. A number of recent investigations have discussed the increase of the irradiation resistance of tungsten by increasing the number of grain boundaries and interfaces, as these may act as a sink for radiation-induced defects [80, 81]. There are high expectations that these sinks may produce a denuded zone [82]. And there are, furthermore, high hopes that the size of the denuded zone is somehow of a similar magnitude to the size of the ultrafine grains. Against this background, tungsten laminates made of severely cold-rolled, ultrafine-grained tungsten foils are an interesting candidate for applications in a neutron environment. Irradiation campaigns should take the following issues into account: The room-temperature tensile properties of laminated composites are severely deteriorated after a heat treatment of 1 h at 900°C (Fig. 23A). It is very likely that recovery and recrystallisation processes may even take place at a heat treatment of 1 h at 800°C [33]. Furthermore, the mechanical properties may change under thermal-cyclic loading [12]. In addition, the residual stresses in the Cu-phase of W-Cu laminates are of the tension type, which makes the copper phase very sensitive to void formation and increases the risk of brittle failure (Fig. 21). A detachment of the tungsten-copper interface may significantly decrease the tensile ductility in terms of total elongation to fracture, A_t, as the beneficial residual stresses in the W-phase vanish. Finally, the contamination of tungsten with carbon has to be excluded.

It is envisioned to produce W-W laminated pipes made of severely cold-rolled, ultrafine-grained, potassium-doped tungsten foils. These pipes may be produced by a hot-isostatic-pressing process. There are great expectations that these pipes can retain the ductility and toughness of the ultrafine-grained tungsten foils, combined with an enhanced recrystallisation onset temperature (e.g. 1600°C (1873 K) for a 1 h heat treatment) and with an enhanced irradiation resistance.

Nuclear fusion is an ideal sustainable energy source. A major hurdle to its commercial development is the availability of sufficiently resilient materials. Tungsten laminated composites may contribute to clear this hurdle.

Acknowledgements

References

[1]   J. Knaster, A. Möslang, T. Muroga, Materials research for fusion, Nat. Phys. 12 (2016) 424–434.

[2]   H. Zohm, Assessment of DEMO challenges in technology and physics, Fusion Eng. Des. 88 (2013) 428–433.

[3]   S.J. Zinkle, A. Möslang, T. Muroga, H. Tanigawa, Multimodal options for materials research to advance the basis for fusion energy in the ITER era, Nucl. Fusion. 53 (2013) 104024.

[4]   E. Lassner, W.D. Schubert, Tungsten - Properties, Chemistry, Technology of the Element, Alloys, and Chemical Compounds, Springer, Berlin, 1999.

[5]   Q. Wei, L.J. Kecskes, Effect of low-temperature rolling on the tensile behavior of commercially pure tungsten, Mater. Sci. Eng. A. 491 (2008) 62–69.

[6]   J. Reiser, S. Wurster, J. Hoffmann, S. Bonk, C. Bonnekoh, D. Kiener, et al., Ductilisation of tungsten (W) through cold-rolling: R-curve behaviour, Int. J. Refract. Met. Hard Mater. 58 (2016) 22–33.

[7]   J. Reiser, J. Hoffmann, U. Jäntsch, M. Klimenkov, S. Bonk, C. Bonnekoh, et al., Ductilisation of tungsten (W): On the shift of the brittle-to-ductile transition (BDT) to lower temperatures through cold rolling, Int. J. Refract. Met. Hard Mater. 54 (2016) 351–369.

[8]   A.A.N. Németh, J. Reiser, D.E.J. Armstrong, M. Rieth, The nature of the brittle-to-ductile transition of ultra fine grained tungsten (W) foil, Int. J. Refract. Met. Hard Mater. 50 (2015) 9–15.

[9]   M. Seiss, T. Mrotzek, N. Dreer, W. Knabl, Thermophysical Properties of Molybdenum Copper Multilayer Composites for Thermal Management Applications, Mater. Sci. Forum. 825-826 (2015) 297–304.

[10]   W. Martienssen, H. Warlimont, Springer Handbook of Condensed Matter and Materials Data, Springer, Berlin Heidelberg, 2005.

[11]   R. Hill, The elastic behaviour of a crystalline aggregate, Proc. Roy. Soc. A 65 (1952) 349–354.

[12]   M. Seiss, T. Mrotzek, T. Hutsch, W. Knabl, Properties and reliability of molybdenum-copper-composites for thermal management applications, Proceedings of the 15th IEEE ITHERM Conference (2016) 971–975.

[13]   A. Misra, J.P. Hirth, R.G. Hoagland, Length-scale-dependent deformation mechanisms in incoherent metallic multilayered composites, Acta Mater. 53 (2005) 4817–4824.

[14]   W. D. Nix, Elastic and plastic properties of thin films on substrates: nanoindentation techniques, Mater. Sci. Eng. A. 234-236 (1997) 37–44.

[15]   A. Misra, J.P. Hirth, K. Kung, Single-dislocation-based strengthening mechanisms in nanoscale metallic multilayers, Philos. Mag. A 82 (2002) 2935–2951.

[16]   M. Vill, D.P. Adams, S.M. Yalisove, J.C. Bilello, Mechanical properties of tough multiscalar microlaminates, Acta Metall. Mater. 43 (1995) 427–437.

[17]   J. Reiser, M. Rieth, B. Dafferner, Tungsten foil laminate for structural divertor applications – Basics and outlook, J. Nucl. Mater. 423 (2012) 1–8.

[18]   W.W. Basuki, P. Norajitra, L. Spatafora, J. Aktaa, Fabrication of tungsten-vanadium hybrid material with sufficient toughness for high-temperature applications by diffusion bonding, Fusion Sci. Technol. 66 (2014) 315–321.

[19]   Y. Shao, D.Q. Jiang, F.M. Guo, Y.D. Ru, X.W. Hu, L.S. Cui, Fabrication and Property of W/Tininb Shape Memory Alloy Laminated Composite, Mater. Sci. Forum. 815 (2015) 211–216.

[20]   Y. Zhang, T. Ouyang, D. Liu, Y. Wang, J. Du, C. Zhang, et al., Effect of thickness ratio on toughening mechanisms of Ta/W multilayers, J. Alloys Compd. 666 (2016) 30–37.

[21]   J.T. Beals, V.C. Nardone, Tensile behaviour of a niobium/alumina composite laminate, 29 (1994) 2526–2530.

[22]   C.A. Hoffmann, J.W. Weeton, Tensile behavior of unnotched and notched tungsten-copper laminar composites, NASA TN D-8254, (1976).

[23]   D.L. McDanels, R.W. Jech, J.W. Weeton, Stress-Strain Behavior of Tungsten-Fiber-Reinforced Copper Composites, NASA TN D-1881, (1963).

[24]   J. Hohe, S. Fliegener, C. Findeisen, J. Reiser, V. Widak, M. Rieth, Numerical exploration into the potential of tungsten reinforced CuCrZr matrix composites, J. Nucl. Mater. 470 (2016) 13–29.

[25]   I.J. Beyerlein, N.A. Mara, J.S. Carpenter, T. Nizolek, W.M. Mook, T.A. Wynn, et al., Interface-driven microstructure development and ultra high strength of bulk nanostructured Cu-Nb multilayers fabricated by severe plastic deformation, J. Mater. Res. 28 (2013) 1799–1812.

[26]   S.B. Lee, J.E. Ledonne, S.C. V Lim, I.J. Beyerlein, a. D. Rollett, The heterophase interface character distribution of physical vapor-deposited and accumulative roll-bonded Cu-Nb multilayer composites, Acta Mater. 60 (2012) 1747–1761.

[27]   J. Reiser, P. Franke, T. Weingärtner, J. Hoffmann, A. Hoffmann, M. Rieth, Tungsten laminates made of ultrafine-grained (UFG) tungsten foil — Ageing of tungsten–titanium (W–Ti) laminates, Int. J. Refract. Met. Hard Mater. 51 (2015) 264–274.

[28]   Y. Shao, K. Yu, D. Jiang, C. Yu, Y. Ren, X. Jiang, F. Guo, L. Cui, High strength W/TiNi micro-laminated composite with transformation-mediated ductility, Mater. Des. 106 (2016) 415–419.

[29]   Annual Book of ASTM Standards—Standard Test Method for Plane-Strain Fracture Toughness of Metallic Materials (ASTM E 399–90), vol. 03.01, American Society for Testing and Materials; 1997.

[30]   www.plansee.com (2015)

[31]   J. Reiser, M. Rieth, B. Dafferner, A. Hoffmann, X. Yi, D.E.J. Armstrong, Tungsten foil laminate for structural divertor applications – Analyses and characterisation of tungsten foil, J. Nucl. Mater. 424 (2012) 197–203.

[32]   S. Bonk, J. Reiser, J. Hoffmann, A. Hoffmann, Cold rolled tungsten (W) plates and foils: Evolution of the microstructure, Int. J. Refract. Met. Hard Mater. 60 (2016) 92–98.

[33]   C. Bonnekoh, personal communication (2016).

[34]   J. Reiser, M. Rieth, A. Möslang, B. Dafferner, A. Hoffmann, J. Hoffmann, et al., Tungsten foil laminate for structural divertor applications - Tensile test properties of tungsten foil, J. Nucl. Mater. 434 (2013) 357–366.

[35]   M. Rieth, A. Hoffmann, Influence of microstructure and notch fabrication on impact bending properties of tungsten materials, Int. J. Refract. Met. Hard Mater. 28 (2010) 679–686.

[36]   L. Veleva, R. Schäublin, A. Ramar, et al., Focused Ion Beam Application on the Investigation of Tungsten-Based Materials for Fusion Application, Proceedings, Springer, Berlin, 2008.

[37]   H. Mughrabi, Plastic Deformation and Fracture of Materials, in Materials Science and Technology, A Comprehensive Treatment, edited by R.W. Cahn, P. Haasen, and E.J. Kramer, Volume 6, VCH, Weinheim, 1993.

[38]   A. Luft, C. Ritschel, Deformation and slip behaviour of cold-worked molybdenum single crystals at elevated temperatures, Phys. Stat. Sol. 72 (1982) 225–237.

[39]   C. Ritschel, A. Luft, D. Schulze, On the change of the dislocations structure during the postdeformation of cold worked molybdenum single crystals at elevated temperatures, Kristall und Technik 13 (1978) 791–797.

[40]   B.J. Brindley, P.J. Worthington, Yield-point phenomena in substitutional alloys, Met. Rev., 15 (1970) 101–114.

[41]   J.R. Rice, R. Thomson, Ductile versus brittle behaviour of crystals, Philos. Mag. 29 (1974) 73–97.

[42]   M. Khantha, D.P. Pope, V. Vitek, Dislocation screening and the brittle-to-ductile transition: A Kosterlitz-Thouless type instability, Phys. Rev. Lett., 73 (1994) 684–687.

[43]   P.B. Hirsch, S.G. Roberts, J. Samuels, The brittle-ductile transition in silicon. II. Interpretation, Proc. R. Soc. Lond., 421 (1989) 25–53.

[44]   S.G. Roberts. Modelling the brittle to ductile transition in single crystals. In: Kirchner HO, Kubin LP, Pontikis V, editors. Computer Simulations in Materials Science, series E: Applied Sciences, 308 (1996) 409–434.

[45]   S.G. Roberts, P.B. Hirsch, A.S. Booth, M. Ellis, F.S Serbena, Dislocations, cracks and brittleness in single crystals, Phys. Scripta T49 (1993) 420–426.

[46]   S.M. Ohr, An electron microscope study of crack tip deformation and its impact on the dislocation theory of fracture, Mater. Sci. Eng. 72 (1985) 1–35.

[47]   Y.H. Zhao, Y.Z. Guo, Q. Wei, T.D. Topping, A.M. Dangelewicz, Y.T. Zhu, T.G. Langdon, E.J. Lavernia, Influence of specimen dimensions and strain measurement methods on tensile stress-strain curves, Mater. Sci. Eng. A. 525 (2009) 68–77.

[48]   J. Reiser, et al., Ductilisation of tungsten (W): On the increase of strength AND room-temperature tensile ductility through cold-rolling, Int. J. Refract. Met. Hard Mater. 64 (2017) 261-278.

[49]   T. Gladman, F.B. Pickering, The effect of grain size on the mechanical properties of ferrous materials. In: Baker TN, editor. Yield, flow and fracture of polycrystals. London: Applied Science Publishers (1983) 148.

[50]   A. Alfonso, D. Juul Jensen, G.-N. Luo, W. Pantleon, Thermal stability of a highly-deformed warm-rolled tungsten plate in the temperature range 1100–1250°C, Fusion Eng. Des. 98–99 (2015) 1924–1928.

[51]   A. Alfonso, D. Juul Jensen, G.N. Luo, W. Pantleon, Recrystallization kinetics of warm-rolled tungsten in the temperature range 1150-1350°C, J. Nucl. Mater. 455 (2014) 591–594.

[52]   Y. Yuan, H. Greuner, B. Böswirth, K. Krieger, G.N. Luo, H.Y. Xu, et al., Recrystallization and grain growth behavior of rolled tungsten under VDE-like short pulse high heat flux loads, J. Nucl. Mater. 433 (2013) 523–530.

[53]   L.M. Garrison, Y. Katoh, L.L. Snead, T.S. Byun, J. Reiser, M. Rieth, Irradiation effects in tungsten-copper laminate composite, J. Nucl. Mater. 481 (2016) 134–146.

[54]   J. Reiser, M. Rieth, B. Dafferner, S. Baumgärtner, R. Ziegler, a. Hoffmann, Deep drawing of tungsten plates for structural divertor applications in future fusion devices, Fusion Eng. Des. 86 (2011) 2949–2953.

[55]   J. Reiser, M. Rieth, A. Möslang, H. Greuner, D.E.J. Armstrong, T. Denk, T. Gräning, W. Hering, A. Hoffmann, J. Hoffmann, H. Leiste, T. Mrotzek, R. Pippan, W. Schulmeyer, T. Weingärtner, A. Zabernig, Tungsten (W) laminate pipes for innovative high temperature energy conversion systems, Adv. Eng. Mater. (2014) 491–501.

[56]   H. Greuner, H. Bolt, B. Böswirth, T. Franke, P. McNeely, S. Obermayer, N. Rust, R. Süß, Design, performance and construction of a 2MW ion beam test facility for plasma facing components, Fusion Eng. Des. 75-79 (2005) 345–350.

[57]   H. Greuner, B. Boeswirth, J. Boscary, P. McNeely, High heat flux facility GLADIS:. Operational characteristics and results of W7-X pre-series target tests, J. Nucl. Mater. 367-370 B (2007) 1444–1448.

[58]   L.S. Tong, A phenomenological study of critical heat flux, ASME paper, 75-HT-68 (1975).

[59]   T.R. Barrett, S.C. McIntosh, M. Fursdon, D. Hancock, W. Timmis, M. Coleman, M. Rieth, J. Reiser, Enhancing the DEMO divertor target by interlayer engineering, Fusion Eng. Des. 98-99 (2015) 1216–1220.

[60]   J. Linke, High Heat Flux Performance of Plasma Facing Materials and Components Under Service Conditions in Future Fusion Reactors, Fusion Sci. Technol. 57 (2010) 293-302.

[61]   M.S. Tillack, a. R. Raffray, X.R. Wang, S. Malang, S. Abdel-Khalik, M. Yoda, D. Youchison, Recent US activities on advanced He-cooled W-alloy divertor concepts for fusion power plants, Fusion Eng. Des. 86 (2011) 71–98.

[62]   X. Wang, S. Malang, A.R. Raffray, the ARIES Team, Design optimization of high-performance helium-cooled divertor plate concept, Fusion Sci. Technol. 56 (2009) 1023–1027.

[63]   P. Norajitra, S.I. Abdel-Khalik, L.M. Giancarli, T. Ihli, G. Janeschitz, S. Malang, I. V. Mazul, P. Sardain, Divertor conceptual designs for a fusion power plant, Fusion Eng. Des. 83 (2008) 893–902.

[64]   J. Reiser, M. Rieth, Optimization and limitations of known DEMO divertor concepts, Fusion Eng. Des. 87 (2012) 718–721.

[65]   A. Delano, D. Mathur, Managing heat flux in advanced packages, Semiconductor International, 30 (2007) SP-9-SP-13.

[66]   J. Bratberg, Z. Metallkd. 96 (2005) 335-344.

[67]   A. Borgenstam, A. Engström, L. Höglund, J. Ågren, J. Phase Equilib. 21 (2000) 269.

[68]   Landolt-Börnstein NS III/26, H. Mehrer, Ed., "Diffusion in Solid Metals and Alloys", Springer, 1990.

[69]   S.M. Klotsman, G.N. Tatarinova, A.N. Timofeev, Defect Diff. Forum 330 (2012) 1-10.

[70]   J. Pelleg, V. Segel, Physica B 393 (2007) 259-265.

[71]   L.S. Darken, Trans. AIME 175 (1948) 184-194.

[72]   S. V. Nagender Naidu, P. Rama Rao, Phase Diagrams of Binary Tungsten Alloys, Indian Institute of Metals, Calcutta,1991.

[73]   M.A. Meyers, A. Mishra, D.J. Benson, Mechanical properties of nanocrystalline materials, Prog. Mater. Sci. 51 (2006) 427–556.

[74]   C. Bonnekoh et al., The controlling mechanisms of the BDT in ultrafine-grained tungsten foils, Tungsten workshop, Nov. 2015, Reutte, Plansee SE.

[75]   E. Pink, L. Bartha, Metallurgy of Doped/Non-Sag Tungsten, Springer, 1989.

[76]   S. Nogami, W. Guan, M. Fukuda, A. Hasegawa, Effect of microstructural anisotropy on the mechanical properties of K-doped tungsten rods for plasma facing components, Fusion Eng. Des. 109-111 (2016) 1549–1553.

[77]   M. Fukuda, S. Nogami, K. Yabuuchi, A. Hasegawa, T. Muroga, Anisotropy in the mechanical properties of potassium and rhenium doped tungsten alloy plates for fusion reactor applications, Fusion Science and Technology 68 (2015) 690–693.

[78]   X. Shu, H. Qiu, B. Huang, Z. Gu, J. Yang, J. Liao, Y. Yang, N. Liu, J. Tang, Preparation and characterization of potassium doped tungsten, J. Nucl. Mater. 440 (2013) 414–419.

[79]   I. Wesemann, W. Spielmann, P. Heel, A. Hoffmann, Fracture strength and microstructure of ODS tungsten alloys, Int. J. Refract. Met. Hard Mater. 28 (2010) 687–691.

[80]   Z. Chen, W. Han, J. Yu, K. Zhu, Effect of 800 keV argon ions pre-damage on the helium blister formation of tungsten exposed to 60 keV helium ions, J. Nucl. Mater. 472 (2016) 110–117.

[81]   D.E.J. Armstrong, T.B. Britton, Effect of dislocation density on improved radiation hardening resistance of nano-structured tungsten-rhenium, Mater. Sci. Eng. A. 611 (2014) 388–393.

[82]   T. Koyanagi, N.A.P. Kiran Kumar, T. Hwang, L.M. Garrison, X. Hu, L.L. Snead, Y. Katoh, Microstructural evolution of pure tungsten neutron irradiated with a mixed energy spectrum, J. Nucl. Mater. 490 (2017) 66–74.